Space Science and Engineering Center
University of Wisconsin-Madison

Science Support for the Earth Radiation Budget Experiment (ERBE)

# A REPORT from the

# Cooperative Institute for Meteorological Satellite Studies

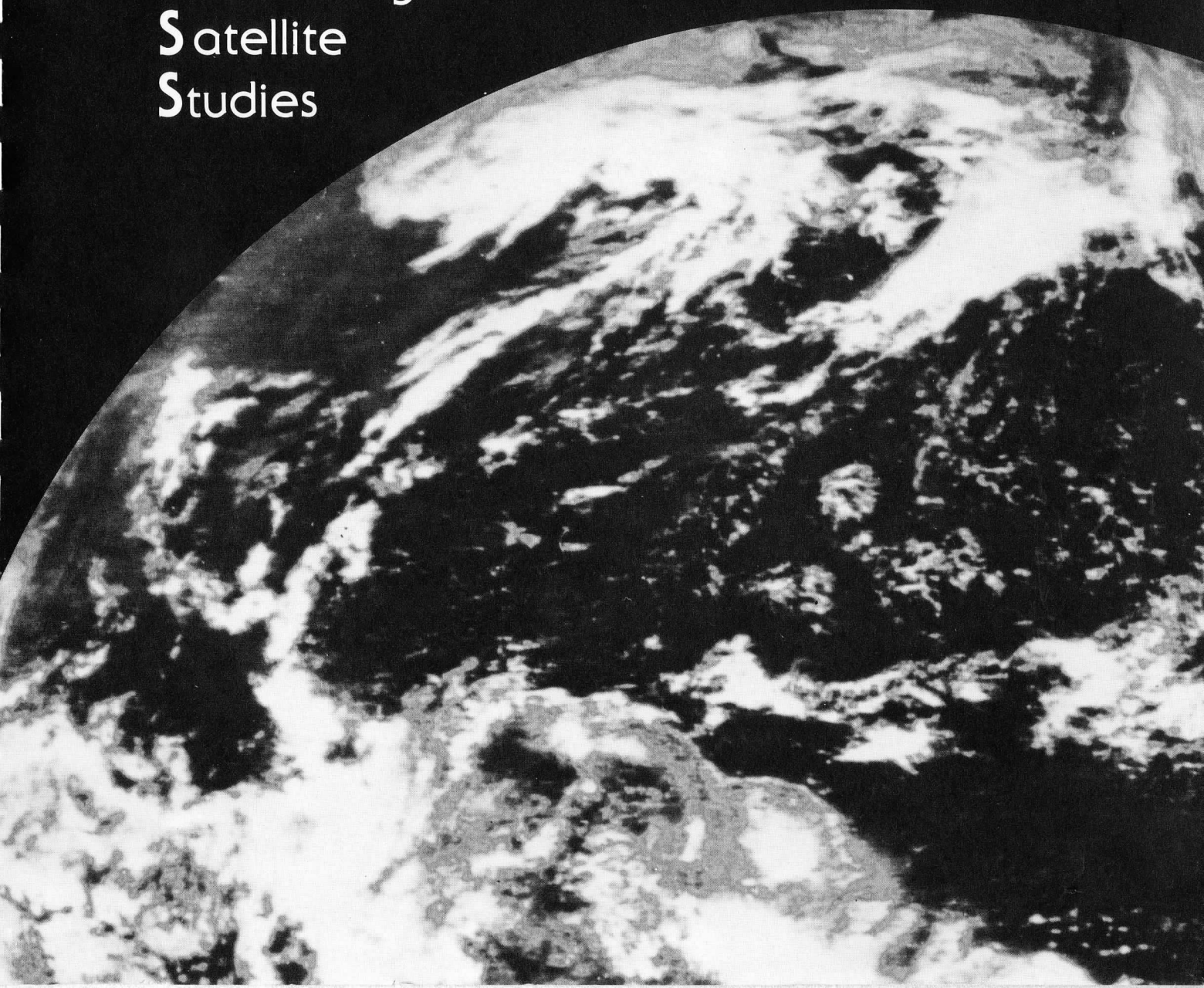

# Science Support for the Earth Radiation Budget Experiment (ERBE)

A Final Report

for

NASA Contract NAS1-16507

Prepared By:

William L. Smith
Leroy D. Herman
Thomas H. Achtor

May 7, 1987

FINAL REPORT ON CONTRACT NAS1-16507:
NASA, LANGLEY RESEARCH CENTER

EARTH RADIATION BUDGET EXPERIMENT (ERBE) SCIENTIFIC INVESTIGATIONS

This report summarizes research efforts at the Cooperative Institute for Meteorological Satellite Studies (CIMSS) for NASA contract NAS1-16507. The report also contains an index and copies of presentations, papers and a graduate student Master's Degree thesis completed under this contract.

Under the contract listing for potential science support, participation in the following areas was requested;

1) Unresolved development trade-offs
2) Sensor calibration
3) Sensor performance
4) Operation planning for data acquisition
5) Format(s) for data collection
6) Development, use and testing of algorithms for extraction of parameters of interest
7) Forms of output data products for use in instrument validation and in investigations
8) Verification of the data output products by comparison with measurements obtained by other means.

CIMSS has participated in many of these areas, as summarized below.

Initially, the ERBE data was examined for consistency. ERBE imagery was compared with coincident GOES visible and infrared imagery, checking for cloud and clear sky correspondence. An estimate of ERBE navigation accuarcy was accomplished by locating geographical landmarks. The navigation accuracy was considered acceptable given the instrument resolution.

Efforts to detect scanner noise discovered suspect patterns in the ERBS imagery. Very sharp discontinuities were found in the grey scale data, which implied straight line cloud edges. These discontinuities were usually located along (parallel to) scan lines. This banding or striping occurred frequently and was determined to be a significant source of error. Several methods were tried to remove the striping by statistical methods, but it was found that these techniques altered the radiance information in other areas.

Work was also done comparing scanner and non-scanner data over the same geographical region. It was found that averaging the non-scanner data reduced single sample noise and produced the highest quality result.

Long wave scanner radiative flux at the top of the atmosphere from ERBS was compared to VAS multi-spectral data. For mostly clear sky conditions the best correlation between the ERBS and VAS data was found to be when the ERBS scanner data was compared to a combination of two VAS water vapor channels and the window channel radiance data.

Finally, a study comparing the scanner and non-scanner data for consistency and accuracy was developed as part of a graduate student research project. Data was checked for quality control and a coordinate transformation algorithm produced data sets from the same reference frame for comparison. Examination of the data showed the ERBE observations from the two instruments to have similar values for the same observation and be of reasonably high quality.

More details on these and other issues are contained in the papers included in this final report.

ERBE SCIENTIFIC RESEARCH DOCUMENTS; CONTRACT NAS1-16507

| DATE | TITLE |
|---|---|
| 1985-86 | Wu, Xiangqian. A Method for Comparing ERBE Data. (M.S. Thesis, University of Wisconsin-Madison.) |
| 3/18/85 | Herman, Leroy D. A Comparison of ERBS and GOES Infrared and Visible Data. (Presented at the 15th ERBE Science Team Meeting.) |
| 3/18/85 | Herman, Leroy D. A Quick Comparison of ERBS Landmarks on November 9, 1984 (15th ERBE Science Team Meeting.) |
| 7/22/85 - 11/1/85 | Herman, Leroy D. Stripping (Banding) Problem. (Letter and memo to Bruce Barkstrom.) |
| 12/3/85 | Herman, Leroy D. A Search for ERBS Scanner Noise. (Presented at the 17th ERBE Science Team Meeting.) |
| 12/3/85 | Herman, Leroy D. and X. Wu. A Preliminary Comparison Between Scanner and Non-Scanner Data. (17th ERBE Science Team Meeting.) |
| 12/3/85 | Nagle, Fred. A Quick View of ERBS Scan and Non Scan Data. (17th ERBE Science Team Meeting.) |
| 5/13/86 | Herman, Leroy D. Removal of Striping from ERBE Data. (Presented at the 18th ERBE Science Team Meeting.) |
| 5/13/86 | Herman Leroy D., and W.L. Smith. Intercomparison of Preliminary ERBS Flux Estimates and Geostationary Satellite Multi-Spectral VAS Radiance Measurements. (Presented at 6th Conference on Atmospheric Radiation, Williamsburg, VA.) |

ERBE SCIENTIFIC RESEARCH DOCUMENTS: CONTRACT NAS1-16507

# A Method for Comparing ERBE Data

By

XIANGQIAN WU

A thesis submitted in partial fullfilment
of the requirement for the degree of

MASTER OF SCIENCE
( Meteorology )

at the

UNIVERSITY OF WISCONSIN -- MADISON

1986

TABLE OF CONTENTS

## ABSTRACT

The Earth Radiation Budget Experiment estimates the solar constant, the back-scattered and the re-emitted radiation at the top of the atmosphere (TOA) with wide, medium and narrow angle radiometers. A cross validation algorithm is developed in this paper, which simulates the irradiance at the satellite altitude by integrating the radiance at the TOA. The irradiance is observed by the nonscanner, the radiance is estimated by the scanners, and the integration is performed separately for the shortwave and longwave radiations. Main components of the algorithm are quality control of the data, coordinate transformation, angular dependence models of radiation, and the division of the WFOV into angular bins. For the 18 comparisons performed, the weighted average of the relative difference is 1.9%; the weighted average of the linear correlation coefficient is 0.9820; the hypothesis that those two data sets are from the same population is verified at the level of significance of 0.1. The results provide reasonable confidence in the ERBE observations. More work is needed to refine the absolute accuracy of both the scanner and nonscanner measurements.

ACKNOWLEDGEMENT

I would like to thank my advisor, Prof. William L. Smith, for his scientific guidance throughout this work. His carefulness in reading and commenting on this thesis was especially helpful. I enjoyed very much the years I have worked with him.

The Tang Kak Ji Trust in Hong Kong granted me a scholarship to initiate my graduate study. Mr. L. Herman provided me with the ERBS data. Messrs. F. Nagle and H. Woolf were always willing to help me in computer facilities. Dr. L. Sromovsky, Mr. T. Achtor, Profs. V. E. Suomi and J. A. Young generously offered many valuable comments on this thesis. Their assistance is greatly appreciated.

Finally, everyone in my family deserves my deepest regards. They have always helped me to maintain a clear perspective on my work and life. My dear mother did not live to see this completion, but she still is, and will be, another source of encouragement in my life.

This research was supported by the ERBE Project through Grant NAS1-16507.

LIST OF FIGURES AND TABLES

## LIST OF ACRONYMS

...for those appearing more than once

| | |
|---|---|
| ERBE | Earth Radiation Budget Experiment |
| ERBS | Earth Radiation Budget Satellite |
| DMS | Data Management System |
| FOV | Field Of View |
| MFOV | Medium Field Of View |
| NASA | National Aeronautical and Space Administration |
| NFOV | Narrow Field Of View |
| PAT | Processed Archival Data |
| TOA | Top Of the Atmosphere |
| WFOV | Wide Field Of View |

# 1. INTRODUCTION

The Earth Radiation Budget Experiment (ERBE) estimates the solar constant, the reflected and back-scattered shortwave radiation, and the earth-atmosphere emitted longwave radiation at the top of the atmosphere (TOA). Radiometers implemented in ERBE differ from one another both in their fields of view (FOV) and in their response to the electromagnetic spectrum. Nonscanning wide field of view (WFOV, radius of about 2,500 km) are used to measure the irradiance at the height of satellite. Scanning narrow field of view (NFOV, about 30 by 45 km at nadir) radiometers are used to measure the radiance, from which irradiance field with much higher resolution can be derived. Nonscanning medium field of view (MFOV, radius of about 500 km) flat plate radiometers measure the irradiance with a better resolution than that of WFOV, but also suffer more from the bidirectional characteristics of the reflected radiation (Barkstrom and Smith, 1986). Moreover, scanner can scan either across or along the satellite ground track, although this study uses the across-track scan mode only.

Prior to using these data for quantitative estimates of the earth radiation budget, it is important to validate the measurements archived by the various ERBE sensors and the estimates derived from those measurements by the ERBE Data Management System (DMS). A research was conducted in which the spectral irradiance observed by the nonscanners (WFOV and MFOV) at the satellite altitude is simulated by an angular integration of the spectral radiance at the TOA estimated by the narrow angle scanning sensors. A cross validation of the ERBE data follows by comparing the angularly integrated scanning data with measurements made by the nonscanner sensors throughout an entire orbit as well as for some local times. The data used for this paper are from the Earth Radiation Budget Satellite (ERBS) acquired on Nov. 9, 1984. The algorithm can also be applied to data obtained for other ERBE satellites as they become available.

## 2 ALGORITHM

### 2.1 Physical Basis

Consider a system in space consisting of a radiating object (the earth-atmosphere subsystem) and a point (nonscanner on satellite) some distance away from the object. Assume:

a) intermediate space between the TOA and the spacecraft is a perfect vacuum;

b) direct sunshine is completely baffled away from all sensors when observing; and

c) nonscanners receive only negligible amount of radiation from other celestial bodies.
(For example, when viewed from the nonscanner, the solid angle subtended by the moon is only about 1/10 of that by an NFOV. Assumed to be a perfect whitebody, the moon contributes an irradiance to the nonscanner less than $0.02 W/m^2$.)

In the absence of other sources and sinks of radiation, one could calculate the irradiance at the point from the object provided that the followings are known:

1. geometry of the system;
2. radiance distribution at the surface of that object; and
3. angular dependence of radiance.

Those requirements are met in this research as follows:

1. The TOA is assumed to be 30 km above an "idealized earth", which is an ellipsoid with the half major axis = 6378.2 km at its equator plane and half minor axis = 6356.8 km between its poles (Yang et al, 1980).

2. The radiance field at the TOA is derived from scanner data for the shortwave and longwave radiance components, respectively.

   An implicit assumption associated with this irradiance estimate is that the radiation field under study is "fixed" for measurement

during an "integration time", which is 272 seconds (about 4.5 minutes) for integration over the WFOV and 80 seconds (less than 1.5 minutes) for integration over the MFOV. "Fixed radiation field" means that the radiance, solar zenith angle and scene type of the NFOV will not change (or have not changed, depending on the relative position of the NFOV to the nonscanners) for a time interval not less than the integration time. However, the rotation of the whole radiation field with the earth-fixed coordinates is permitted, because the transformed coordinates will rotate accordingly (cf. Section 2.3).

3. The angular dependence of radiance is estimated by the bidirectional model (Taylor and Stowe, 1984).

## 2.2 Quality Control

Thorough scrutiny of the ERBE data for errors has been done by the DMS (Hall, 1983), and "bad data" are tagged by default values and/or corresponding flag

words. The Quality Control procedure of the algorithm does not assess the quality of data from ERBE S-8 PAT. It only discriminates the flagged bad data from the good ones, the latter will be input into the algorithm as "true data".

There are two steps in the quality control procedure. The first step is to eliminate data in the Processed Archival Tape (PAT) which are unusable for applying the angular integration algorithm. Those unusable data include:

a) Missing record;

b) Too many bad data within a record; and

c) Bad nonscanner data

Missing record (case (a)) will occur when all data from all sensors in the entire 16-second period are invalid. When this happens, continuity of scanner data coverage will be interrupted, which will definitely influence the accuracy of the simulation.

Missing records occur relatively rarely. For example, only 13 out of 5,400 records in the PAT for Nov. 9, 1984 are missed. In contrast, there are often

some data in a record which are invalid, especially at the beginning and the ends of scan lines. If in a record there are too many invalid data, or the bad data are concentrated at the center of scan lines, the quality of that record will be severely compromised (case (b)).

Evaluation of record quality in this context is as follows. Recognizing that data at the center of scan lines are much more valuable than those at the fringe, the algorithm assigns a different weight to each Narrow Field Of View (NFOV) observation according to its position on the scan lines. A normal distribution for the weights is assumed (Fig.1):

$$W(i) = \exp(-((i-a)/b)^{**}2) \qquad (2\text{-}1)$$

where W(i) is the weight of the i'th NFOV in a line, a = 31.5 is the index for the central NFOV, and b = (i=a)/sqrt(2) = 21.57 is empirically defined. (One could assign different values to a and b to get any weight distribution desired.) When an invalid datum with index i is subjected to the algorithm, its weight will be computed by Eq.(2-1) and stored as a "bad credit". The total credits of a scan line is (cf.

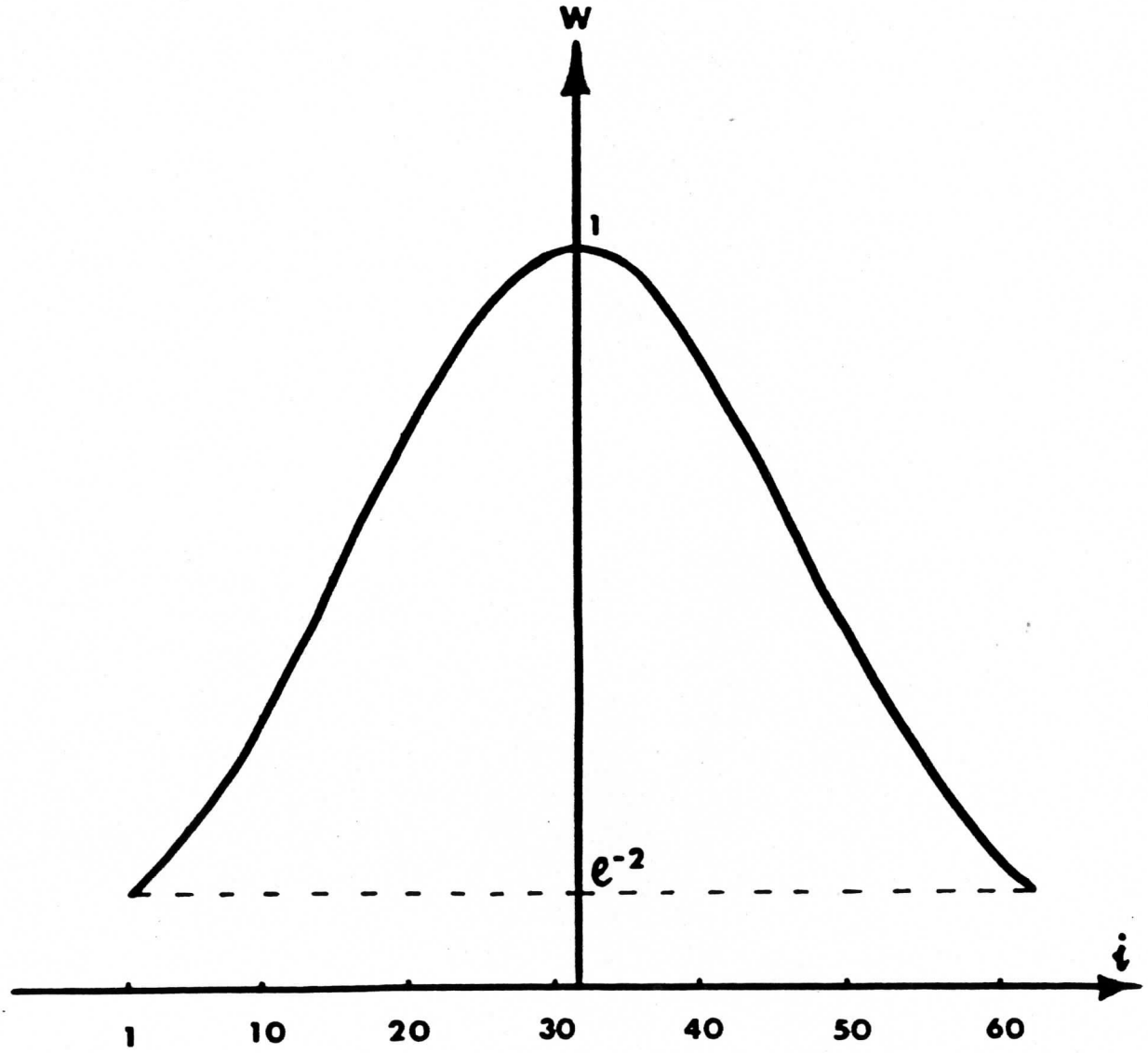


Figure 1 Weighting function of i'th (i=1,...,62) NFOV on a scan line. It is used for record quality evaluation.

Spiegel, 1975):

$$\int_{1}^{62} W(i) * di = P\left[|i-a| < \left(\frac{62-1}{2}\right)\left(\frac{1}{b\sqrt{2}}\right)\right] \int_{-\infty}^{\infty} W(i)\,di$$

$$= .9958 * b\sqrt{\pi} \qquad (2\text{-}2)$$

Thus, the ratio between the accumulated bad credit and the total credit computed by Eq.(2-2) will define the quality of that record. An empirical criterion of 5% is adopted, which means that records passing this quality control examination will, with priority defined by Eq.(2-1), have at least 95% valid data.

The case (c) for the vital deficiency of a data record is due to invalid nonscanner data as a result of direct sunshine at satellite sunrise and sunset. However, the scanner data of that record might still be usable as long as it has "95% valid data", defined above, and it is not one of the "pivot records" (cf. Section 3.1).

This first step of quality control is carried out before any subroutines. It interprets all flag words for record quality evaluation. As its product, warnings are marked out for those records where integration is not recommended (cases (a) & (b)) or

where comparison is prohibited (case(c)).

The second step of quality control is performed as the PAT tape is read in. Before any datum enters the algorithm, its validity is examined and bad data are rejected. In its place a value linearly interpolated from adjacent "true data" may be filled in (if the bad datum happens to be on the "selected scan lines", cf. Section 2.4). The algorithm searches for the nearest valid data m indices along the line and n indices across the line (currently, m = 4 and n = 2). The linear interpolation follows:

$$L = \frac{\sum_j Lj * Wj}{\sum_j Wj} \qquad (2\text{-}3)$$

provided that j (j=1,...,4) valid data are found and that the weight Wj varies inversely with the distance between the valid and the invalid data. The limits m and n prevent the search from being carried out too far away from the invalid data so that the algorithm will not suffer from unrealistic interpolation. Also, since those interpolated data are less than 5% of the total data, errors due to this procedure are small.

## 2.3 Coordinate Transformation:

A description of the notation is in order before reader can understand the following equations. Lower-case Greek letters are used to refer to the NFOV, and the corresponding upper-case Greek letters are used to refer to the WFOV or MFOV nonscanning radiometers. For example, $\theta_R$ is the zenith angle of the radiometer R with respect to the NFOV P, i.e., $\angle$ZPR in Fig.2, while $\theta_P$ is the zenith angle of P with respect to R, or $\angle$QPR in Fig.2. Exceptions are made for colatitude/longitude, where $(\varphi, \lambda)$ are with respect to the geographic coordinate, and $(\Phi, \Lambda)$ are with respect to the transformed coordinate. Moreover, $(\theta', \psi')$ and $(\Theta', \Psi')$ are integration arguments.

An NFOV P (Fig.2) centered at $(\Theta_P, \Psi_P)$ and subtending a solid angle $(\Delta\Theta_P * \Delta\Psi_P)$ will contribute to radiometer R the irradiance Ep given by:

$$Ep = \int_{\Psi_P}^{\Psi_P+\Delta\Psi_P} \int_{\Theta_P}^{\Theta_P+\Delta\Theta_P} L(\sigma, \zeta, \Theta', \Psi') \cos\Theta' \sin\Theta' d\Theta' d\Psi'$$

$$= 0.5 * \bar{L}\left[\sin^2(\Theta_P+\Delta\Theta_P) - \sin^2\Theta_P\right]\Delta\Psi_P \qquad (2\text{-}4)$$

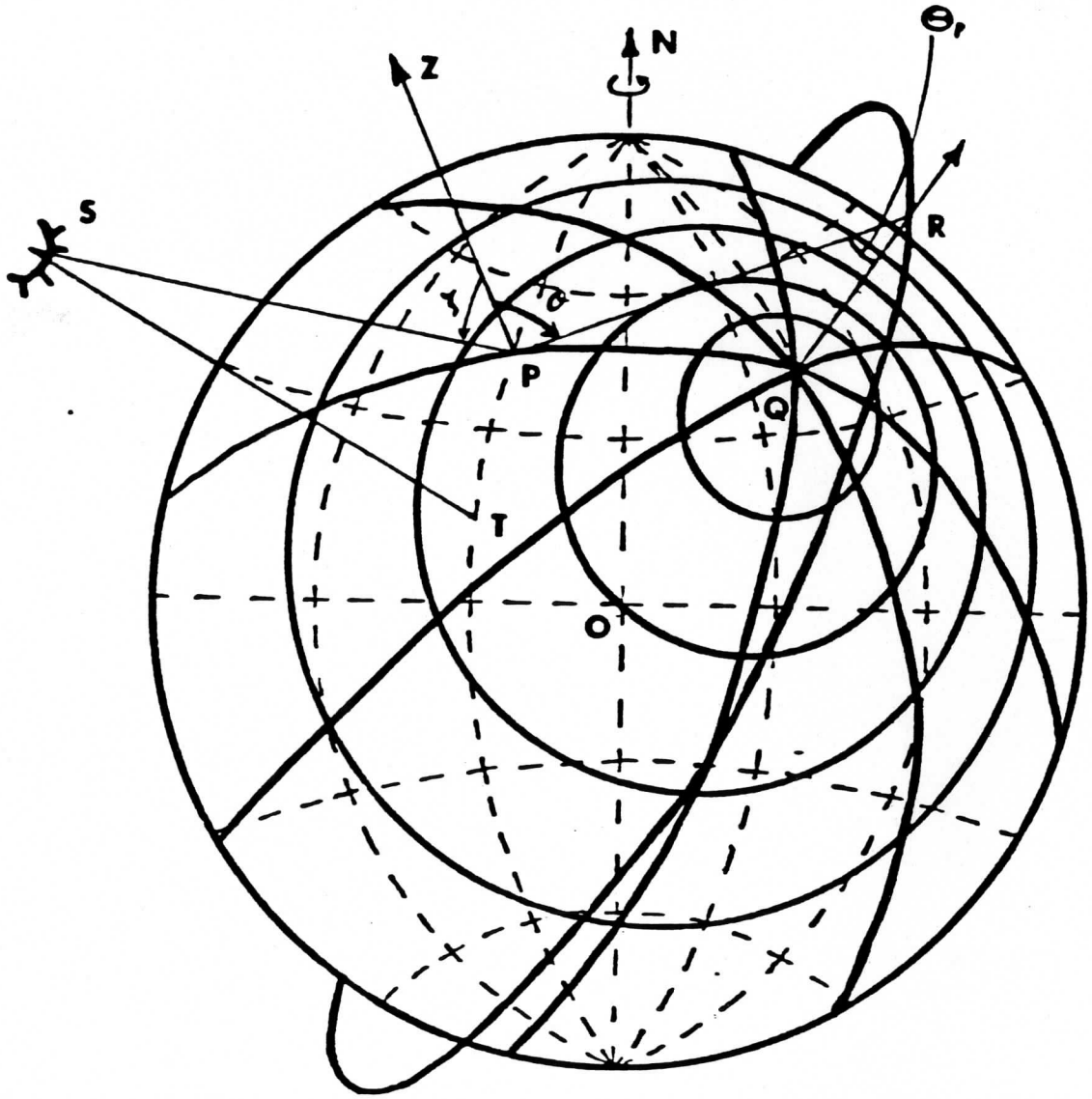


Figure 2. Coordinate transformation.

Solid line : Transformed colatitude/longitude;
Broken line : Geographic colatitude/longitude;
Thin solid line : Geometry.

N : the north pole;
O : the center of the earth;
P : position of the NFOV under study;
Q : satellite nadir point;
R : radiometer, i.e., position of satellite;
S : the sun;
T : the sub-sun point;
Z : the local zenith of the NFOV.

where :

$\Theta_p$ : zenith angle;

$\Psi_p$ : azimuth angle;

L : radiance from P to R;

$\bar{L}$ : average of L over P.

$\bar{L}$ can be obtained by applying proper anisotropic index to the appropriate ERBE data, so the question becomes to find $\Theta_p$ and $\Psi_p$.

To solve this problem, the algorithm transforms the original geographic coordinates ($\varphi p, \lambda p$) to another one with the transformed north pole at the nonscanner's nadir point, as illustrated in Fig.2. Then the NFOV's in a nonscanner's FOV are sorted into several angular bins defined in the transformed coordinates (cf. Section 2.4). The average radiance and the solid angles of those angular bins are computed (cf. Section 2.5), and finally one could simulate the irradiance measured by a nonscanner sensor. Suppose the transformed colatitude/longitude of P is ($\Phi p, \Lambda p$). With simple sine theory:

$$p = \arcsin\left(\frac{Rtoa * \sin\Phi p}{\sqrt{Rsat^2 + Rtoa^2 - 2Rsat*Rtoa*\cos\Phi p}}\right)$$

$$\Psi_p = \Lambda_p \qquad (2\text{-}5)$$

The coordinate transformation is based on spherical trigonometry, by which $\Phi_p$ and $\Lambda_p$ are calculated. Consider the triangle $\Delta NPQ$ on a sphere (Fig.2) with known geographic colatitude/longitude $N(0,0)$, $P(\varphi_p,\lambda_p)$, and $Q(\varphi_q,\lambda_q)$. It follows that:

$$\widehat{PQ} = \arccos(\cos\varphi_p * \cos\varphi_q + \sin\varphi_p * \sin\varphi_q * \cos(\lambda_p - \lambda_q))$$

$$\angle PQN = \arcsin(\sin\varphi_p * \sin(\lambda_p - \lambda_q) / \sin\widehat{PQ})$$

with:

$$\varphi_p = \widehat{NP}$$

$$\varphi_q = \widehat{NQ}$$

$$\lambda_p - \lambda_q = \angle PNQ \qquad (2\text{-}6)$$

where $\varphi$ and $\lambda$ are colatitude and longitude.

The transformed colatitude $\Phi_p$ is the $\widehat{PQ}$ and the transformed longitude $\Lambda_p$ is $\angle PQN$ + const. This constant is subject to the choice of a prime meridian, which can be assigned arbitrarily, such as along the satellite ground track. However, it would be much easier to first find $\Lambda_p$ with respect to the prime meridian $\widehat{NQ}$. This requires only one more definition of

the 90-270 meridian which, along with the prime meridian NQ, separates the FOV into four quadrants. It turns out that this 90-270 meridian is along the points $(\varphi^*, \lambda p)$, measured in original (geographic) coordinate, with:

$$\varphi^* = \varphi q + (90 - \varphi q) * (1 - \cos(\lambda p - \lambda q)) \qquad (2\text{-}7)$$

In summary, the transformed coordinates, with respect to the prime meridian $\widehat{NQ}$, are computed as:

$$\Phi p = \widehat{PQ}$$

$$\Lambda p = \begin{cases} \angle PQN, & \varphi p < \varphi^* \text{ and } \lambda p > \lambda q \\ 360 + \angle PQN, & \varphi p > \varphi^* \text{ and } \lambda p < \lambda q \\ 180 - \angle PQN, & \text{else} \end{cases} \qquad (2\text{-}8)$$

In the algorithm, a subroutine is devoted to this coordinate transformation. In addition to the application described above, it is also used to calculate the relative azimuth $\alpha$ between the sun and spacecraft. To do this, the spherical coordinate is transformed to point P, instead of to point Q as shown in Fig.2. After the transformed longitudes of the sun and that of the spacecraft are calculated separately,

the relative azimuth $\alpha$ is given by:

$$\alpha = \mathrm{ABS}(\mathrm{ABS}(\tilde{\Lambda}_s - \tilde{\Lambda}_r) - 180) \qquad (2\text{-}9)$$

where $\tilde{\Lambda}$ denotes that those are longitudes in the transformed coordinate centered at P, rather than at Q. The scene type $\sigma$ , the solar zenith angle $\zeta$ , and the colatitude $\varphi$ are given in the PAT and are supposed to be constant during the integration time (cf. Section 2.1). With this relative azimuth angle $\alpha$ and the viewing zenith angle $\theta_R$:

$$\theta_R = \arcsin\left(\frac{\mathrm{Rsat} * \sin\frac{1}{2}p}{\mathrm{Rtoa}}\right) \qquad (2\text{-}10)$$

one is able to find the appropriate anisotropic indices $\mathrm{Asw}(\sigma, \zeta, \theta, \alpha)$ and $\mathrm{ALw}(\sigma, \theta, \varphi)$, and further the radiance to the nonscanners.

## 2.4 Division of WFOV into Angular Bins

Knowing the transformed coordinates of each NFOV, we next want to sort those NFOVs into pre-defined angular bins. This is postponed to the next section,

for the division of FOV into angular bins deserves some discussion.

In terms of the transformed coordinates with spacecraft ground track as prime meridian, one notes that at low colatitudes ($\Phi$ small, or around the nadir point), the scanner data points have approximately an angularly homogeneous distribution, or, the distance between projections of the scanner data points on a sphere, centered at nonscanner with Rsat as the radius, is approximately the same. At higher colatitudes ($\Phi$ large, or towards the fringe of a WFOV), there are too many data around $\Lambda = 0$ and $\Lambda = 180$ due to geometry, and very few data around $\Lambda = 90$ and $\Lambda = 270$ because the inversion procedure in the DMS does not interpret the datum from a NFOV if it views the ERBS at a zenith angle larger than 70°.

It would be unnecessary to divide the WFOV into angular bins if the scanner data points had an angularly homogeneous distribution. In that case each scanner datum would represent an equal solid angle $\omega_i$, therefore:

$$E_I = \int_{\Omega} L \star d\omega \doteq \sum_{j=1}^{n} Lj \star \omega_j = \frac{\hat{\pi}}{n} \sum_{j=1}^{n} Lj \qquad (2\text{-}11)$$

where $E_1$ is the irradiance at the nonscanning radiometers obtained through integration, $\Omega$ is the solid angle subtended by the full disk of the earth, Lj is the average radiance of the j'th pixel subtending a solid angle $\omega_j$ (the scanner measurement), and n is the total number of data points. The actual distribution of scanner data points is, of course, not exactly angularly homogeneous anywhere, but this equation does tell us that the mesh need not be very fine around the nadir point.

Things are more complex and contradictory at the fringes of a WFOV. If the mesh is too fine, some of bins will contain no valid scanner data due to the distribution of the scanner data, resulting in "blank spots" where valid data are sparse. If on the other hand the mesh is too coarse, two other problems appear: 1) the area where scanner data are dense will be unrealistically weighted too heavily; 2) a bin which is "at night" (therefore indeed "blank" in the shortwave spectrum) may be interpreted as "at day" if a single non-zero data exists in a corner of that large bin.

There are two approaches to deal with the situation at the fringe of the WFOV. One is to follow Eq.(2-11), i.e., to select scanner data so that they are more homogeneous. The other is to carefully design the angular bins to minimize the errors due to scanner data inhomogeneity. Since the real data can never be ideally homogeneous (synthesized data based on some kind of objective analysis can meet this requirement, see Section 3.3), while the second approach is too complicated, the algorithm uses a combination of the two to gain the optimal result, which should be a compromise between:

* An accurate representation of the radiance distribution in the WFOV,
* More complete bins, and
* Simplicity.

The optimal combination was determined empirically. Many designs were tested on a representative scanner data set which has all valid data only in the central 58 scanning pixels on any scan line. The following factors have been considered in different combinations:

1) The number and spacing (usually uneven) of

rings and sectors -- the coarsest mesh contains 12 bins (3 rings by 4 sectors), and the finest mesh contains 288 bins (12 rings by 24 sectors).

2) The orientation of the prime meridian -- every 5 degree between local true north and the satellite ground track.

3) The selection of scan lines -- the idea is to skip a certain number of scan lines at the fringe; therefore, the remaining selected scan lines are more homogeneous. Invalid scanner data on the selected lines are replaced by linearly interpolated values (cf. Section 2.2). Note that instead of discarding those extra scan lines, one could also average them to find "better" values for the selected lines. However, that would more than double the computing time (only 67 out of 180 scan lines are selected), and the experimental runs did not show noticeable difference between the two choices.

The final version of the angular bin

distribution and scan line selection is not as complicated as many of those tested , and are depicted in Fig.3 and Fig.4.

## 2.5 Integration and Statistics

Having completed the previous works, the integration and the comparison is fairly straight forward.

### 2.5.1 Integration

1. Sort $P(\Theta p, \Psi p)$ into proper angular bins bounded by $(\Theta bi, \Psi bi)$. The transformed coordinates of scanner datum $P(\Theta p, \Psi p)$ are known from Section 2.3. The boundary of angular bins $(\Theta bi, \Psi bi)$ are known from Section 2.4.

2. Compute the average radiance $\bar{L}i$ of bin i:

$$\bar{L}i = \sum_{j=i}^{n} \frac{Lj}{n} \qquad (2\text{-}12)$$

where Lj,j=1,...,n is the average radiance

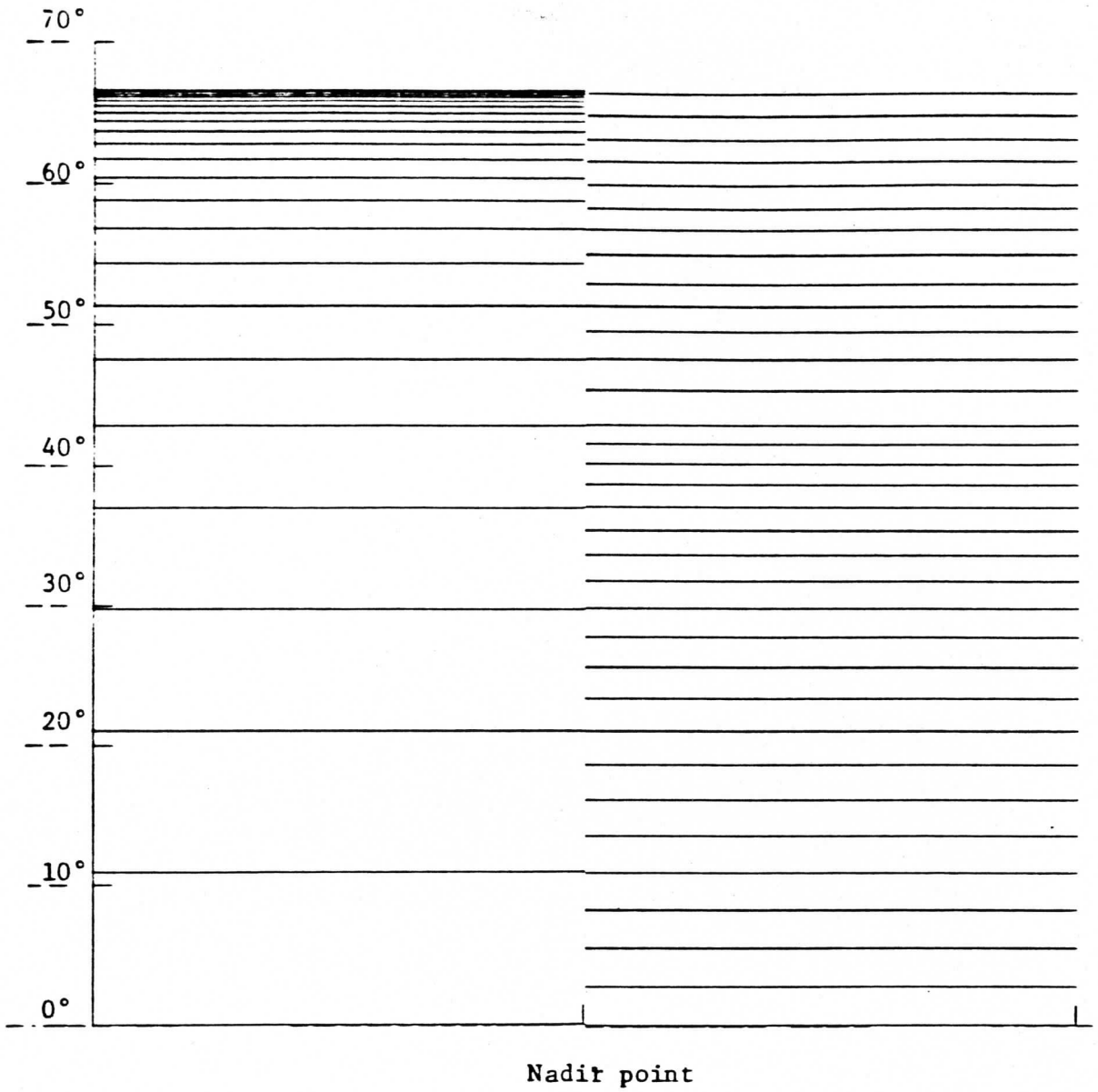


Figure 3 Scan lines in a WFOV before (left) and after (right) the selection of scan line. All the selected lines are shown on the right while only every 4 scan lines before the selection are shown.

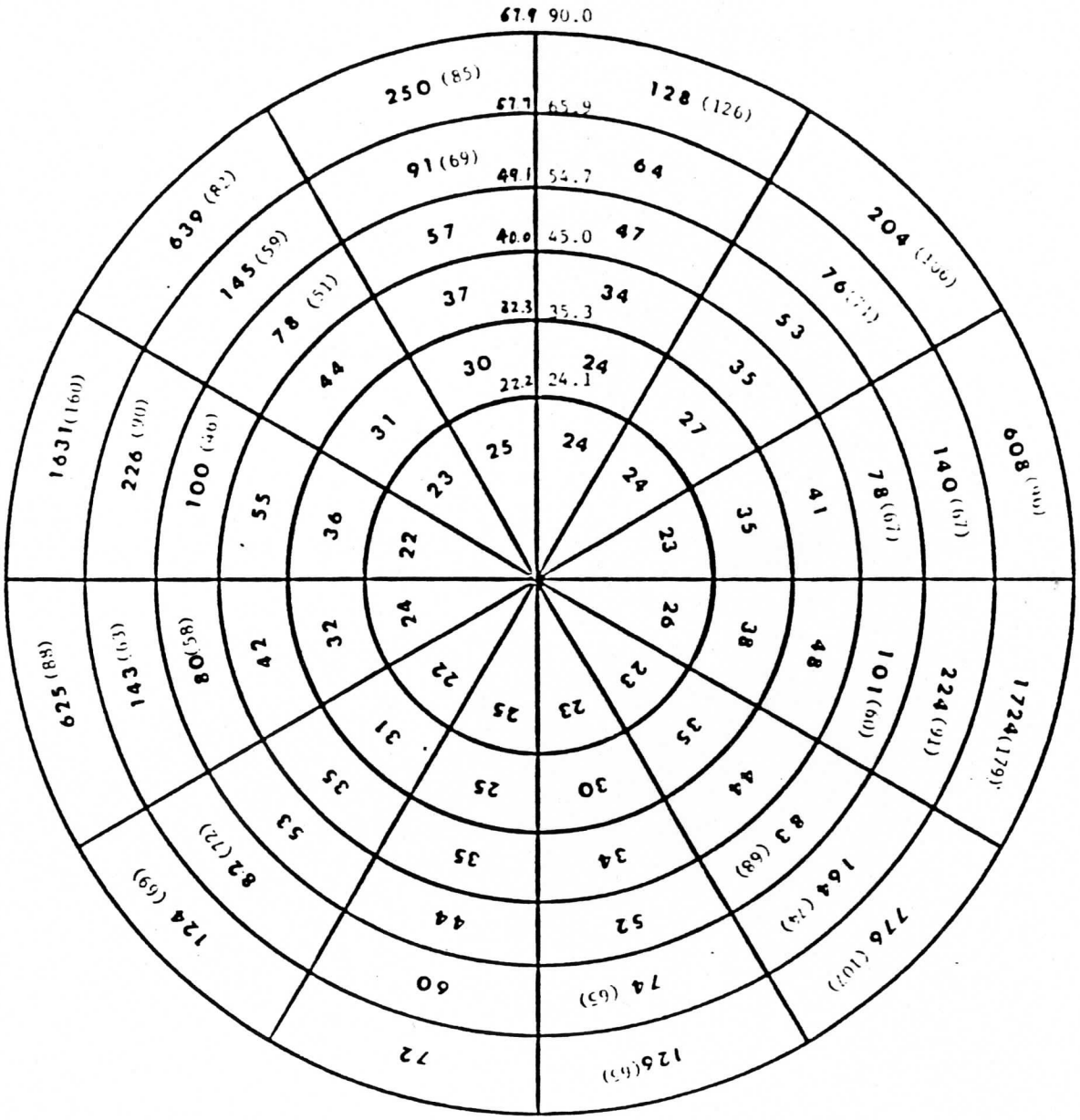


Figure 4 Division of WFOV into angular bins. Number of pixels in each angular bin before and after (will be in parenthesis if different) the scan line selection are shown. Prime meridian is the local true north. Azimuth angles between sectors are equal; zenith angles of rings are hand-written for $\Theta_p$ and printed for $\theta_R$.

from the j'th NFOV to the direction of the nonscanner, and all n NFOV's are in bin i.

3. Compute the solid angle subtended by bin i:

$$\omega_j = (\sin^2\Phi_{bi} - \sin^2\Phi_{bi-1})(\Psi_{bi} - \Psi_{bi-1})/2 \qquad (2\text{-}13)$$

4. Finally, sum up the contributions from all angular bins:

$$E_1 = \sum_{j=1}^{N} \bar{L}i * \omega_i \qquad (2\text{-}14)$$

where $E_1$ is defined in (2-11) and N is the total number of angular bins.

### 2.5.2 Statistics

Simulated observations Xi,i=1,...,n and actual observations (nonscanner measurements) Yi,i=1,...,n are compared by a statistics subroutine, which computes:

a) Maxima:

$$Ymax = \max_i (Yi,\ i=i,...,n)$$

$$Xmax = \max_i (Xi,\ i=i,...,n) \qquad (2\text{-}15)$$

b) Minima:

$$Ymin = \min_i (Yi,\ i=1,\ldots,n)$$

$$Xmin = \min_i (Xi,\ i=1,\ldots,n) \qquad (2\text{-}16)$$

c) Means:

$$\bar{Y} = \frac{1}{n}\sum_{i=1}^{n} Yi$$

$$\bar{X} = \frac{1}{n}\sum_{i=1}^{n} Xi \qquad (2\text{-}17)$$

d) Standard deviation of samples:

$$Sy = \left(\frac{1}{n}\sum_{i=1}^{n} Yi^2 - \bar{Y}^2\right)$$

$$Sx = \left(\frac{1}{n}\sum_{i=1}^{n} Xi^2 - \bar{X}^2\right) \qquad (2\text{-}18)$$

e) Difference in means:

$$D = \bar{X} - \bar{Y} \qquad (2\text{-}19)$$

f) Linear correlation coefficient:

$$r = \frac{\frac{1}{n}\sum_{i=1}^{n} Y_i X_i - \bar{Y}\bar{X}}{S_Y S_X} \qquad (2\text{-}20)$$

g) t-test with the null hypothesis that $\mu_y = \mu_x$, as well as $\sigma_y = \sigma_x$, where $\mu$ is the

mathematical expectation and $\sigma$ is the standard deviation of population, respectively. (Note that this implies that the two samples are from the same population):

$$t = |\bar{X} - \bar{Y}| \left( \frac{n-1}{S_X^2 + S_Y^2} \right) \qquad (2\text{-}21)$$

(a) - (f) show some general characteristics of the resemblance of the observation and the integration, while (g) is a statistical decision. A significant level of 0.10 is used, which means that if the results passed this test, one would not say that "the observation is different from simulation", given 10% possibility of being wrong.

# 3 RESULTS AND CONCLUSIONS

## 3.1 Sampling

Nonscanners make an observation every 0.8 second and those data are stored in PAT. However, those data proved to be too noisy for comparisons. Nonscanner data used for comparison are instead taken from the average of every 5 raw observations. Further, if a record is used for comparison, which will be called PIVOT RECORD henceafter, simulation is made only for the first of the four observations. All those pivot records are summarized in Table 1, Figs.5 & 6.

A simulation of a WFOV observation may involve more than 100 scan lines on each side of the satellite ground track. As discussed in Section 2.4, those scan lines at the very edge of a WFOV are redundant for a better interpretation of the radiance field observed. The algorithm thus reads only 90 lines on each side of the nadir (22 sequential records before and after the pivot record).

Table 1 Summary of Pivot Records

| Comparison Objective | Number of Pivot Records Used | Indices of Pivot Records in PAT (spacing 5) |
|---|---|---|
| Whole Orbit, Shortwave | 21 | 945-1045 |
| Whole Orbit, Longwave | 72 | 944-1304 except 1114 & 1239 (bad nonscanner data) |
| Morning | 15 | 222- 232, 1302-1312, 2032-2042, 2392,2402, 2762-2772 |
| Noon | 15 | 625- 635, 985- 995, 1345-1355, 1710-1720, 2070-2080 |
| Evening | 15 | 1400-1410, 1760-1770, 2125-2135, 2490-2500, 2850-2860 |
| Night | 15 | 77- 87, 439- 449, 802- 812, 1165-1175, 1528-1538 |

Figure 5 Locations of pivot records in the comparison.

9 NOV 84

— : Entire Orbit; ● : Morning; ▲ : Noon; ○ : Evening; ■ : Night.
(✱ indicates where the shortwave comparison ends.)

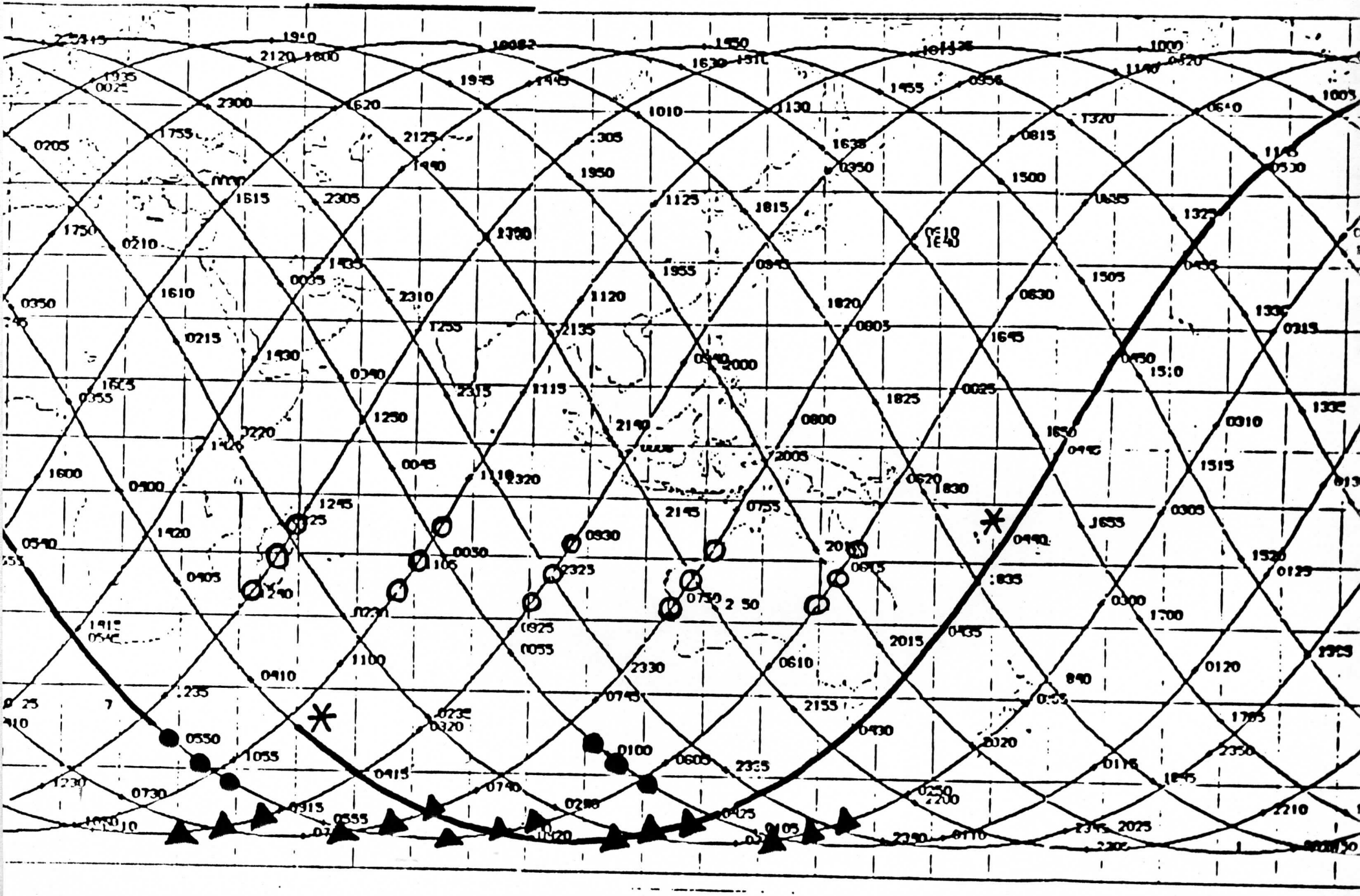

Fig. 6

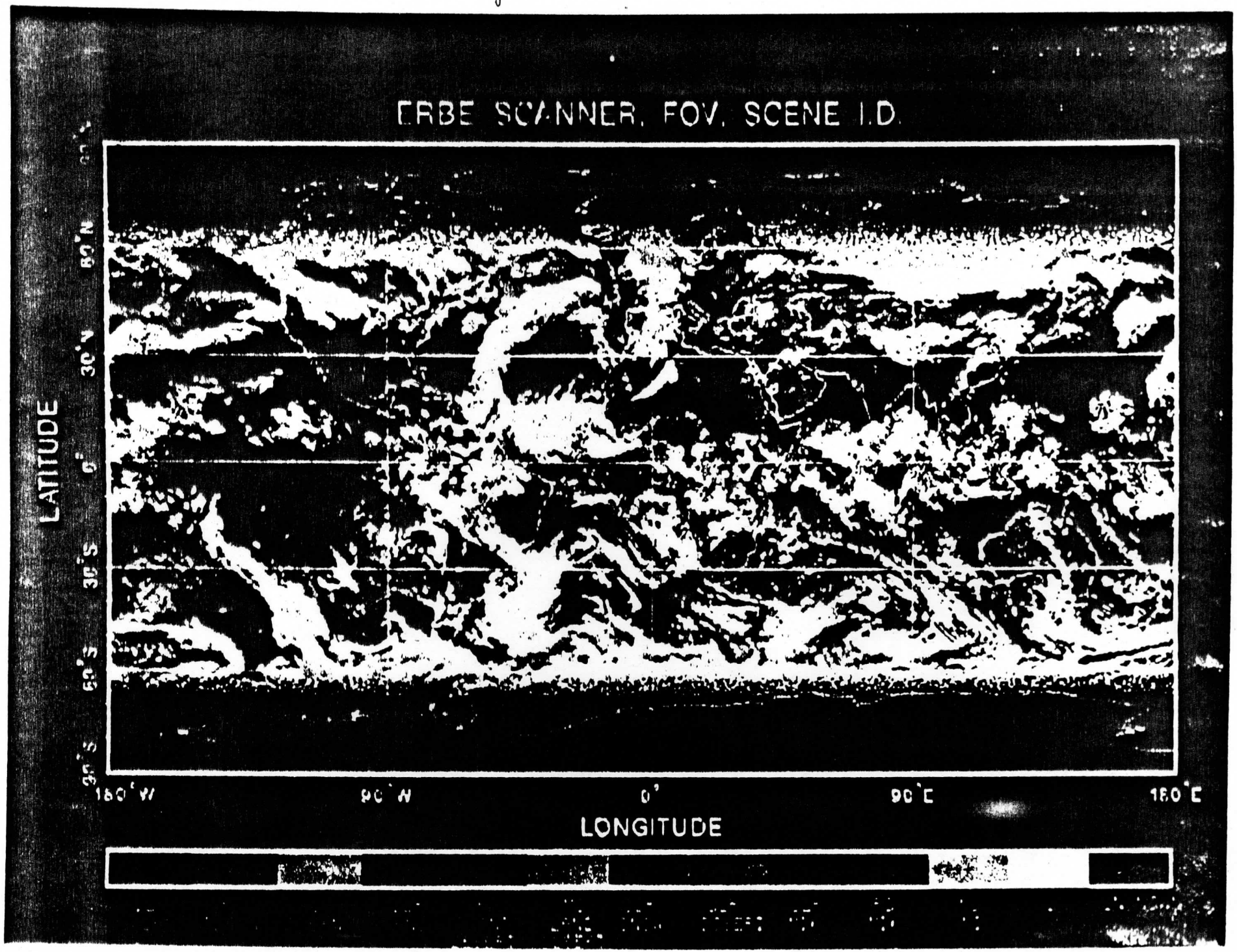
ERBE SCANNER, FOV, SCENE I.D.
LATITUDE
90°N
30°N
0°
30°S
60°S
90°S
180°W
90°W
0°
90°E
180°E
LONGITUDE

In all comparisons, pivot records have a spacing of 5 records so that their MFOVs do not overlap. There are roughly 360 records archived in PAT as ERBS completes one circle around the earth, providing 72 pivot records for an "Entire Orbit" comparison in longwave channel. For shortwave comparison, however, only about 150 records are taken at "daytime" in one orbit, bounded by records of poor quality for the channel due to the direct sunshine at satellite sunrise and sunset. Also, the first and the last 22 records can not be used as pivot records, leaving only 21 pivot records available for shortwave comparison.

Comparisons are also made at four local times: morning, noon, evening, and night. In all those 4 comparisons at local times, three pivot records are fetched from each orbit, so that each comparison of 15 pivot records reflects characteristics of 5 different orbits. For comparisons in the morning and evening, the first (last) pivot record record is taken as early (late) as possible as long as a sufficient number of scan lines of good quality remains on the "night side". For comparisons at noon and night, the time the central pivot record is taken to be the closest to 12 a.m. or 12 p.m. local time.

## 3.2 Result

Results are summarized in Table 2 and plotted in Fig.7. Columns in Table 2 follow the order of the statistics routine described in Section 2.5, but the results of Student t-test are omitted because only one comparison failed to pass that test (this case is footnoted). In Fig.7 the abscissa, representing the observation, and the ordinate, representing the simulation, are deliberately set to be equal; by doing so the "slope error" and the "offset error" will show up by the relation between the best fit line and the diagonal. The "slope error" indicates whether the simulations are always greater (less) than the observations. The "offset error" indicates by how much the two differ. The way the data points scatter about the best fit line indicates the degree of correlation between the simulation and the observation.

Columns "maxima" and "minima" in Table 2 show the wide range of the data, from 36.1 $W/m^2$ to 389.8 $W/m^2$ in terms of irradiance of the radiation field being compared. Those data also span a great variety of geographic and meteorological features (Figs.5 & 6).

Table 2 Results of the comparisons

| Comparison Objective | | Maxima W/m² | | Minima W/m² | | Mean W/m² | | Standard Deviation W/m² | | SML-OBS | | Correlation Coefficient |
|---|---|---|---|---|---|---|---|---|---|---|---|---|
| | (#) | OBS (*) | SML | OBS | SML | OBS | SML | OBS | SML | W/m² | % | |
| Entire Orbit | SW,WFOV | 365.0 | 378.6 | 107.3 | 113.0 | 258.3 | 265.3 | 73.6 | 75.6 | 7.1 | 2.7 | .9966 |
| | SW,MFOV | 194.2 | 199.0 | 36.1 | 45.7 | 126.2 | 129.7 | 45.6 | 44.1 | 3.7 | 2.7 | .9908 |
| | LW,WFOV | 227.7 | 229.6 | 154.2 | 158.8 | 194.8 | 195.7 | 21.5 | 21.2 | 0.9 | 0.0 | .9585 |
| | LW,MFOV | 122.6 | 122.6 | 73.0 | 75.8 | 100.1 | 100.3 | 13.7 | 13.4 | 0.2 | 0.0 | .9902 |
| Morning | SW,WFOV | 282.7 | 297.8 | 195.0 | 204.6 | 240.7 | 253.2 | 29.5 | 30.8 | 12.5 | 5.1 | .9926 |
| | SW,MFOV | 154.7 | 168.2 | 87.9 | 96.2 | 122.2 | 133.5 | 23.1 | 23.5 | 11.3 | 8.8 | .9886 |
| | LW,WFOV | 213.5 | 210.9 | 173.0 | 165.6 | 194.2 | 189.3 | 11.7 | 12.6 | -4.9 | 3.6 | .9933 |
| | LW,MFOV | 105.5 | 105.5 | 74.2 | 76.5 | 93.3 | 95.4 | 8.6 | 7.9 | 2.2 | 2.3 | .9917 |
| Noon | SW,WFOV | 389.8 | 399.5 | 275.3 | 269.0 | 340.7 | 343.4 | 30.6 | 34.7 | 2.7 | 0.8 | .9975 |
| | SW,MFOV | 219.6 | 218.5 | 138.0 | 134.0 | 179.4 | 176.7 | 23.9 | 24.8 | -2.7 | 1.5 | .9973 |
| | LW,WFOV (@) | 201.3 | 197.1 | 181.3 | 171.8 | 190.9 | 182.1 | 6.3 | 7.4 | -8.8 | 4.7 | .9625 |
| | LW,MFOV | 100.6 | 102.6 | 82.7 | 82.5 | 90.0 | 91.1 | 4.5 | 5.1 | 1.1 | 1.2 | .9706 |
| Evening | SW,WFOV | 220.4 | 231.7 | 112.7 | 105.8 | 141.5 | 146.1 | 29.2 | 32.0 | 4.7 | 3.3 | .9876 |
| | SW,MFOV | 119.9 | 126.3 | 39.9 | 46.2 | 65.8 | 72.0 | 23.6 | 23.2 | 6.3 | 4.6 | .9915 |
| | LW,WFOV | 261.7 | 265.0 | 203.7 | 201.9 | 227.6 | 229.4 | 16.3 | 17.4 | 1.8 | 0.8 | .9965 |
| | LW,MFOV | 140.2 | 143.0 | 94.4 | 97.1 | 115.4 | 118.4 | 13.2 | 12.3 | 3.0 | 2.6 | .9916 |
| Night | LW,WFOV | 168.0 | 176.0 | 147.2 | 134.2 | 160.5 | 163.0 | 5.3 | 10.4 | 2.6 | 1.6 | .9495 |
| | LW,MFOV | 90.9 | 92.7 | 72.5 | 64.7 | 83.9 | 82.8 | 4.9 | 6.5 | -1.1 | 1.3 | .9776 |

(*) OBS : Observation by nonscanner
SML : Simulation from scanner

(#) SW : Shortwave
LW : Longwave

(@) Failed to pass the Student t-test at a level of significance of 0.1

Figure 16 Plots of the results.
Horizontal : OBS; Vertical : SML; Unit : $W/m^2$.

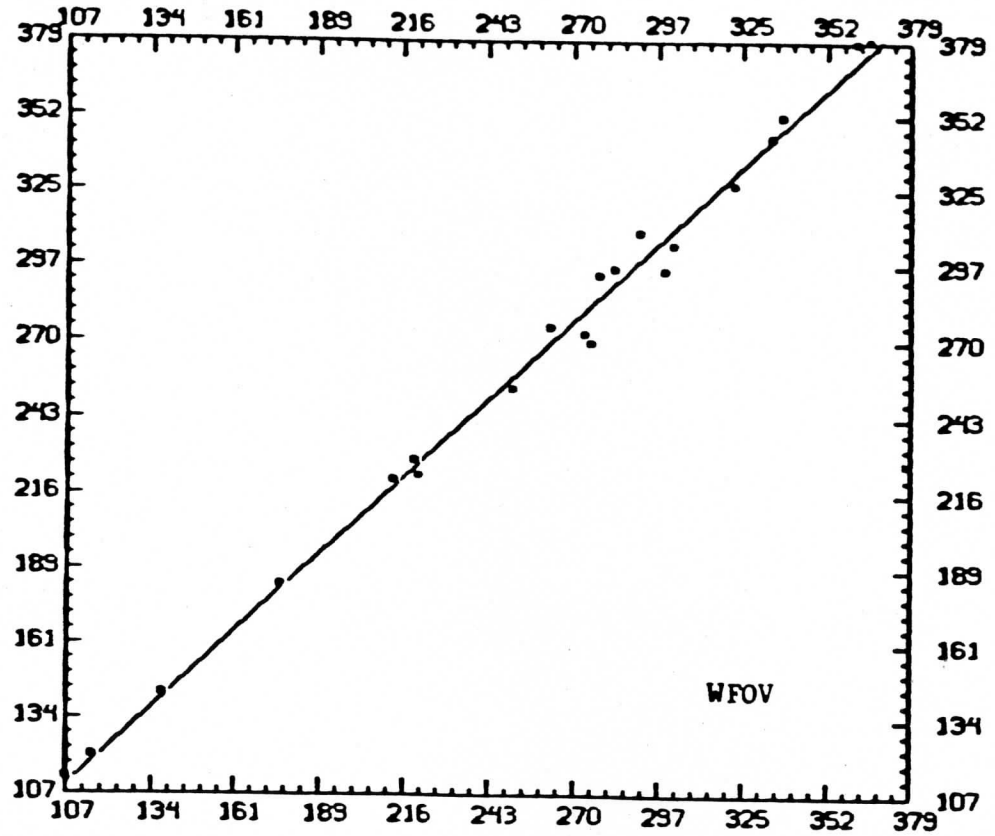


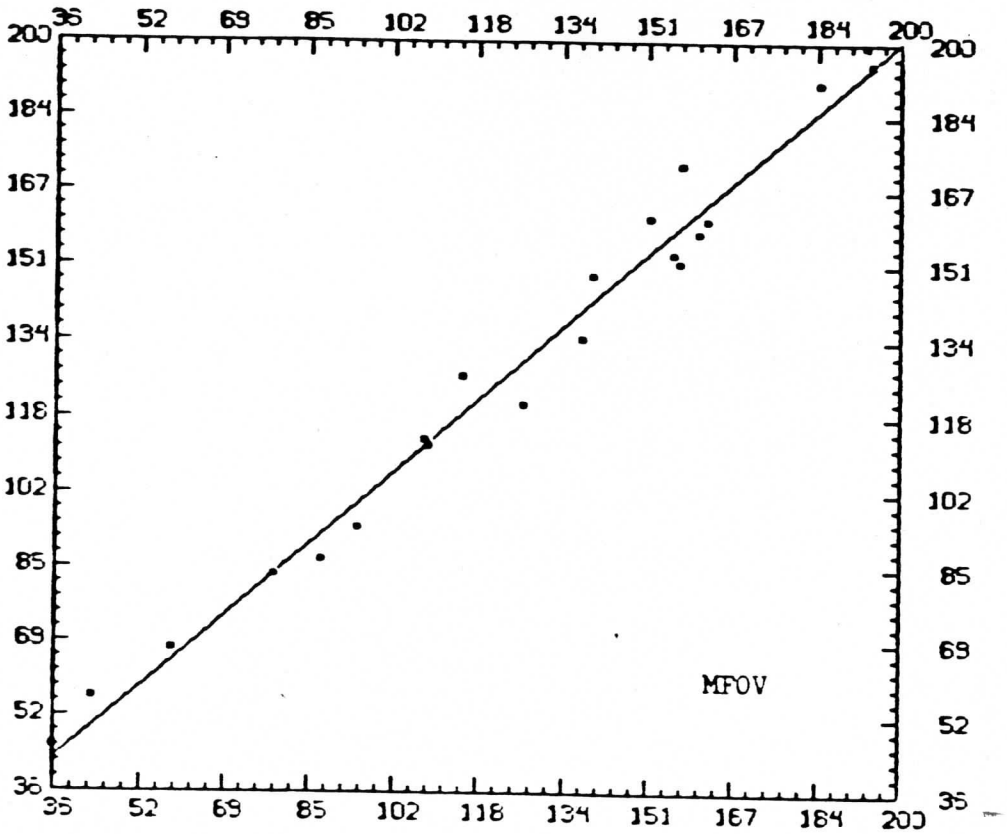




(a) Entire Orbit . SW

Horizontal : OBS; Vertical : SML; Unit : $W/m^2$

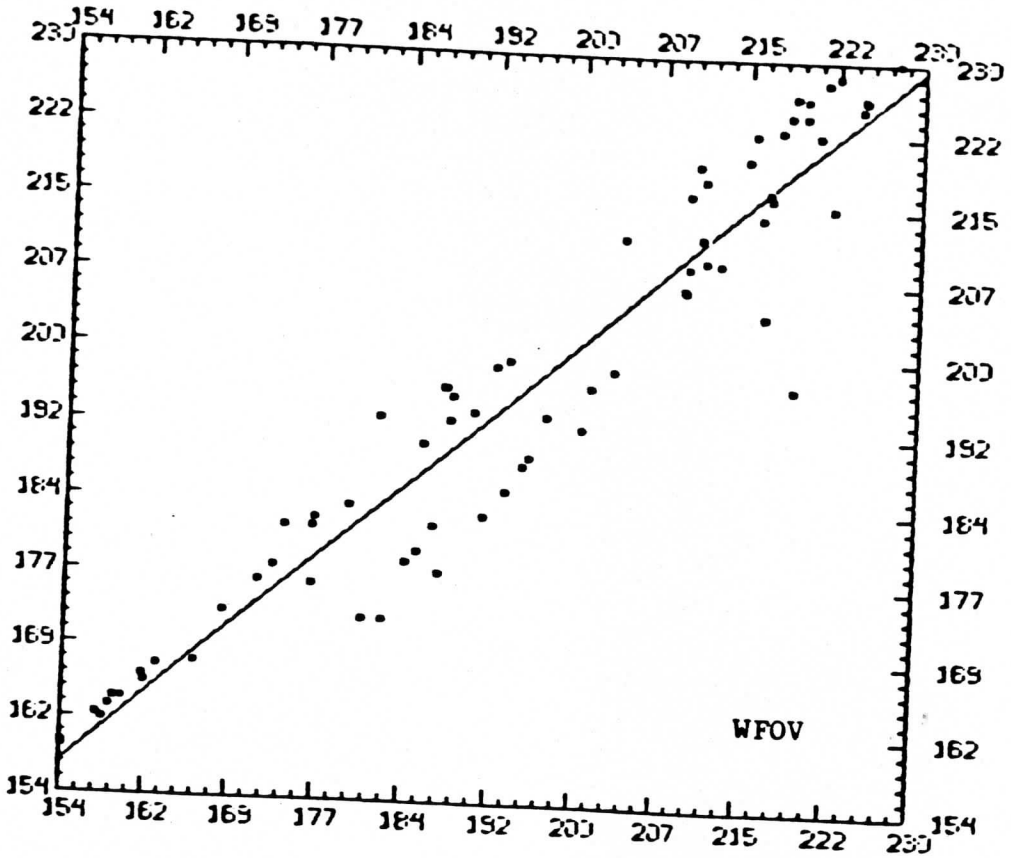


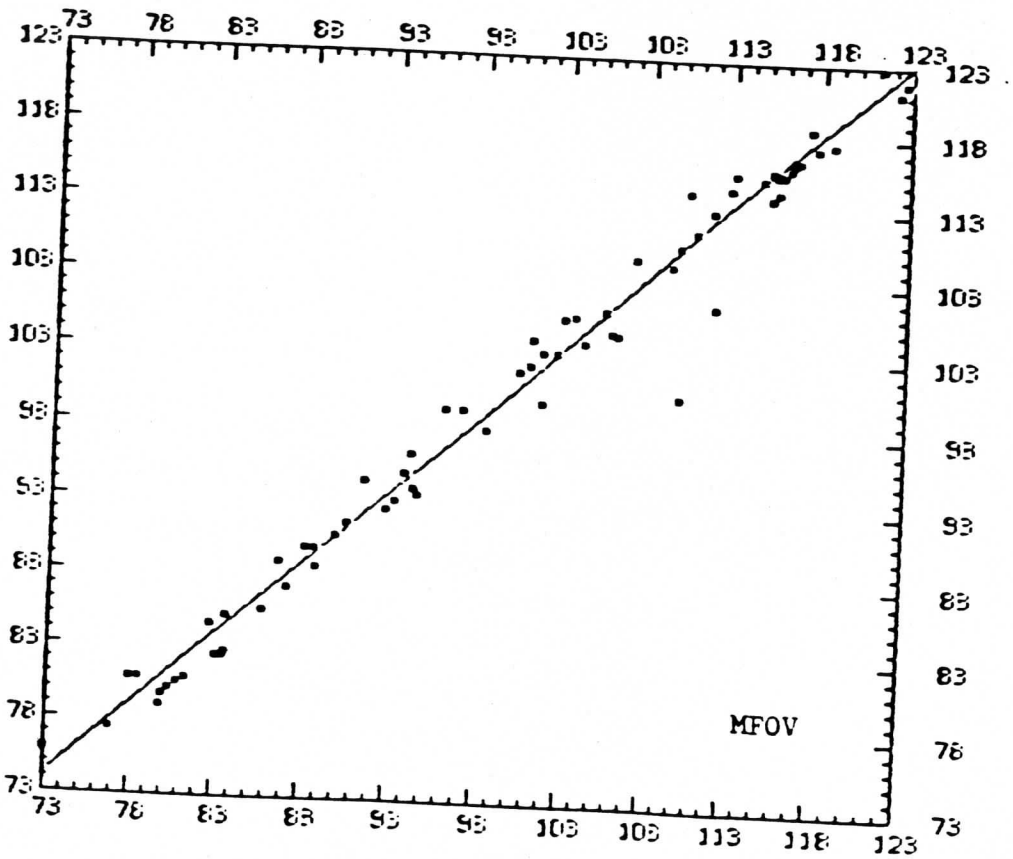


(b) Entire Orbit, LW.

Horizontal : OBS;  Vertical : SML  Unit : $W/m^2$

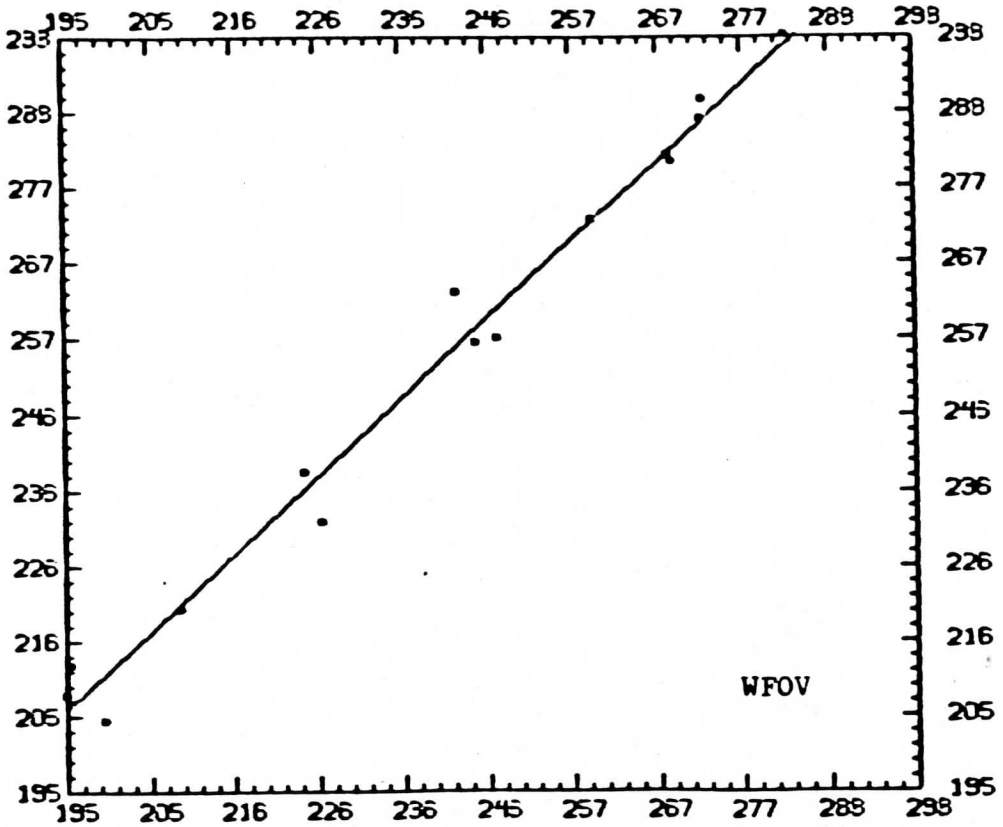


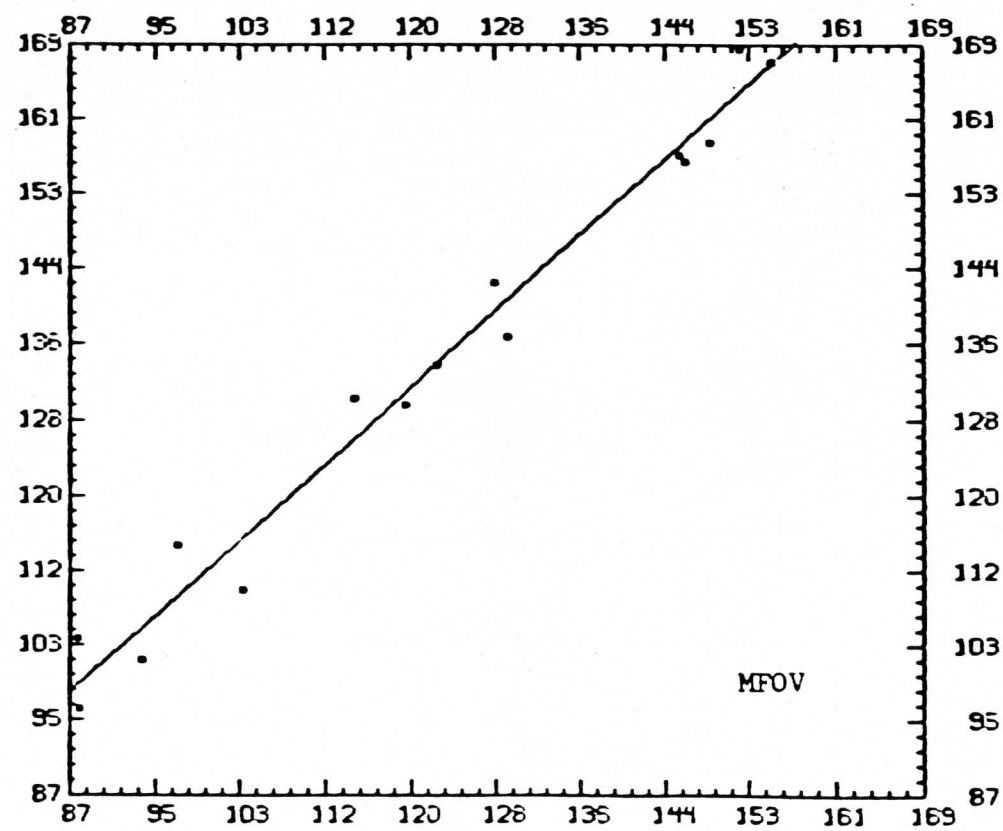




(c) Morning, SW

Horizontal : OBS  Vertical : SML  Unit : $W/m^2$

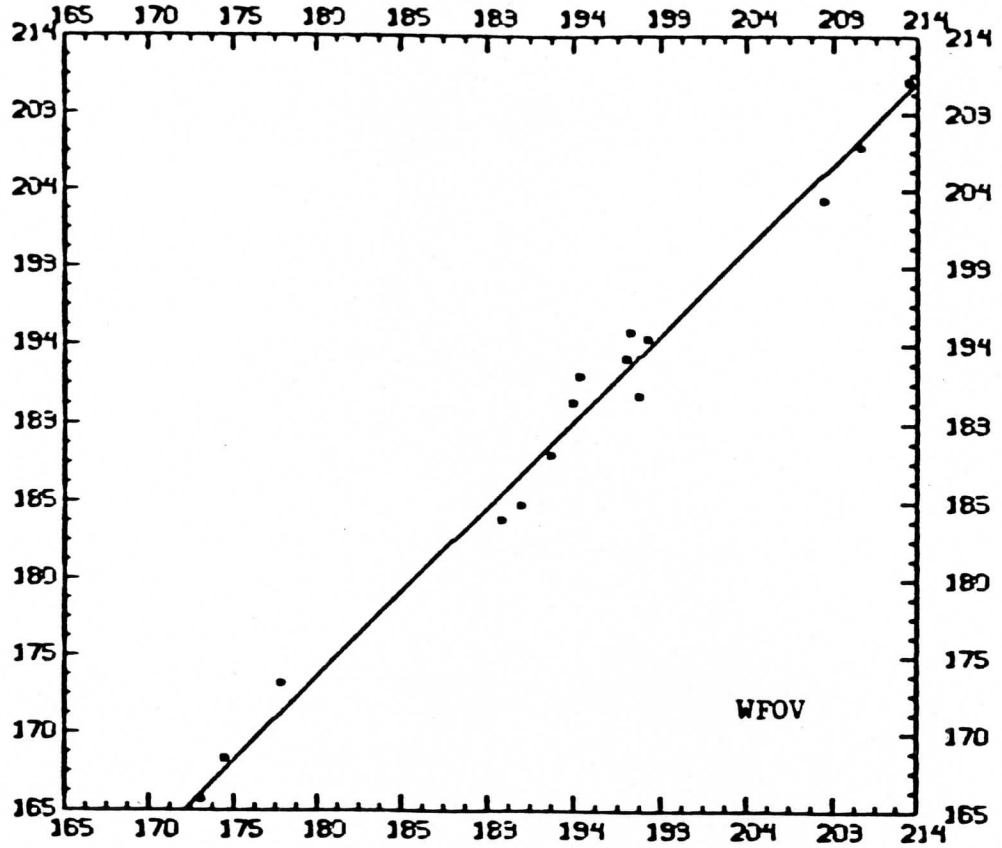


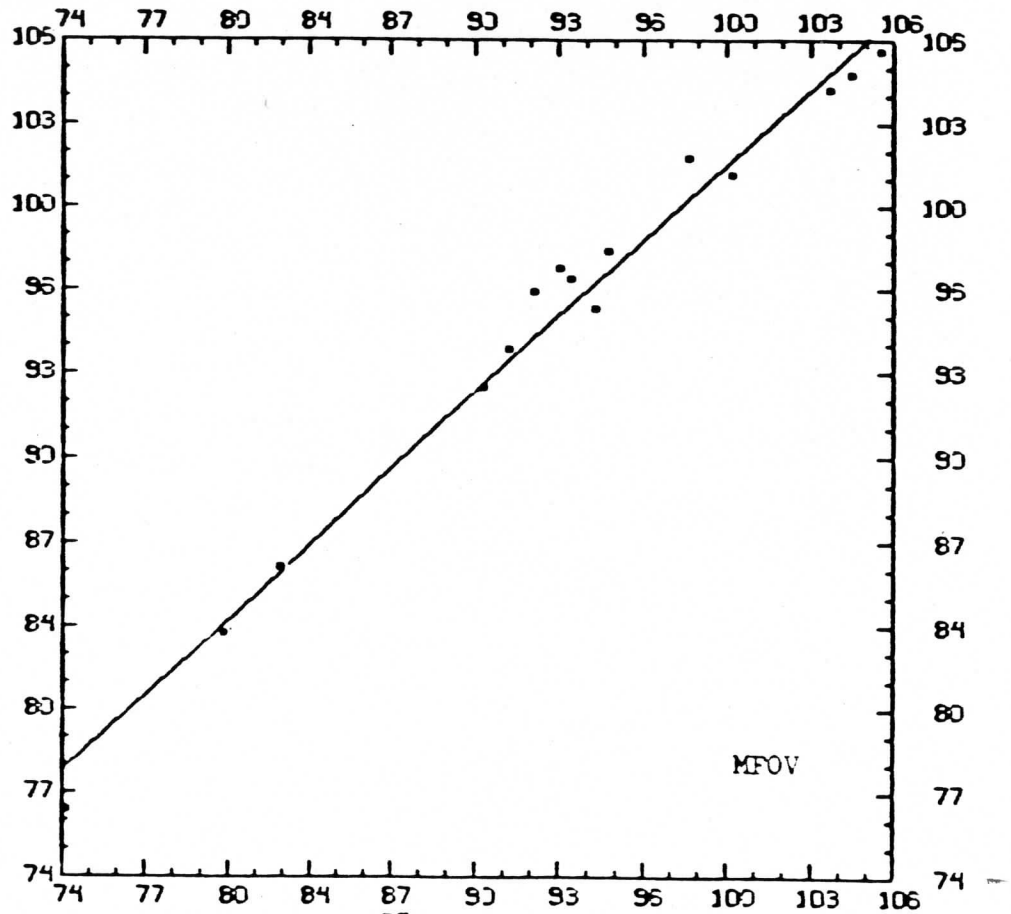




(d) Morning, LW

Horizontal : OBS  Vertical : SML  Unit : $W/m^2$

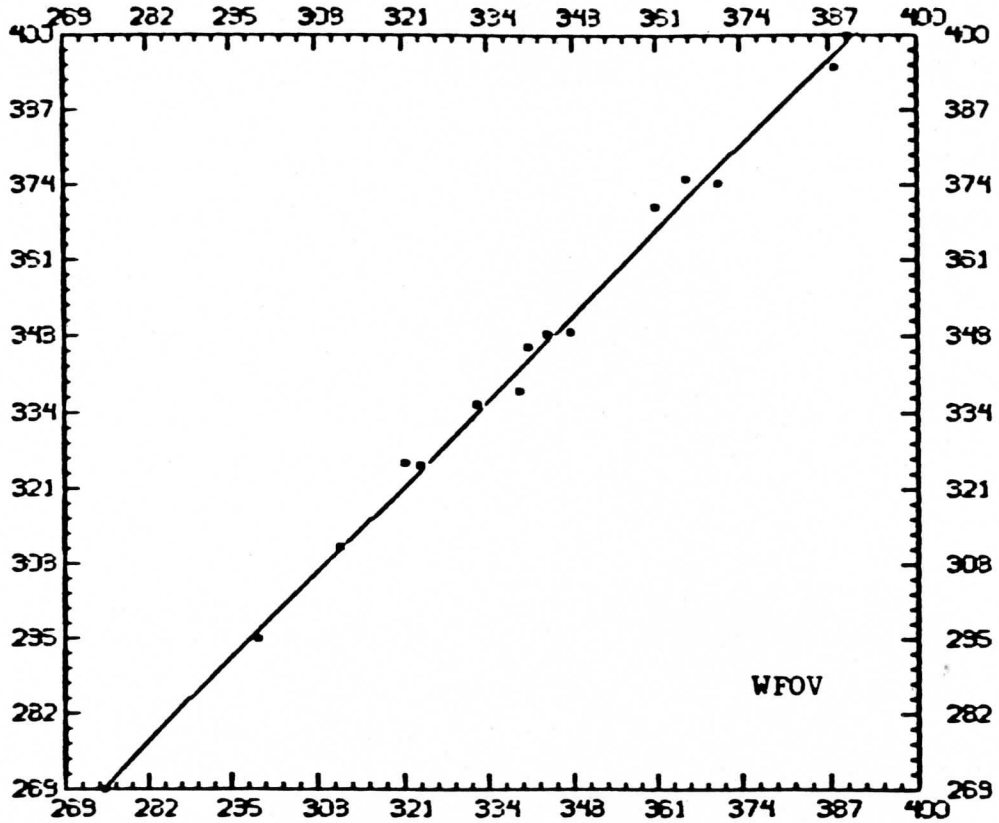


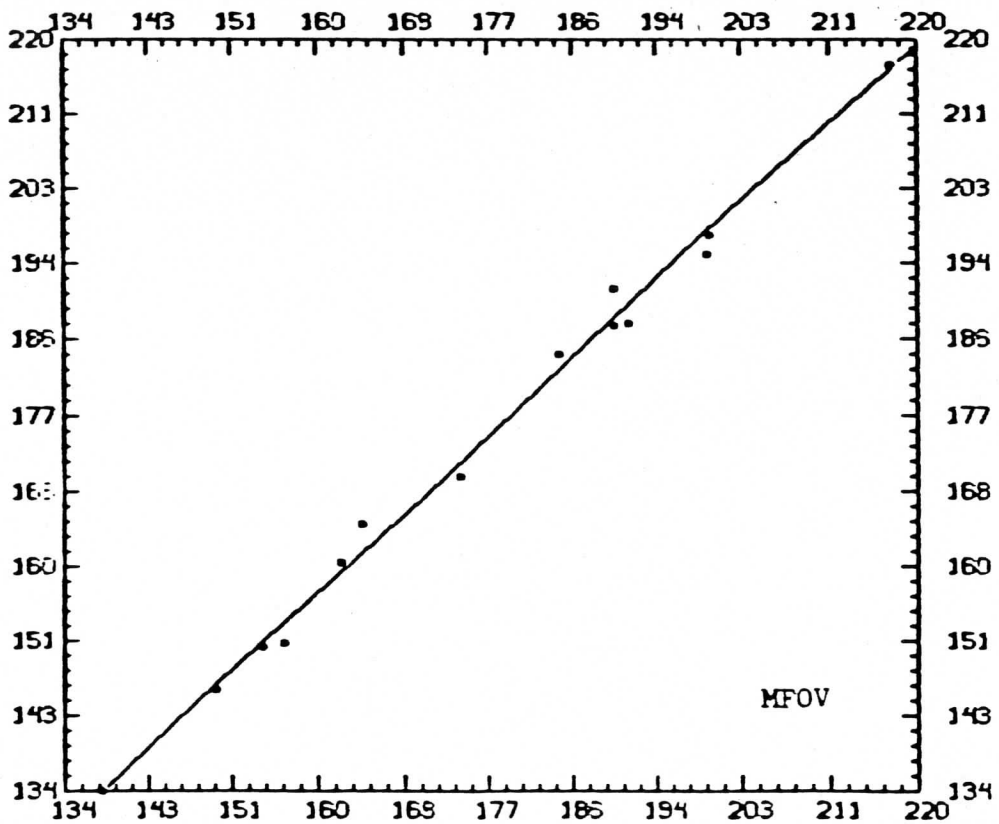


(e) Noon, SW

Horizontal : OBS  Vertical : SML  Unit : $W/m^2$

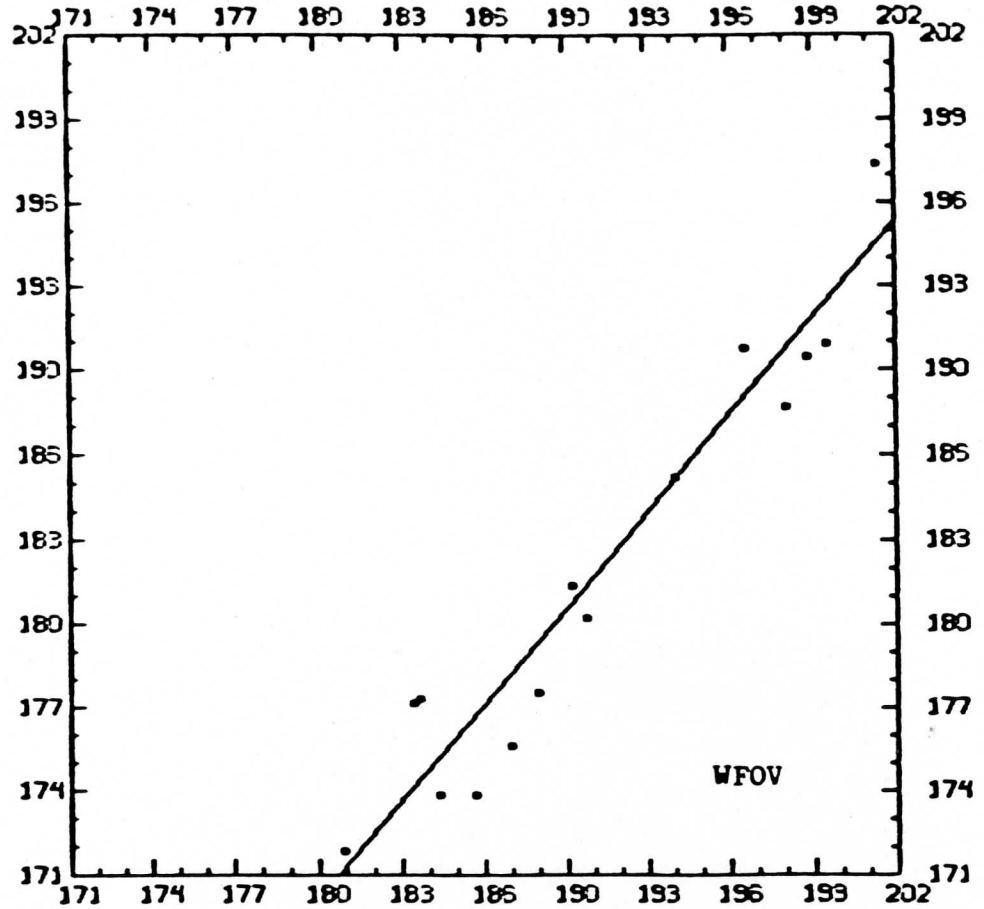


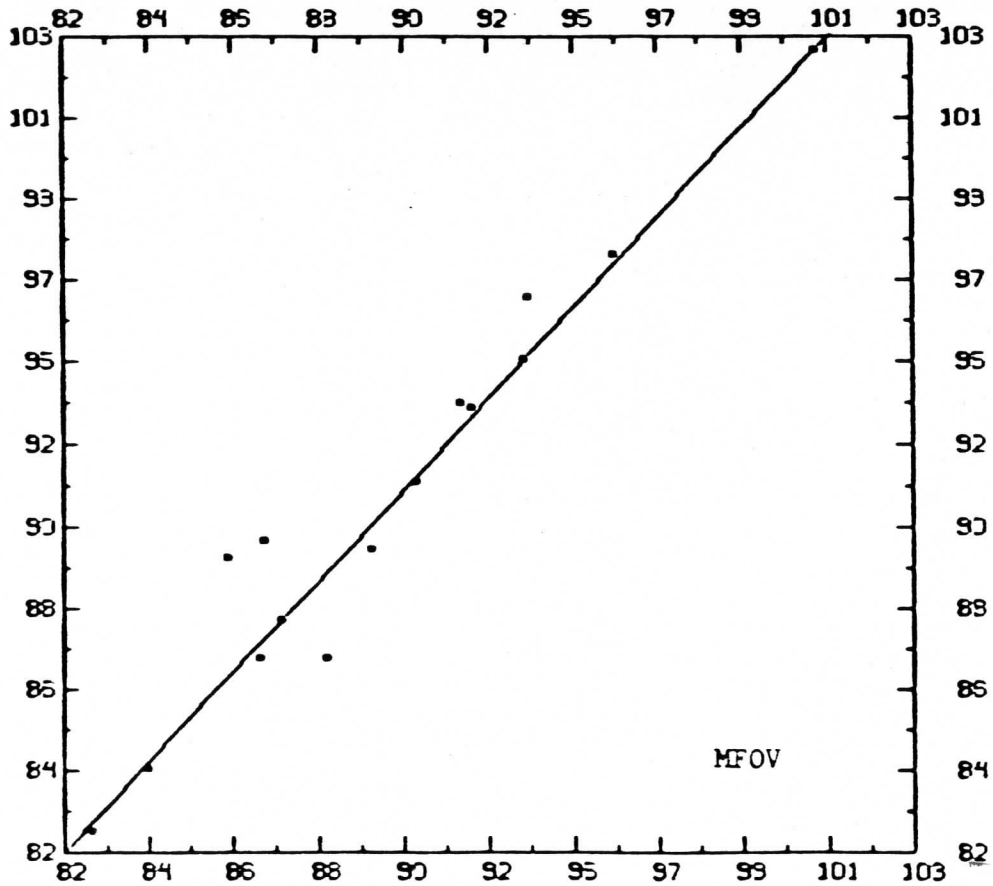




(f) Noon, LW

Horizontal : OBS  Vertical : SML  Unit : $W/m^2$

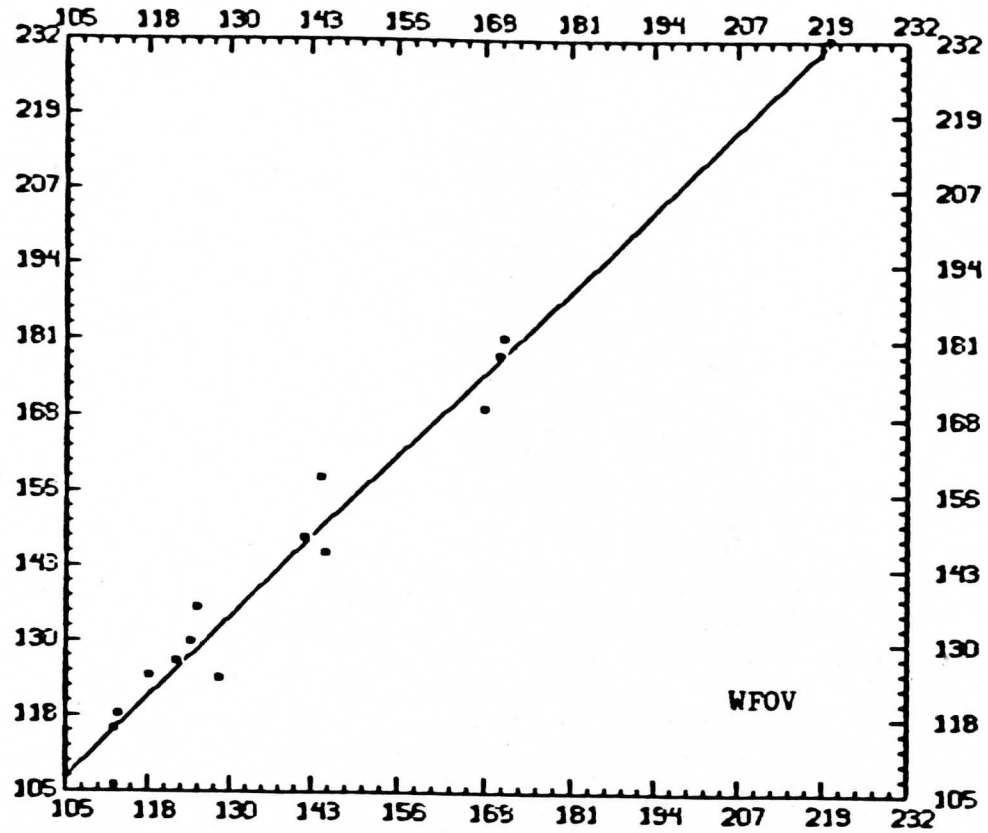


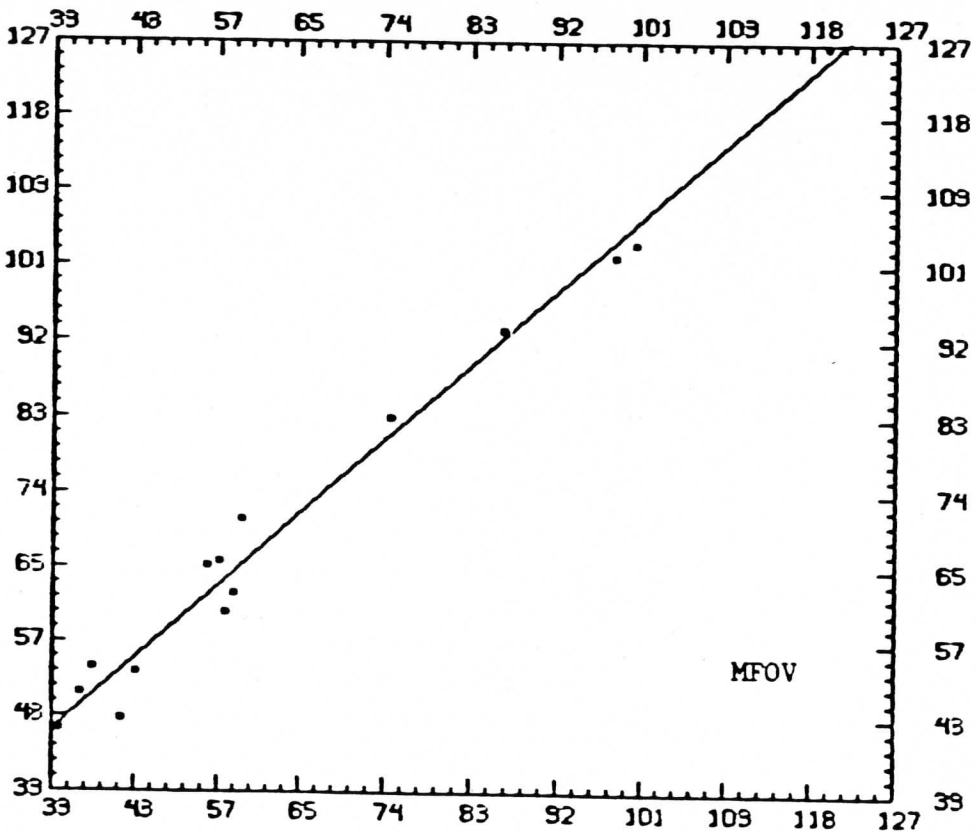




(g) Evening, SW

Horizontal : OBS  Vertical : SML  Unit : $W/m^2$

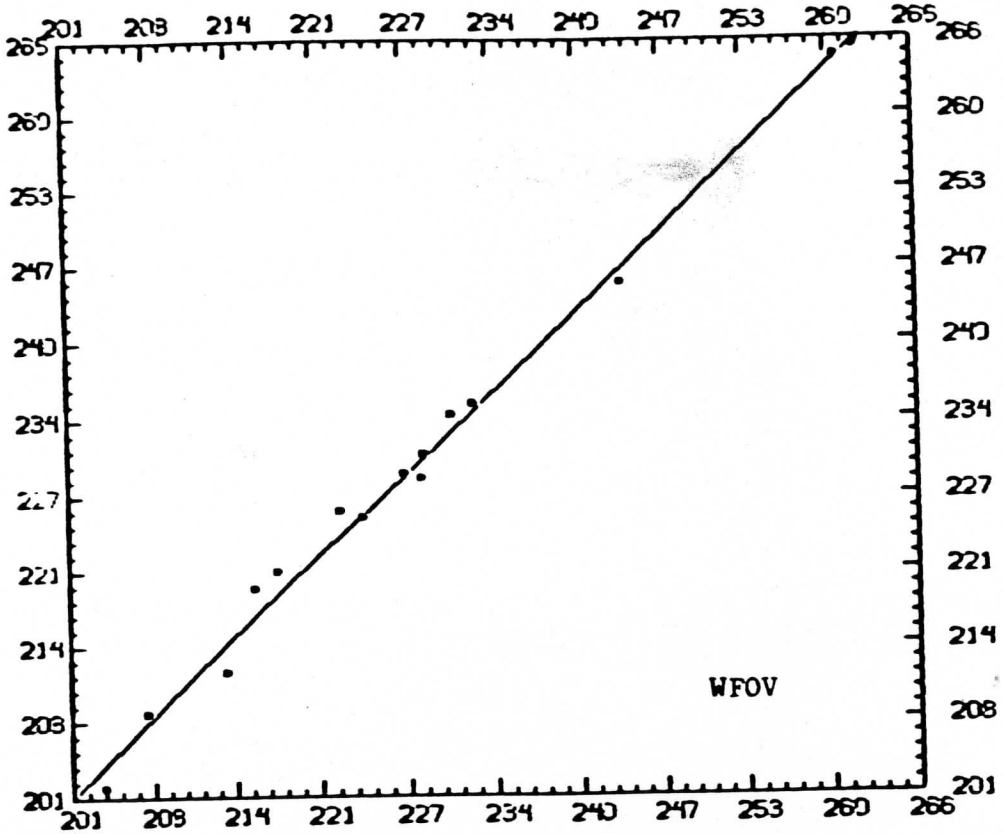


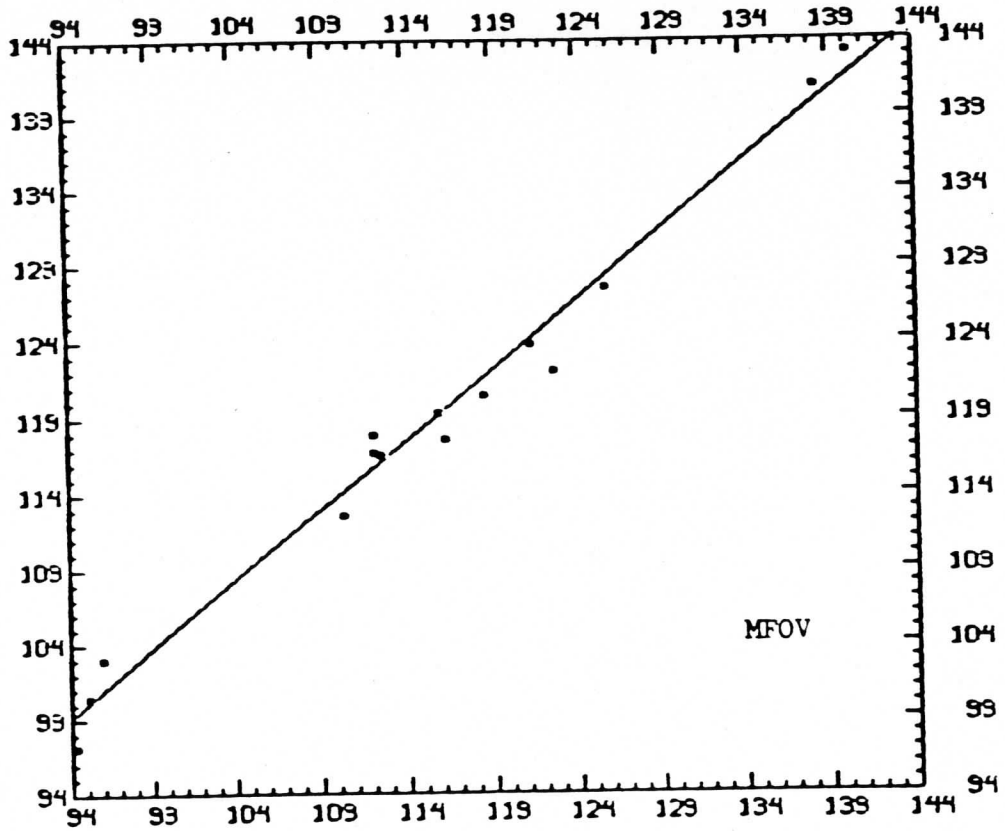


(h) Evening, LW

Horizontal : OBS  Vertical : SML  Unit : $W/m^2$

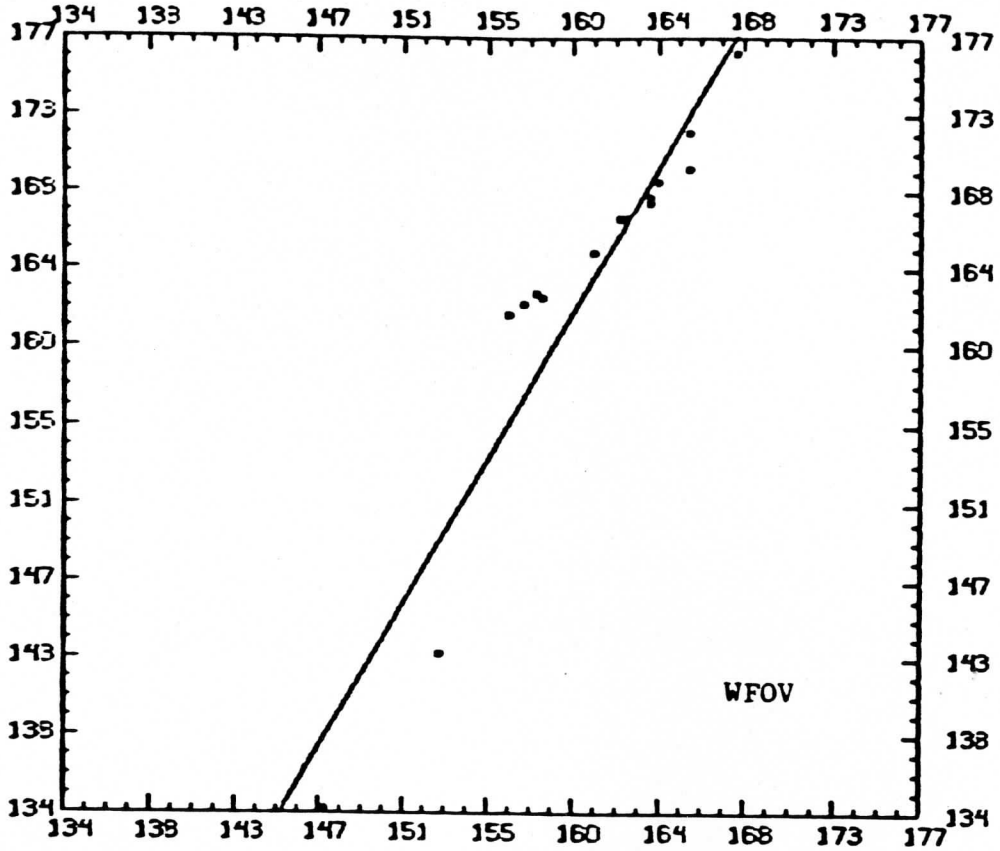


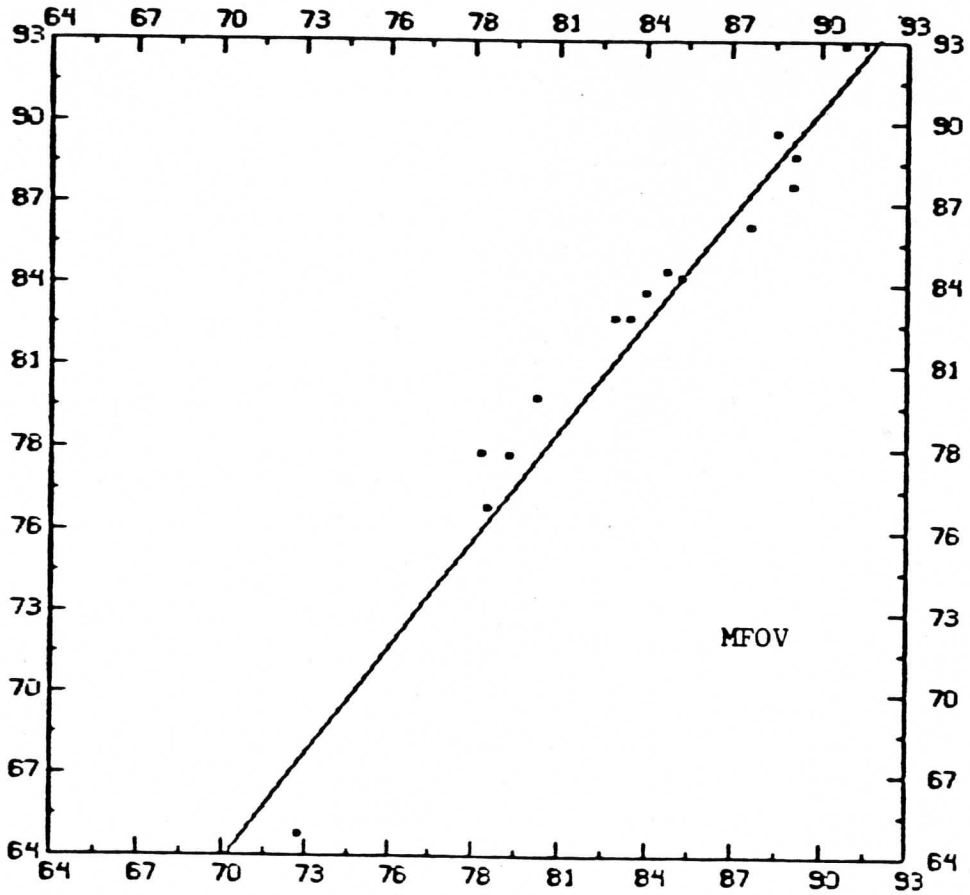

The first group of comparisons, "Entire Orbit", serves as an ensemble validation, which demonstrates that the simulations agree very well with the nonscanner observations. The largest absolute difference of 7.1 $W/m^2$ is excellent in view of the standard deviations of the flux values (73.6 $W/m^2$ for observations and 75.6 $W/m^2$ for simulations) in this sample. The agreement between the observation and simulation is further confirmed by the relative difference of all 18 comparisons, which ranges from 0.0% to 8.8% with the weighted average P:

$$P = \frac{\sum_i Pi * Ni}{\sum_i Ni} \qquad (3\text{-}1)$$

as small as 1.9%, where Pi is the relative difference of the i'th comparison (in terms of percentage) and Ni is the sample size of that comparison. The linear correlation coefficient is also very encouraging: 11 out of the 18 are better than 0.99 and the weighted average is as high as 0.98. It should be noted that the comparisons are between instantaneous (observed and simulated) radiation fields. If the integrations are made and averaged over a much longer time period, say a month for typical climatic studies, difference between

the observation and simulation should be reduced significantly.

In general, the observation and simulation are well correlated. It is the "offset errors" which are not very satisfactory. (The word "very" is used in the light of the statistical test, which says, with the predefined confidence, that any fluctuations are more likely due to the random sampling process.) Three features are noted. The first one is that the simulated shortwave irradiance is larger than the observed flux in most cases (Table 2). This discrepancy may originate from two sources. One is the algorithm itself, namely, how well it has sampled the radiation field observed by the nonscanners. This discussion will be deferred to Section 3.3. The other possible source of error is the bidirectional model of angular dependence of shortwave radiation. That model has been revised twice at NASA Langley Research Center while this research was in progress, and a new version is forthcoming. Significant improvements have been noted (but not detailed here) by this algorithm in using new versions of angular models; therefore one may reasonably expect further improvements.

Another feature is that, as far as the "offset error" is concerned, the simulated longwave irradiance agrees better with the observation than that of shortwave. So does the "Entire Orbit" comparison than the "local time" comparisons, the latter seem to have a different bias for different simulation. The first part of this feature is plausible since the angular dependence of longwave radiation is simpler and better known than that of the shortwave radiation. The meandering of the bias could be attributed to the scene types, the intensity of the irradiance field, etc., but no conclusion can be drawn before data from other days and satellites are analyzed. Also, it is relevant to mention here that the reason that the comparison for Noon, LW,WFOV failed to pass the Student t-test is due to the difference in the means. The null hypothesis is that the two samples are from the same population, or $\mu_{OBS} = \mu_{SML}$ and $\sigma_{OBS} = \sigma_{SML}$. Although the simulation "imitates" the observation quite well in many ways, reflected by standard deviation and correlation coefficient and Fig.7, the large difference in their mean values is decisive.

One last point is that the two comparisons for "Night" are the only ones possessing significant "slope

errors". It seems that this is mainly caused by two data (having the smallest simulated values in both panels in Fig.7(1)), which are from the first two pivot records of the first orbit. If they were removed from the data set, the "slope error" would almost disappear and other statistics would also be better. It is likely that those anomalous data have errors. However no attempt has been made to avoid using those data after they are chosen, and more effort is required to explain and correct suspected erroneous data.

## 3.3 Conclusions

A cross validation algorithm is developed to intercompare scanner and nonscanner data from the Earth Radiation Budget Satellite. Based on spherical geometry, the algorithm transforms the original geographic coordinate, in which all ERBE data are specified, to another one, in which the solid angle integration is greatly simplified. In general, the simulated irradiance from scanner observations agree very well with the nonscanner observations in both their intensity and distribution. For 18 comparisons, the relative difference is from 0.0% to 8.8% with a

weighted average of 1.9%; the linear correlation coefficient is from 0.9495 to 0.9975 with a weighted average of 0.9820; Student t-tests are verified at a level of significance of 0.1 with only one exception. These results are even more encouraging in view of the variety of conditions that the data span, including scene types, solar zenith angles, and the intensity of the radiation fields.

An important limitation of those results is that the emphasis of the research is the relative difference of the scanner and nonscanner data of the ERBS, i.e., to see how consistent those data are. Undoubtedly the nonscanner data have noise, as well as the scanner data. It is possible that some of the disagreement (or agreement) between the simulations and observations is just due to those random errors. An absolute measure of the errors in scanner or nonscanner data is much needed indeed, but it is not presented here. Also, errors in the simulation may originate from any link of the data stream (calibrations, count inversion, unfiltering, bidirectional model, and the algorithm of integration), meanwhile error cancellation and/or amplification may occur. In that sense, this work is a overall error analysis of the ERBE data product.

One improvement to the algorithm is the better representation of the WFOV by scanner data. This algorithm has attempted to divide the FOV into "best" angular bins while rendering the scanner data more homogeneous. Previously, another algorithm was examined which tries to calculate the overlap of NFOV's and thus the net solid angle each scanner datum represents. That algorithm failed to produce reasonable results, which proves that this algorithm is better. However, this "better" algorithm may be optimized further. For example, one could impose some kind of grid mesh on the FOV. The angular distance between the grids is of course well-defined (e.g., homogeneous). One could then interpolate the radiance at those grid-points via some sort of objective analysis, and the integration will be similar as Eq.(2-11). This approach has not yet been tested.

A better bidirectional model of angular dependence of radiation is another avenues to improve this algorithm. It is interesting to note that this algorithm may be used to improve the bidirectional models as well. Choosing pivot records with consideration of solar zenith angle, scene types,

radiation intensity, etc, some evidence may be collected to identify the bias under those conditions. The "Local Time" comparisons were so oriented, but as indicated in Section 3.2, the available data were too few to make suggestions.

This research performs only an intercomparison between scanner and nonscanner radiometers of ERBS. Although the same algorithm may be applied to other ERBE satellites as they become available, one could also use a revised algorithm for comparison with other radiance data from other platforms, such as those in a geostationary orbit. The significance of such comparisons is that one can use geosynchronous sensors as monitors to provide sufficient temporal resolution over a limited area for the study of diurnal variation of the earth radiation budget parameters.

REFERENCES:

Barkstrom, B.R. and G.L. Smith, 1986 The Earth Radiation Budget Experiment: science and implementation. To appear in: Rev. Geophys. Space Phys.

Hall, J.B., 1983 Earth Radiation Budget Experiment (ERBE): Validation Plan. Report ERBE 2-2-9-0-83-01-00. NASA Langley Research Center, Hampton, VA.

Spiegel, M.R., 1975: Theory and Problems of Probability and Statistics. 327pp., McGraw-Hill Book Co., U.S.A.

Taylor, V.R., and L.L. Stowe, 1984: Reflectance characteristics of uniformed earth and cloud surfaces derived from Nimbus-7 ERB. J. Geophys. Rev., 89, pp.4987-4996.

Yang, D.S., Y.B. Liu, S.S. Liu, 1980: Dynamic Meteorology. 423 pp., (in Chinese). Meteorology Press, Beijing, China.

# A Comparison of ERBS and GOES IR and Visible Data

Leroy D. Herman

NESDIS - CIMSS

University of Wisconsin

Madison, Wisconsin

March 18, 1985

15th ERBE
Science Team Meeting

# A Comparison of ERBS and GOES IR and Visible Data

One objective of the ERBE Science Team to be achieved early in the life cycle of the first satellite is to validate the data. For this purpose, comparison of the data with data from other satellites is necessary. A small sample of ERBS scanner data has been examined for both the long wave and short wave channels.

A. Long Wave Case - 0000Z

The first orbit on the November 9, 1984 ERBS data tape begins at 0000Z over Central America. The satellite moved northeastward across the eastern U.S. more or less parallel to the coast. The cloud cover on this segment of the orbit is seen in figure 1. Some regions appear to be virtually cloud free such as the southeastern U.S., Maine, and the Maritime provinces of Canada.

The same distribution of cloudiness is also seen in the GOES infrared picture shown in figure 2. Good resolution on the east coast in the ERBS picture permits comparison with the GOES picture eastward to Lake Erie in the northern U.S. and as far west as Louisiana in the southern U.S.

Ordinarily for comparison purposes it would be sufficient to specify a cloud's position for pictures so nearly simultaneous, however, the GOES itself was moving during this period, so navigation was not reliable enough to use that technique. Instead, the same target or cloud was located in both pictures according to its visual pattern similarities. One problem in comparing these two types of data is the difference in resolution between the two data types. The scanner resolution is approximately 36x48 km, while the GOES data is only 8 km. In order to overcome this disparity, sample points were chosen in areas where there were uniform fields.

When this technique was followed, the scatter diagram shown in figure 3 was obtained. The top of the atmosphere scanner values were converted to temperatures according to the Stephan-Boltzman Law and form the abcissa on the diagram. The fit of the regression line is quite good for the 32 points except for the two obvious exceptins below the regression line. Examination of the data showed the point furtherest out of line is from a small cloud found near 32N, 80W, and the second worst point is from a cloud at 31N, 78W. Apparently both of these two clouds are less than the spot size of the scanner and were warmer than the 8 km resolution of the GOES due to radiation from the surface or from lower cloud tops in the vicinity.

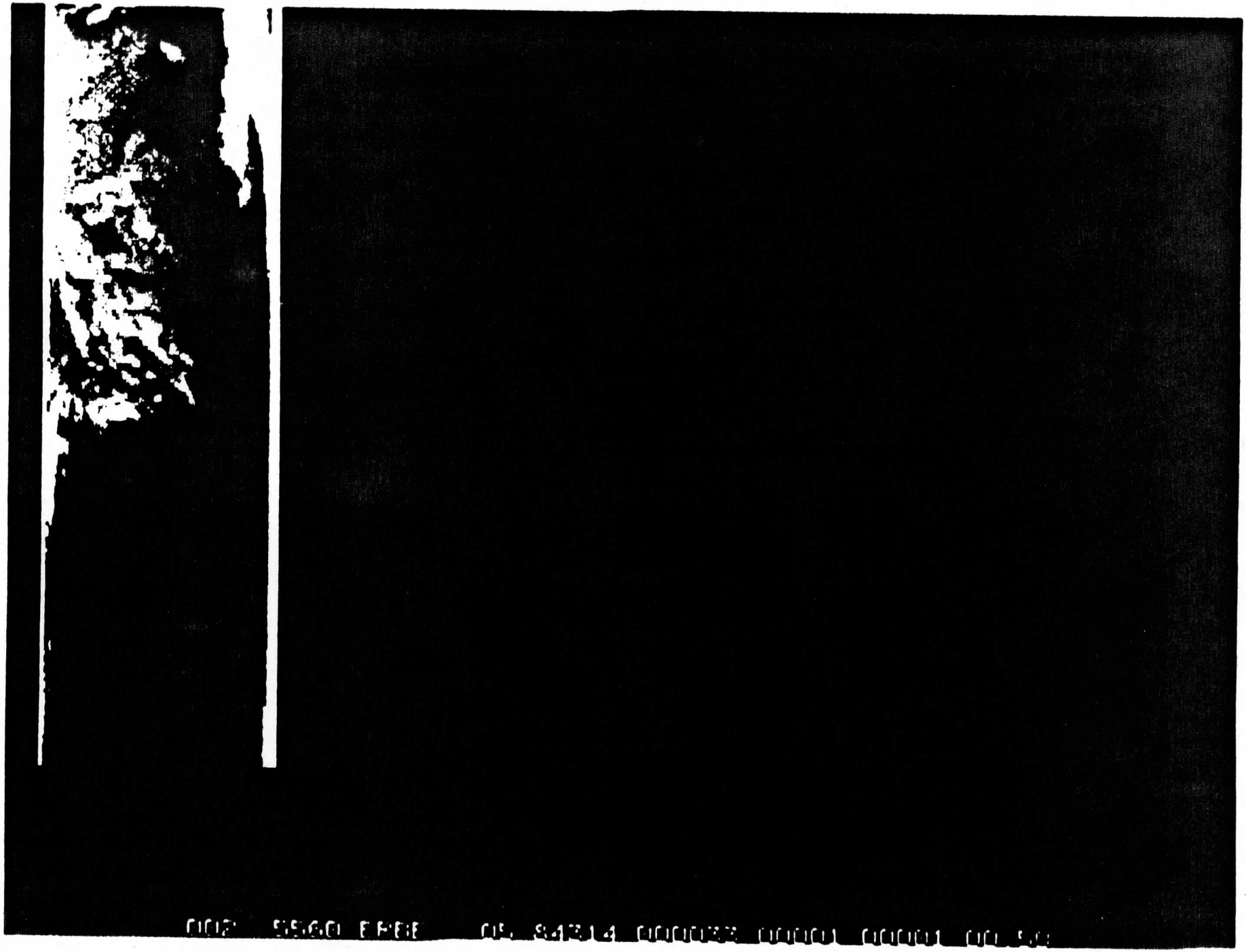

Figure 1. ERBS long wave pass - November 9, 1984 0000Z

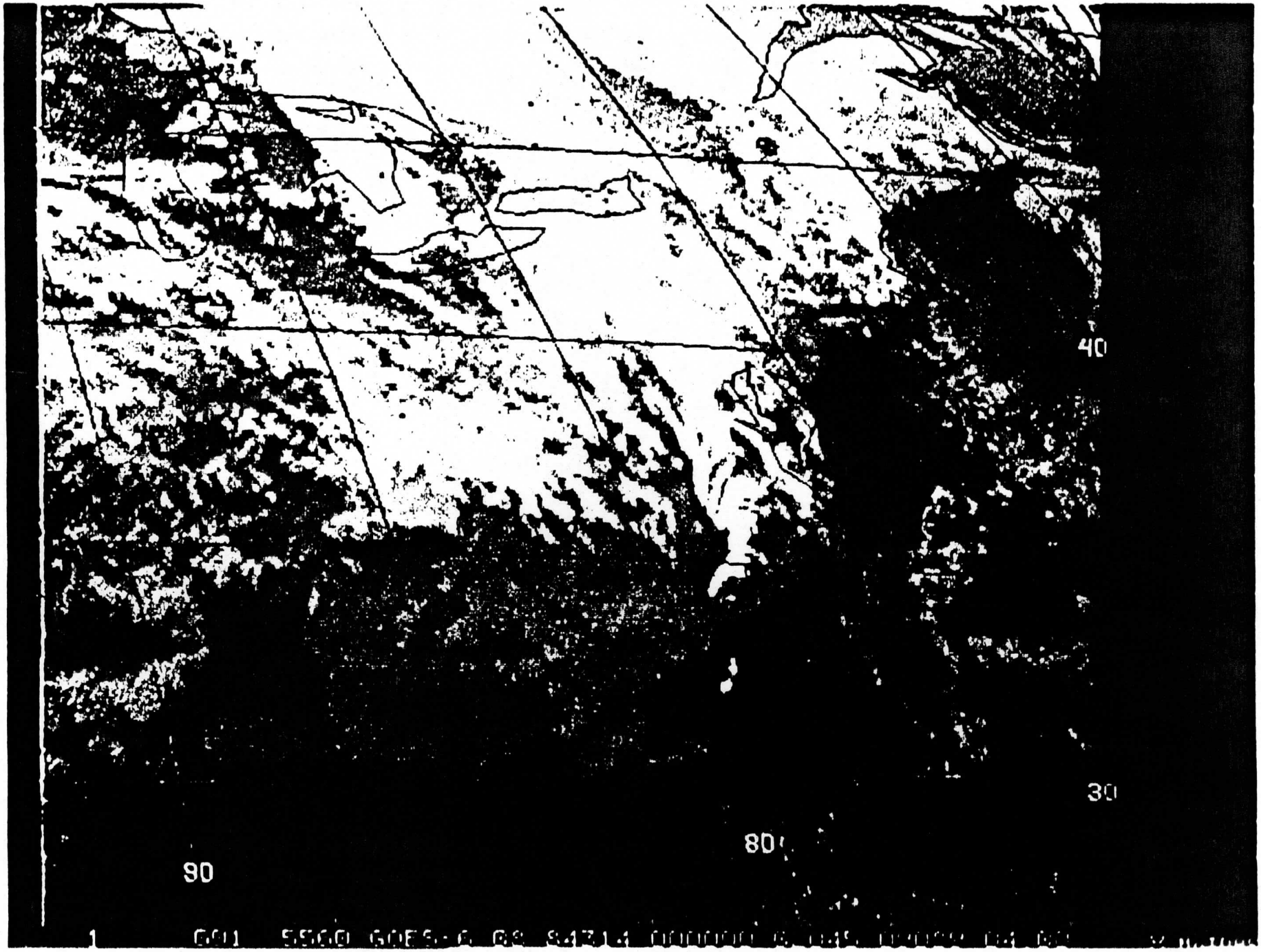


Figure 2. GOES IR for November 9, 1984 0000Z

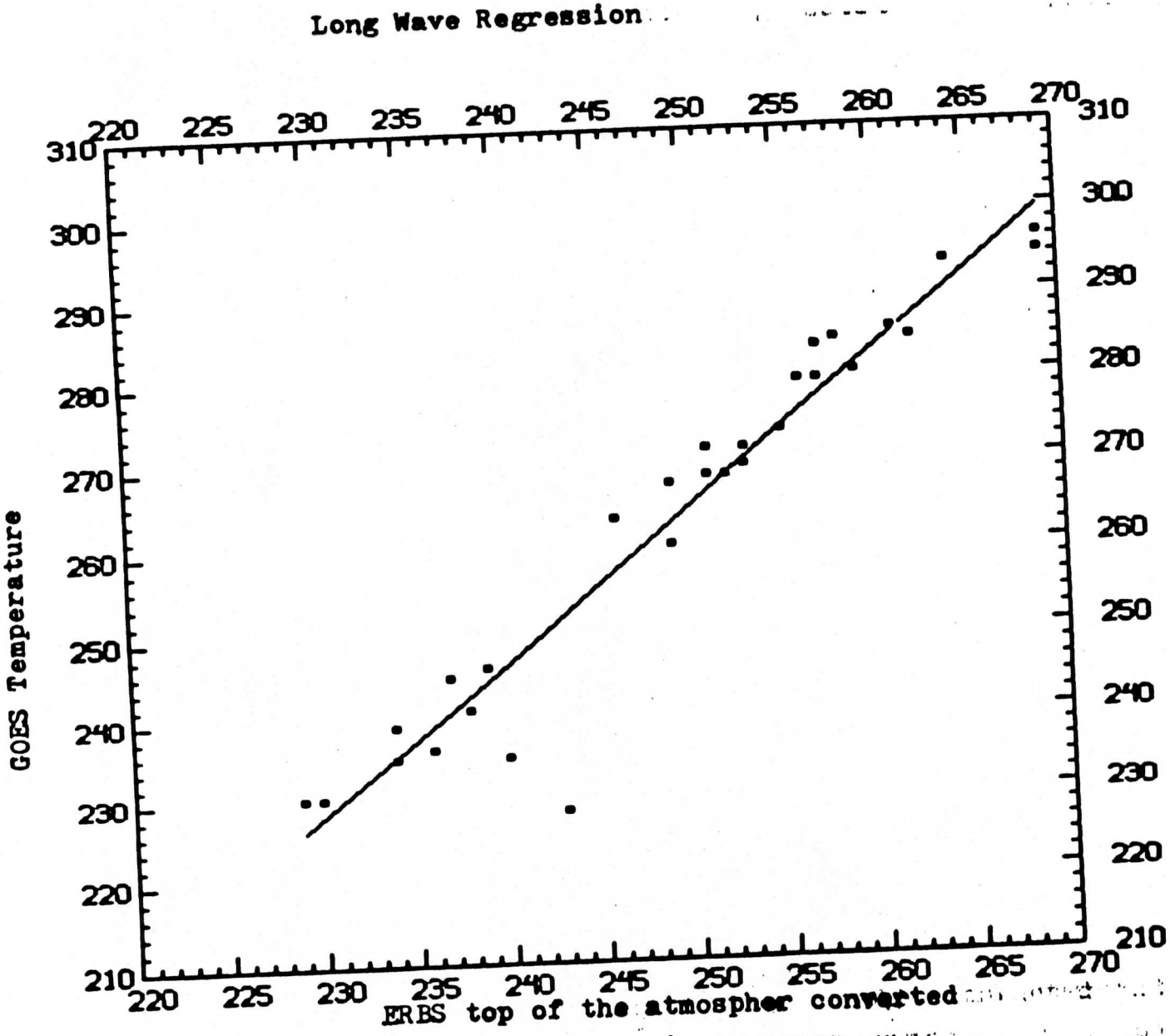


Figrue 3. Long wave regression

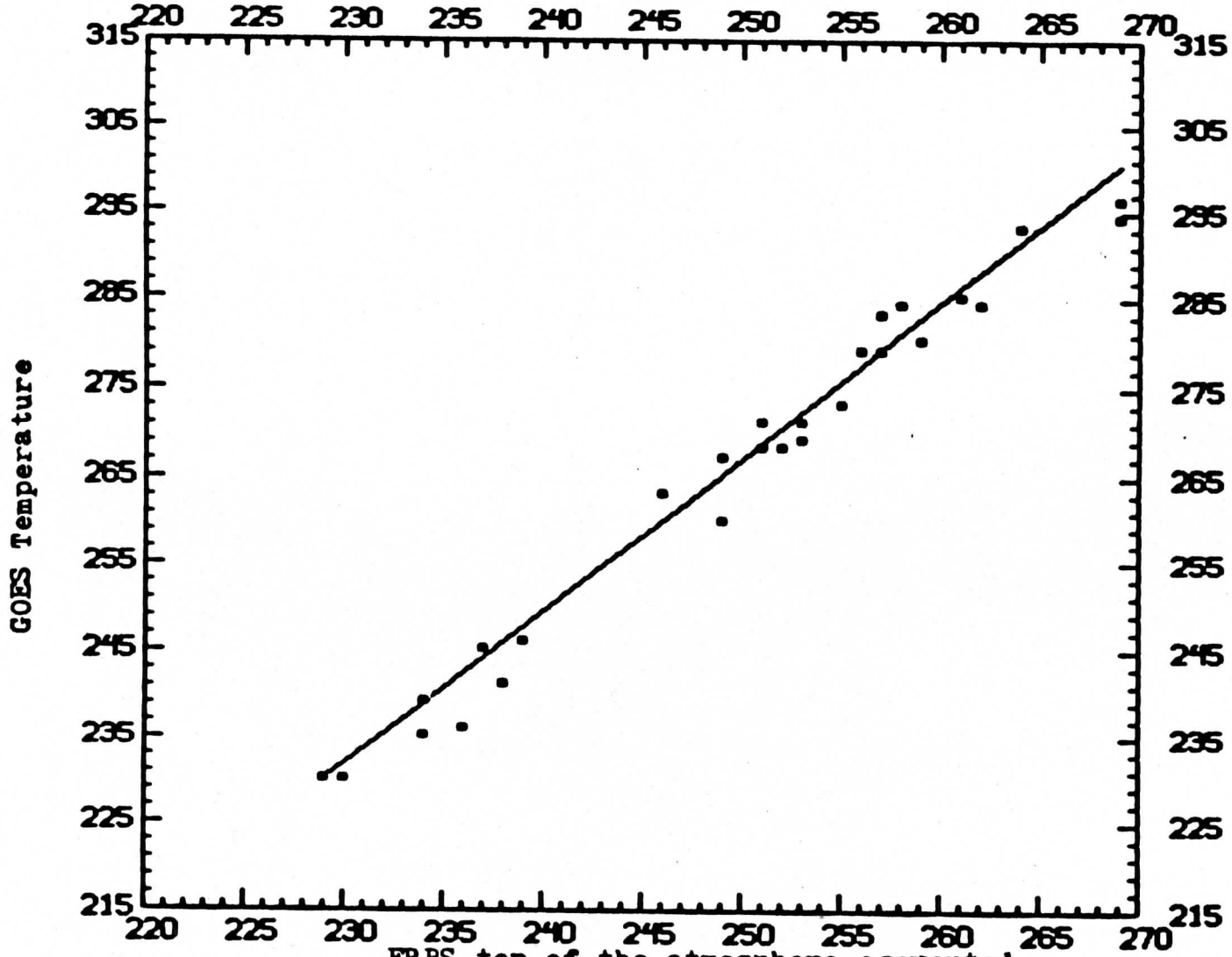


Figure 4. Long wave regression corrected.

R = .9927

N = 30

Figure 4 shows the recomputed regression line found after eliminating the two questionable points. The fit of these points is remarkable, when it is considered that no corrections to the GOES data to account for the differences in processing have been made. Certainly, limb darkening due to water vapor absorption on the warm end of the scale should be a significant factor.

B. Short Wave Case - 1907Z

The only short wave data on the first tape is to be found in the southern hemisphere. A sample of ERBE short wave scanner data was selected over Brazil for comparison with the GOES visible data at nearly the same time. These are shown in figures 5 and 6. The principal clouds in these pictures are either part of cumulonimbus clusters or small-element low level cumulus. Figure 7 shows the GOES IR does indeed have cold-topped cumulonimbus and unresolvable cumulus, even for 8 km resolution data. Consequently the ERBS short wave appears virtually clear south of the cluster.

In order to compare the two data presentations, a procedure similar to that used for the selection of the long wave data was followed. The result of matching points is shown in the scatter diagram of figure 8. Here the ordinate is scaled to an energy quanity by squaring the GOES gray scale count. In this case such simple processing, without refinement such as using bi-directional reflectance corrections, produces a less desirable result. Evidently more work must be done.

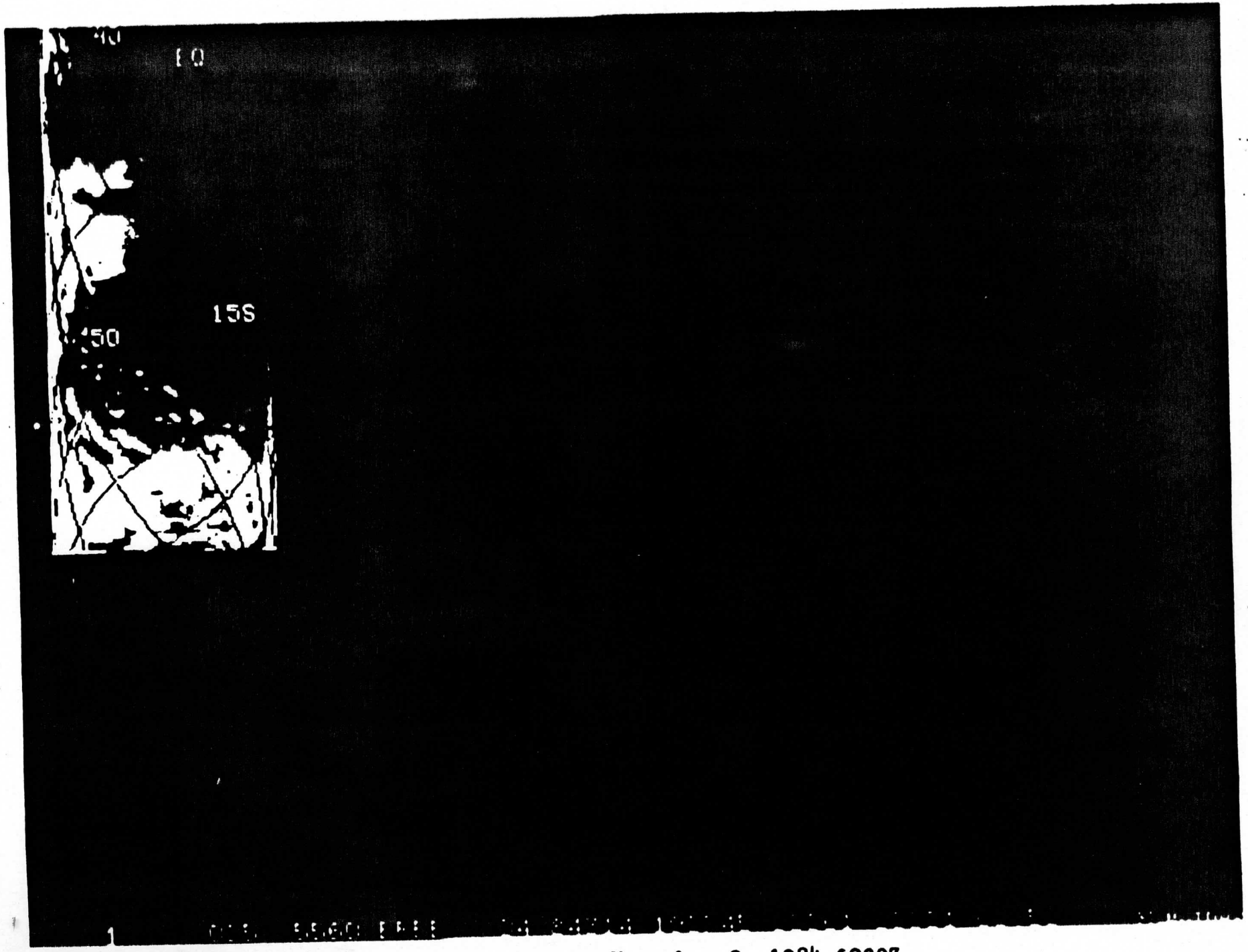


Figure 5. ERBS short wave pass - November 9, 1984 1900Z

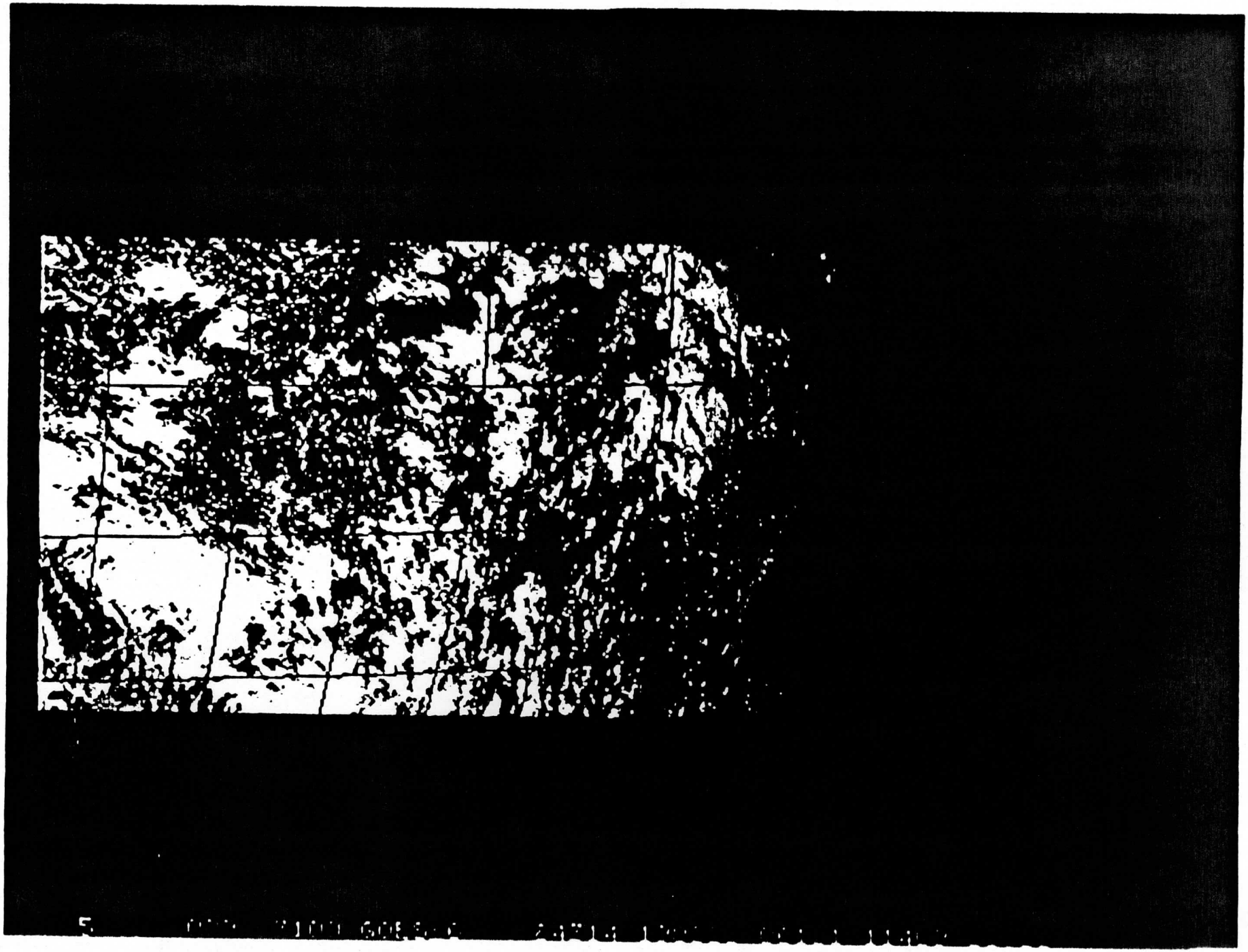

Figure 6. GOES visible for November 9, 1984 1900Z

Figure 7. GOES IR for November 9, 1984 1900Z

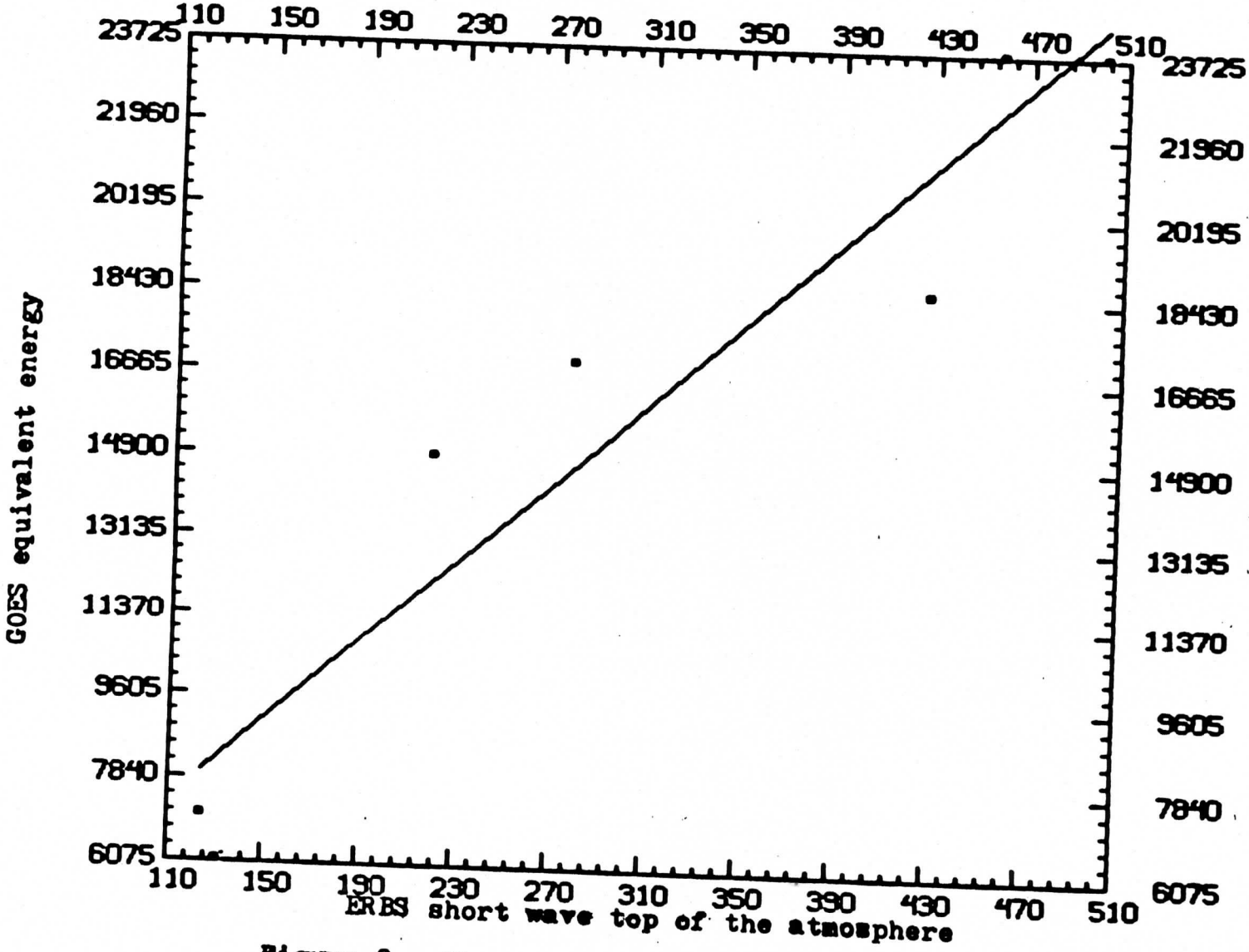


Figure 8. Short wave regression

# A Quick Comparison of ERBS Landmarks on November 9, 1984

Leroy D. Herman

NESDIS - CIMSS

University of Wisconsin

Madison, Wisconsin

March 14, 1985

15th ERBE
Science Team Meeting

L. Herman
Madison WI

# A QUICK COMPARISON OF ERBS LANDMARKS ON NOVEMBER 9, 1984

The verification of positions within ERBS pictures is necessary for confidence in the geographic information contained on ERBS tapes. The geographic coordinates on these tapes should provide accurate positioning information within the limits of the scanner resolution. The work reported here is a preliminary evaluation of that accuracy on a quick-look basis.

## A. Visible Case - 1900Z

The first ERBS tape released by NASA-Langley was for data gathered by the satellite on November 9, 1984. Although this tape has orbits of infrared data from the scanner in both hemispheres, visible data is available only in the southern hemisphere. Examination of the track of the satellite indicated it passed over the southern portion of South American traveling in a northeasterly direction beginning at approximately 1900Z. Figure 1 shows the western hemisphere tracks as mapped on McIDAS.

A display of this pass showed clear skies in portions of the region from 25° south to near 42° south. Enhancement of this area of the picture allowed several landmarks to be selected for determination of accuracy of location. A National Geographic Atlas was consulted and the landmark locations were found prior to checking their corresponding ERBS position. Postional accuracy using the atlas to estimate actual earth locations was no better than 2 nmi.

The procedure was: (1) select a landmark that could be seen in both the satellite picture and the atlas; (2) determinte its geographical location in the atlas; (3) determine its position in the picture; and (4) compare the two. If these locations agree within a half degree or better, this location was recorded as shown in Table 1a.

The average error in positioning was found to be 13.0 nmi. This is not a large error in view of the following analysis: if we take the scanner resolution to be 36 x 48 km and assume the worse case, that is, a landmark falls midway between the center of two picture elements on two different lines, then a mislocation error of 18.3 nmi occurs. Hence, we can say the average error in these measurements is not excessive for the given resolutions.

Of course, judicious care must be exercised in choosing landmarks. Preferably, they should be large enough to be resolved, but not loo large to easily find the center of the pattern. The landmarks found in this case are reasonably close to this standard and permitted good results to be obtained. The choice of landmarks is frequently limited by cloudiness so "targets of opportunity" are sometimes necessary. In addition, when a landmark is split into two lines or two pixels finding its position becomes uncertain. Replication of these results, it has been found, depends on having the right enhancement of gray scales.

B. IR Case - 0033Z

On the first orbit on November 9, land-water temperature contrasts are fairly strong in the IR in the Saudi Arabia region. The same procedure for comparisons was followed as in the visible case and the results are shown in Table 1b. In Saudi Arabia, the chosen landmarks are points of land on the southeast coast that project into the Arabian Sea and are evident in the ERBS picture. Here the average error amounts to 15.3 nmi, which is still under the practical worst case value of 18.3 nmi.

C. Summary

These two cases provide some initial information on the reliability of the geographical positioning of the ERBS scanner data. The sample of visible geographic landmarks gives an indication that the positioning is acceptable. The sample of infrared landmarks gives a similar indication. Because they were made in different parts of the world and at different times, suggests similar results on other passes can be obtained when good landmarks are chosen.

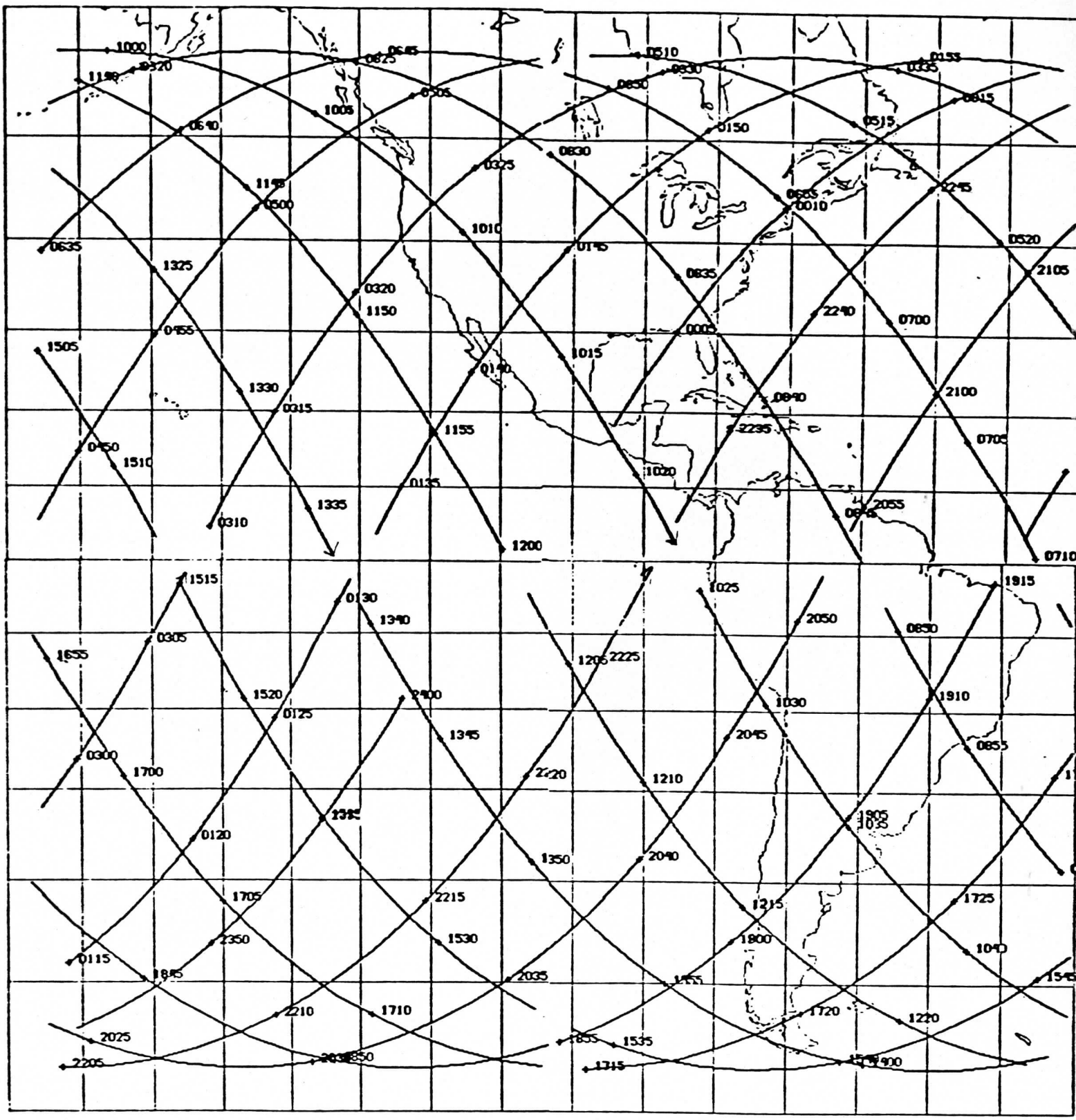


Figure ]. ERBS Orbit Tracks

Table 1a.

ERBS LANDMARKS
November 9, 1984

Visible S. America 1900Z

| | Map Est. Position Lat | Lon | ERBS Position Lat | Lon | (nmi) Error | Landmark Feature |
|---|---|---|---|---|---|---|
| 1. | 30.72 | 62.62 | 30.58 | 62.47 | 11.4 | Laguna Mar Chiquita (center of lake) |
| 2. | 30.72 | 62.84 | 30.42 | 62.68 | 18.7 | Laguna Mar Chiquita (west end) |
| 3. | 30.72 | 62.25 | 30.73 | 62.26 | 0.8 | Laguna Mar Chiquita (east end) |
| 4. | 30.22 | 50.91 | 30.02 | 51.20 | 21.1 | Lagoa dos Patos (north end) |
| 5. | 35.37 | 57.42 | 35.24 | 57.16 | 15.5 | Punta Piedras |
| 6. | 41.06 | 62.73 | 41.17 | 62.80 | 7.5 | Negro River mouth |
| 7. | 39.87 | 62.26 | 39.60 | 62.30 | 16.3 | Bahia Union Bay (north end south branch Colorado River mouth) |

Average Error = 13.0 nmi

Over S. America at Lake Mar Chiquita

1 scan line goes from: 30.58 62.47
to: 30.40 62.28
change = 13.6 nmi

Table 1b.

IR Saudi Arabia 0033Z

| | Map Est. Position Lat | Lon | ERBS Position Lat | Lon | (nmi) Error | Landmark Feature |
|---|---|---|---|---|---|---|
| 1. | 17.26 | 55.27 | 17.10 | 55.07 | 14.9 | Ra Mirbat |
| 2. | 17.89 | 56.33 | 18.05 | 56.15 | 14.1 | Ra ash Sharbatat |
| 3. | 19.02 | 57.67 | 18.84 | 57.44 | 17.0 | Ra al Madrakah |

Average Error = 15.3 nmi

Over Arabia near Ra Mirbat

1 scan line goes from: 17.10 55.07
to: 16.91 55.21
change = 14.94 nmi

**UNITED STATES DEPARTMENT OF COMMERCE**
**National Oceanic and Atmospheric Administration**
NATIONAL ENVIRONMENTAL SATELLITE, DATA, AND INFORMATION SERVICE
Washington, D.C. 20233
Systems Design and Applications Branch
1225 West Dayton Street, 2nd Floor
Madison, Wisconsin 53706
(FTS) 364-5325 (608) 264-5325

July 10, 1985

Dr. Bruce R. Barkstrom
ERBE Science Team Leader
Mail Stop 420
Langley Research Center
Hampton, Virginia 23665

Dear Bruce,

I have been looking at the December 28 data from ERBE and have run into some problems that I think you should know about. I have talked to Jim Kibler and Bruce Wielicki about this and they are also interested.

The first problem is seen in the shortwave data on the pass that begins at 185913 GMT on the 28th. Enclosed are some pictures from McIDAS that help to explain the difficulties. Figure 5 is the filtered data, Figure 6 is the top of the atmosphere and Figure 7 is the scene ID. Brightening occurs in the area indicated on Figure 6 that seems to be correlated with an incorrect scene identification in the region marked. Evidently, there is cloudiness at the locations in question, but the scene ID code was for clear skies, which is obviously incorrect.

The second problem on the same set of pictures relates to a clear zone in the middle of the cloudiness near the terminator near the top of the picture. Figure 5 shows it as a bird-shaped area, but the top of the atmosphere shortwave indicates the region has been largely filled-in by the processing procedure.

Perhaps these two problems have been remedied by the changes that have been made in the data processing since the December 28th data tape was made. At your earliest opportunity, I would like to see the revised tape to compare with this first version.

A third problem evident on Figure 9 is banding in the top of the atmosphere longwave values. The radiance data and the unfiltered data also show banding at the same locations. In the top of the atmosphere data, the large changes average 15 watts/m$^{-2}$, but can run larger. It has been suggested by Jim Kibler that the offset which was measured for nighttime values may not be valid for daytime pictures. Also included in this package are means and standard deviations of lines and differences between lines for the unfiltered data, which show the magnitudes involved, and a periodicity that is mostly a multiple of eight.

I hope this is helpful in de-bugging the data. If you'd like more information, please call me.

Sincerely,

Leroy D. Herman

Leroy D. Herman

Enclosure
C2/LDH1/23

TEST 1

DATA: ERBS
TIME: ∿ 0040Z
DATE: November 9, 1984 (second version)
PLACE: 60E, 10N to 30S (start at record 150)
Stradling the terminator with sunshine in Southern Hemisphere.

LW banding in channel 5 (filtered) appears to be present, but to a minor degree. It is more like a blockiness imposed by the resolution limitations. However, the squaring off of the patterns does occur along the scan line. In other words, there is more likelihood of a change in going between scan lines than from pixel to pixel.

Some blooming (brightening) along selected scan lines occurs. The most prominent location for this is centered on the scan line through 12:40S, 70:13E. In the western half of this line there is smearing of the clouds beyond the reasonable limits one would expect. Perhaps something in the system (perhaps noise) is causing this streaking of the clouds. This is in the general vicinity of the terminator, though not precisely on it. However, the final TOA LW values have no major distortions in them beyond those seen in the filtered channel.

A different situation prevails along the southern edge of a clear zone near 5½S, 66E. Here the edge is orientated parallel to the scan lines. Enhancing this scan line parallelism is a sharp drop off in brightness of a cloud in the western portion of the picture, two lines above the clear boundary. This parallelism is picked up in the scene ID as well. The result of this is a banding across the picture in the TOA LW values.

TEST 2

DATA: ERBS
TIME: 0013Z
DATE: November 9, 1984 (second version)
PLACE: 50N Canada-Europe (start at record 50)

Discontinuities show up in the TOA LW values that are not present in the filtered values. Particularly evident ones are on lines centered at: (1) 51N, 12E, (2) 57N, 26W, (3) 53N, 49W.

Causes

In the first case, there is a cloud edge in the western portion of the picture in the filtered data that may have been picked up and spread over the entire line causing the discontinuity.

In the second case, a discontinuity in the scene ID seems to have been picked up and spread over the entire line.

In the third case, some slight amount of cloud edges occur on the same line, but in different parts of the picture. Again, has a small discontinuity been picked up and spread over the whole picture?

For all three cases, the unfiltered picture shows banding in the same location, but it is not quite so continuous a cloud edge as appears in the TOA channel.

SW shows nothing because it is night.

02/LDH1/30

NOV '85

## TEST 3

DATA: ERBS
DATE: November 9, 1984 (second version)
TIME: 002641Z
PLACE: Eastern Europe to Indian Ocean
Discontinuity LW.

Two discontinuities at 23:14N, 48:40E and 17:18N, 52:40E over Saudi Arabia are most prominent in the radiance data than the TOA for unknown reasons. Perhaps because there is no reinforcement by the scene ID to enhance the original lines.

DATE: November 9, 1984 (second version)
TIME: 004001Z
PLACE:

A primary discontinuity in the TOA at 5S, 65:43E has a similar discontinuity in the scene ID, and is suggested in the clouds on the filtered data.

SW has a small band illuminated in the Southern Hemisphere that shows no banding.

## TEST 4

DATA: ERBS
DATE: November 9, 1984 (second version)
TIME: 0053Z
PLACE: 50S, 90E-140E, Southern Indian Ocean

In the area there is virtually no enhancement of banding in either LW or SW. Perhaps this is due to very few of the cloud axis being aligned along the scan lines. The scene ID also has little cloud banding parallel to the scan lines either. As an aside, the scene ID pattern more closely resembles the SW than the LW.

DATE: November 9, 1984
TIME: 0106Z
PLACE: Southern Central Pacific

Some banding occurs on line 225 element 82 in the TOA, and the scene ID. It is at the parallel edge of a cloud.

DATE: November 9, 1984
TIME: 0119Z
PLACE: 0 to 40S, 120 - 160W, Southeastern Pacific

No banding. LW gets darker by processing. SW gets lighter by processing. But this may be an artifact of the numbers not being divisible by 256, which is the maximum possible to display.

DATE: November 9, 1984
TIME: 0133Z
PLACE: Southwestern U.S.
No banding.

## TEST 5

| DATE | TIME | PLACE | COMMENTS: |
|---|---|---|---|
| Nov 9 84 | 0146Z | Great Lakes to Iceland | No banding. |
| Nov 9 84 | 0200Z | England to Mediterranean | No banding. |
| Nov 9 84 | 0213Z | Eastern Africa at 10:45S, 44:30E | Slight banding in TOA and scene ID. |
| Nov 9 84 | 0226Z | Western Indian Ocean at 48:08S, 82:00E | |

(A) Three line drop-outs in both TOA LW and scene ID. (B) In SW at the same location a cloud shadow through the same cloud shows up best in the TOA SW. (C) However, to the south the brightest band, which has an irregular darkened portion along its axis in the raw data, becomes uniformly bright in the TOA! Looks strange to brighten it so much. (That was a wrong appearance in the visible. When a different division is used to spread the brightness range (24 instead of 20 on TOA SW) the raw and TOA values in that region are nearly identical brightnesses and patterns.)

## TEST 6

DATA: ERBS
TIME: 1616Z
DATE: November 30, 1984
PLACE: 40-50S

Several areas of interest:
(1) Short segments of scan lines from 40 to 50S are seen in the western portion of the picture in all versions of both LW and SW data.
(2) The banding changes its nature in the bottom one-fourth of the picture which is especially evident in the partly cloudy region.
(3) Band brightening is visible near 145W.
(4) A partial line dropout occurs near 157W.

**UNITED STATES DEPARTMENT OF COMMERCE**
**National Oceanic and Atmospheric Administration**
NATIONAL ENVIRONMENTAL SATELLITE, DATA, AND INFORMATION SERVICE
Washington, D.C. 20233
Systems Design and Applications Branch
1225 West Dayton Street, 2nd Floor
Madison, Wisconsin 53706
(608)264-5325 (FTS)364-5325

December 13, 1985

Dr. Bruce Barkstrom
ERBE Science Team Leader
Mail Stop 420
Langley Research Center
Hampton, Virginia 23665

Dear Bruce,

Enclosed is a copy of the reports that I would like to see in the Minutes of the Science Team Meeting held at Goddard last week. It was a good meeting and there seemed to be a general mood of optimism prevailing.

The first report included on scanner noise requires one additional remark. Besides the banding or striping that has been demonstrated in the scanner pictures, there is at least one other set of noise. Beginning in the lower left portion of figure 4B, there are darkened regions of four lines duration about five pixels long that runs up the left. I have now seen more pictures from this pass and see these darkened regions alternating their position passing through the central axis south to north of the next frame (picture enclosed). On the next frame after this one, this checkerboard pattern runs up the right side and exits there. Very unusual.

We are looking forward to receiving the February 7 tape for comparison with VAS.

Sincerely,

Leroy Herman

Leroy Herman

Enclosures

02/LDH2/06

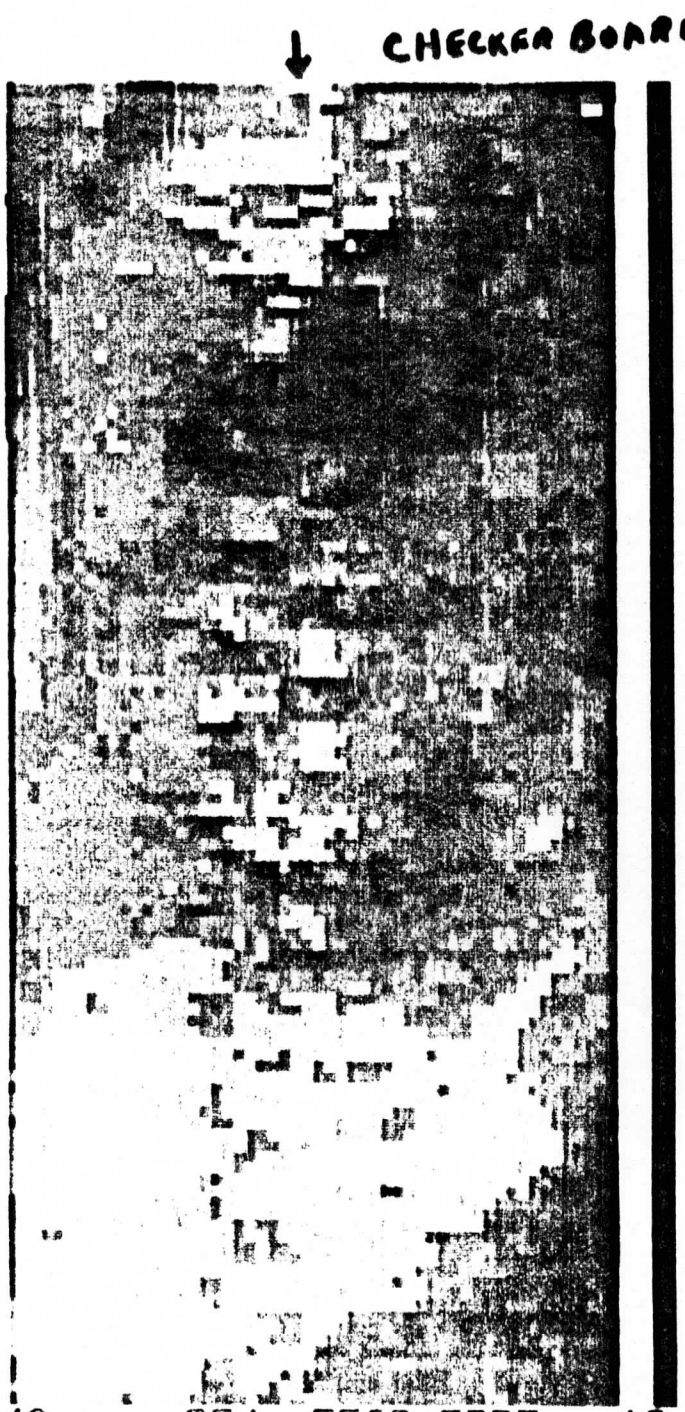
CHECKER BOARD AXIS
13 054 5560 ERBE 12 84335 162936 00002 00002 00.25
LW TOA

17th ERBE Science Team Meeting

Goddard Space Flight Center

December 3-4, 1985

Cooperative Institute for Meteorological Satellite Studies
NESDIS - University of Wisconsin

Reports

1. A Search for ERBS Scanner Noise...Leroy Herman

2. A Preliminary Comparison Between Scanner and Non-scanner Data... Leroy Herman and Xiangqian Wu.

3. A Quick View of ERBS Scan and Non-scan Data... Fred Nagle

# A Search for ERBS Scanner Noise

Leroy Herman
NOAA/NESDIS
University of Wisconsin

November 29, 1985

A small sample of the ERBS scanner data from the first month's tapes was examined visually for recognizable patterns. Generally, pictorial presentation of the data can be recognizable to the meteorologist because of the similarities between the ERBS short wave and long wave with other satellites visible and infrared channels, respectively. Most patterns will appear the same from one satellite to the other. However, examination of the ERBS data shows patterns which are unexpected and therefore suspect. A pattern which appears in the data that arouses considerable interest is straight lines.

Although meteorological patterns can have straight line edges, only those lines that happen to fall parallel to scan lines are in question here. Many examples have been found; some of them are natural edges occurring fortuitously along a scan line, but most appear to be artificial enhancements whose sources have not been determined but probably are caused by noise.

A search was made of the first orbit and a half of the second version of the November 9, 1984 PAT tape to detect discontinuities. There were 50 records at a time examined by displaying them on the McIDAS. About half of these pictures had significant discontinuities. The primary discontinuity found repeatedly is a banding, usually composed of eight brightened scan lines usually seen in the top of the atmosphere (TOA) and unfiltered values in the long wave pictures. Sometimes parts of the discontinuity could be seen in the filtered LW and scene ID, too.

A typical example is shown in Figure 1 which covers the region from Canada to Europe around 50°N. The TOA values in the LW show three discontinuities in the 0013GMT normal size pictures as marked.

Figure 2 shows the November 9 0032GMT picture over Saudi Arabia. The primary discontinuity occurs across central Saudi Arabia, but appears to be related to a plateau edge oriented parallel to the scan lines. The short wave image at night illustrates the "ring worm" problem.

Figure 3 comes from the first version of the December 28 PAT tape. It shows brightening occurring in the short wave TOA picture in the two cloud lines near 40N, 130W. These appear to be caused by the scene ID incorrectly calling these areas clear skies. This problem of misidentification is expected to be corrected in the second version of this tape. In addition, some banding is seen in the LW TOA picture.

Figure 4 is an example from the second version of the PAT on November 30. The area shown is in the southeastern Pacific. The LW TOA values have two superimposed patterns up the left side of the picture. The darker one is a repeating four line pattern of alternating values in the 260's, then 250's $w/m^2$. First one then the other. A second pattern superimposed on the first is a three line pattern of 220's, 250's, and 220's again. This is more irregular, and is on a background mostly in the 250's. In addition, a partial line of missing data in LW, SW, and scene ID is centered at 53S, 159W.


[illegible] IN TOA AND BLOWUP OF SCENE ID.

FIGURE 11. NOV 8 1973 SMT BLOWUP OF LW TOA, FILTERED AND UNFILTERED.

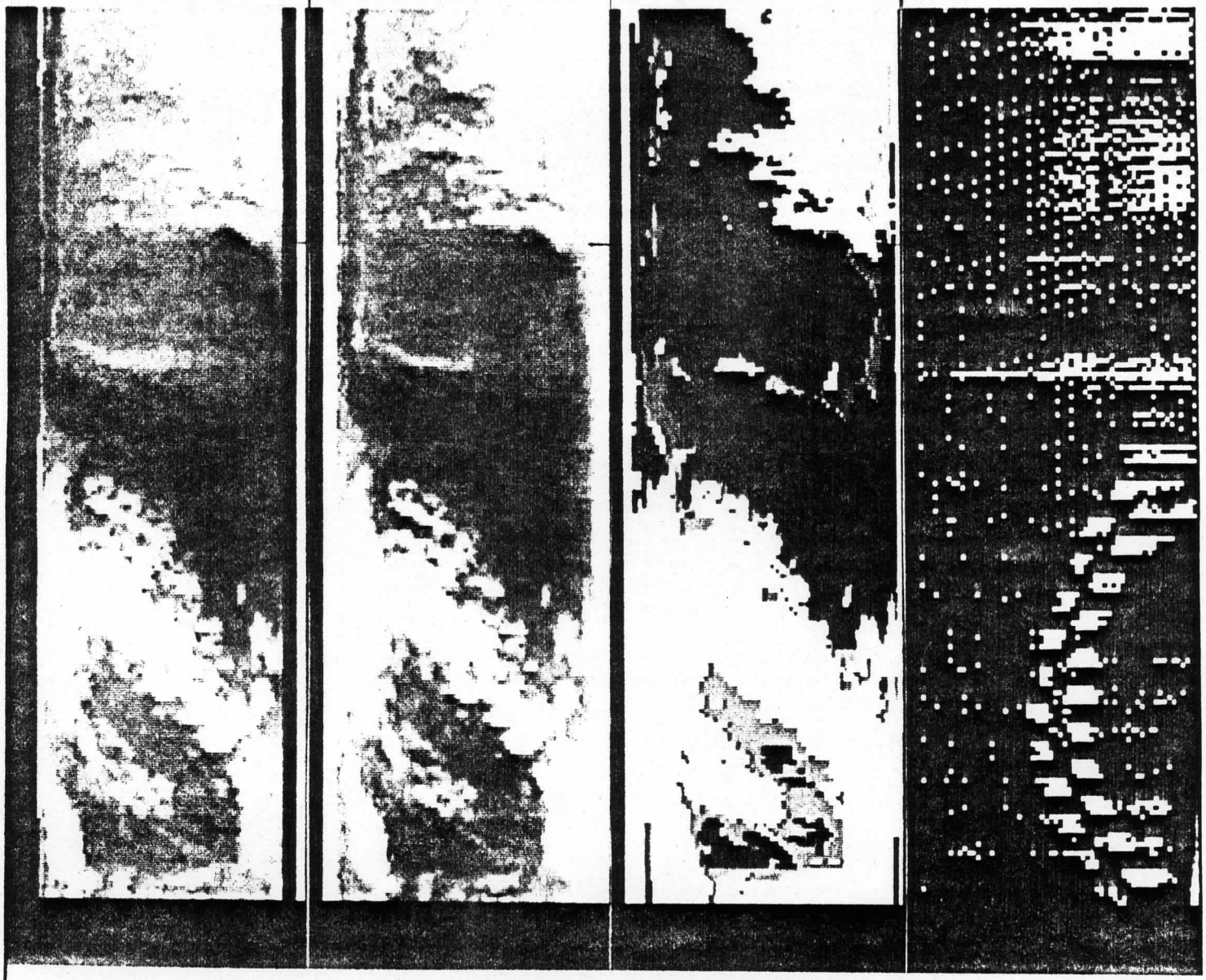

[illegible] SAUDI ARABIA CASE. LW TOA, FILTERED. [illegible]

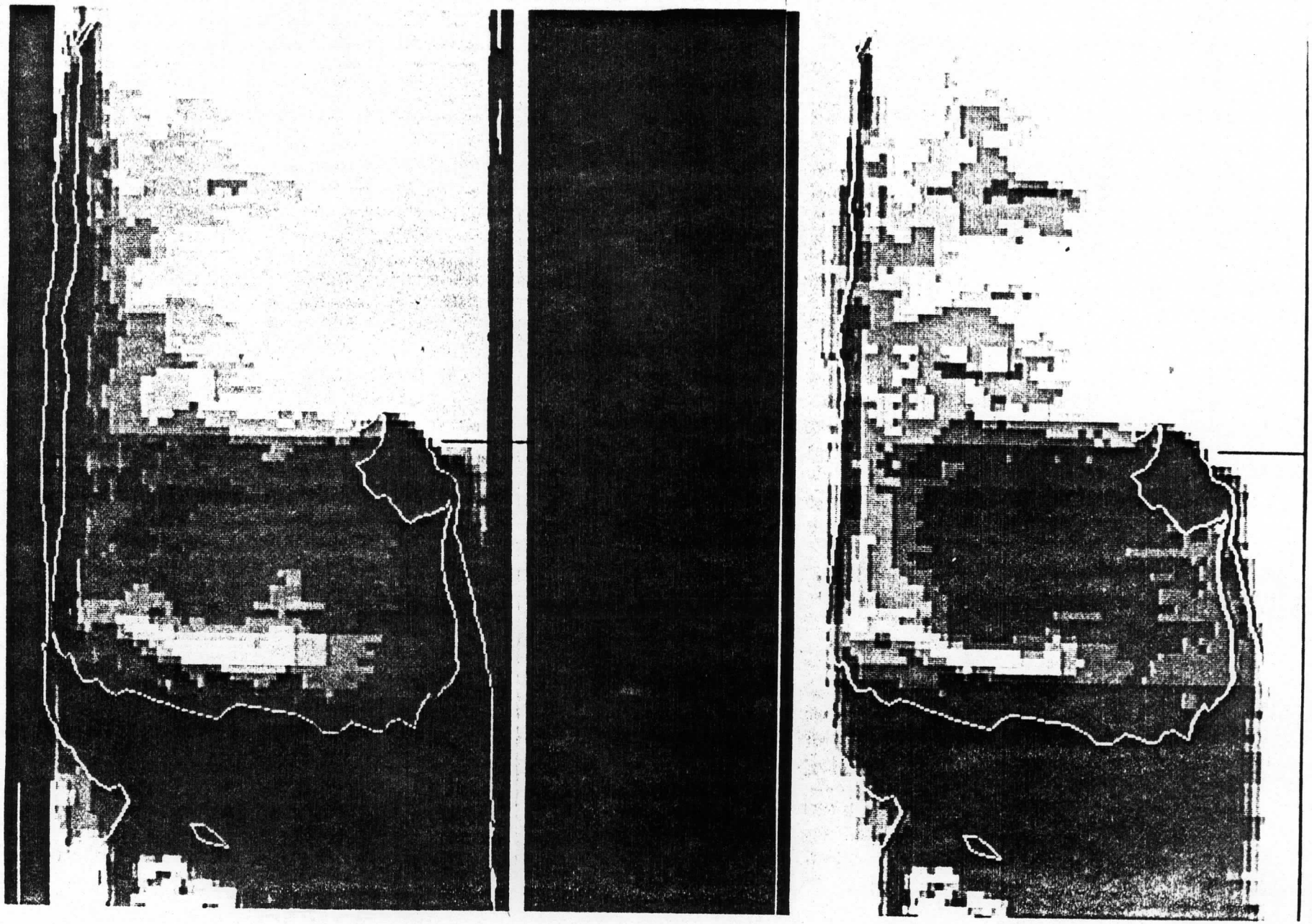

[illegible] LOWUP OF LW TOA AND FILTERED.

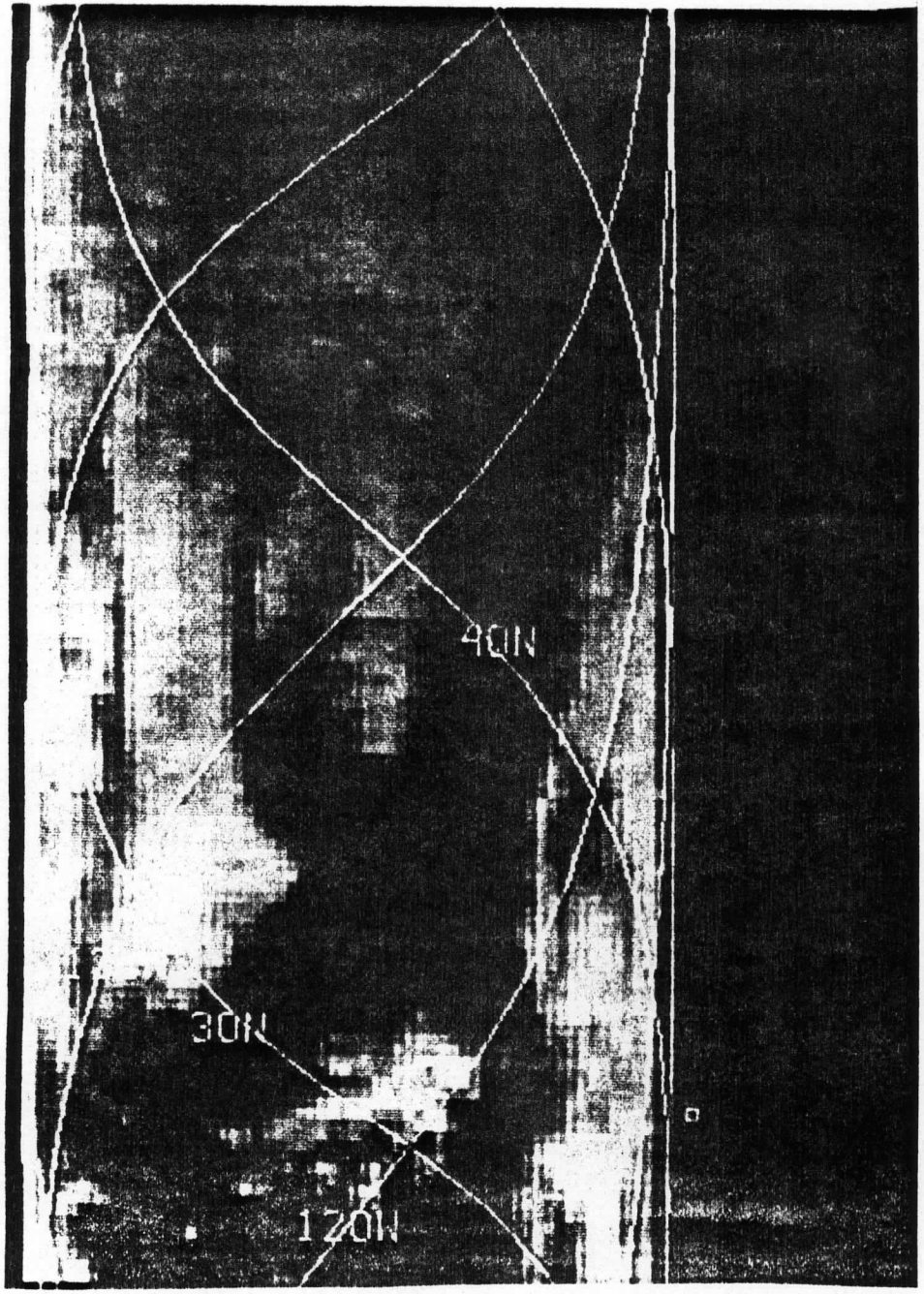


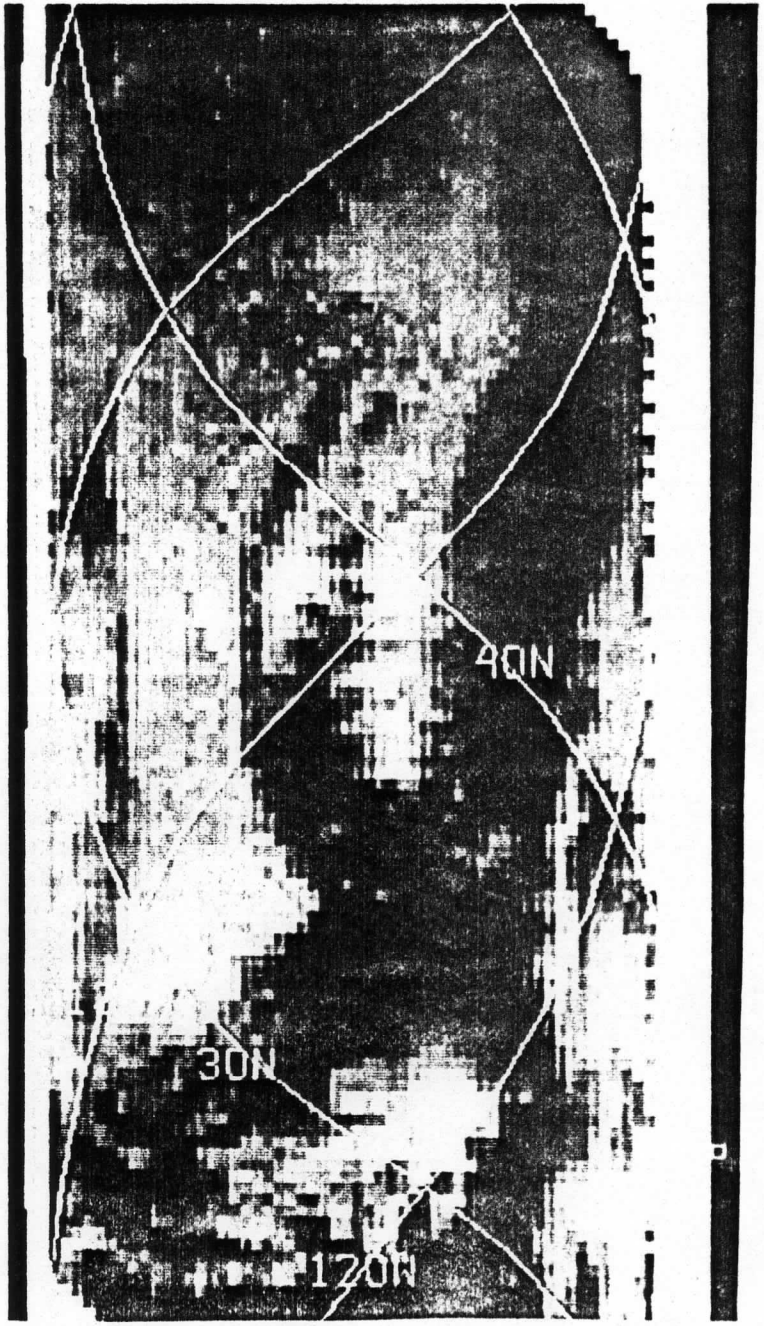


[illegible] SEP. 9 1979 PORT SW FILTERED AND TOA.

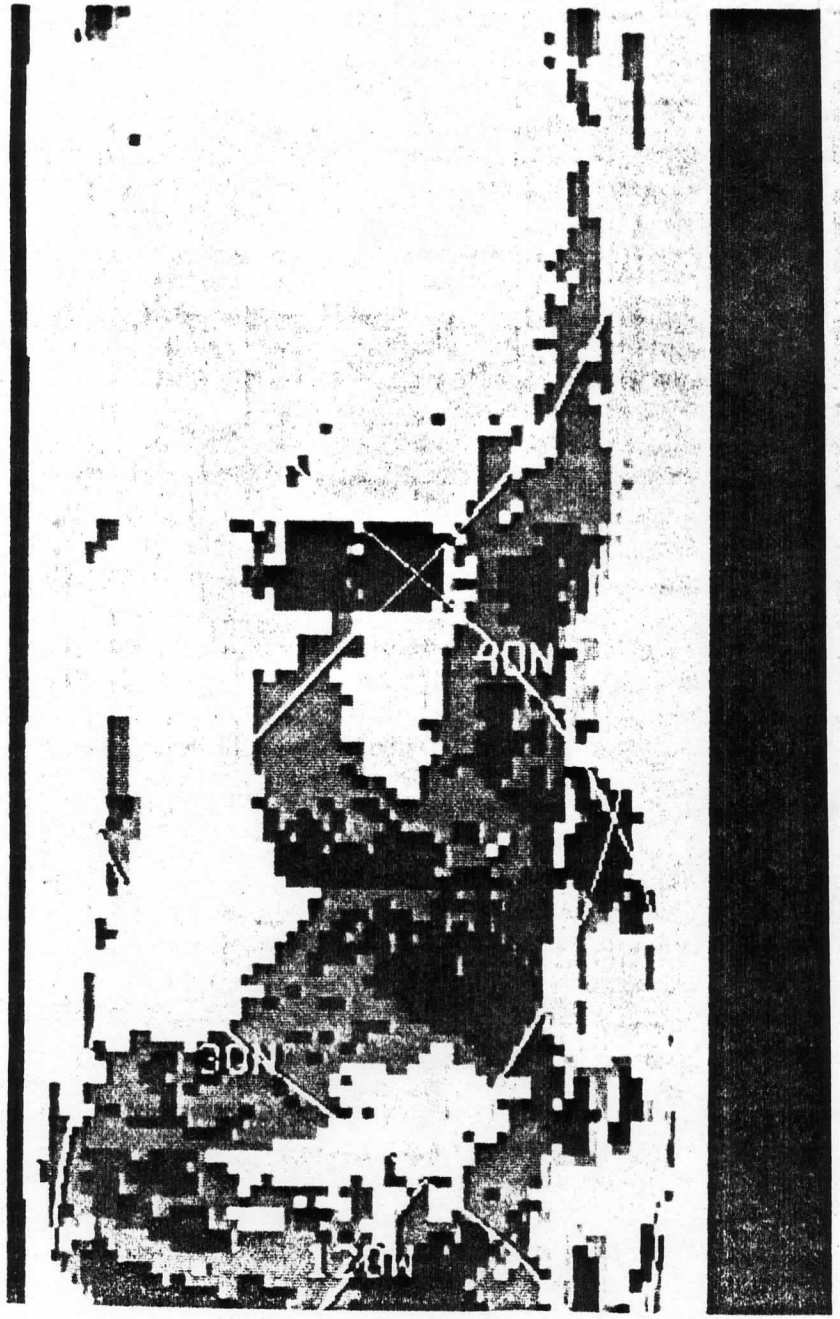


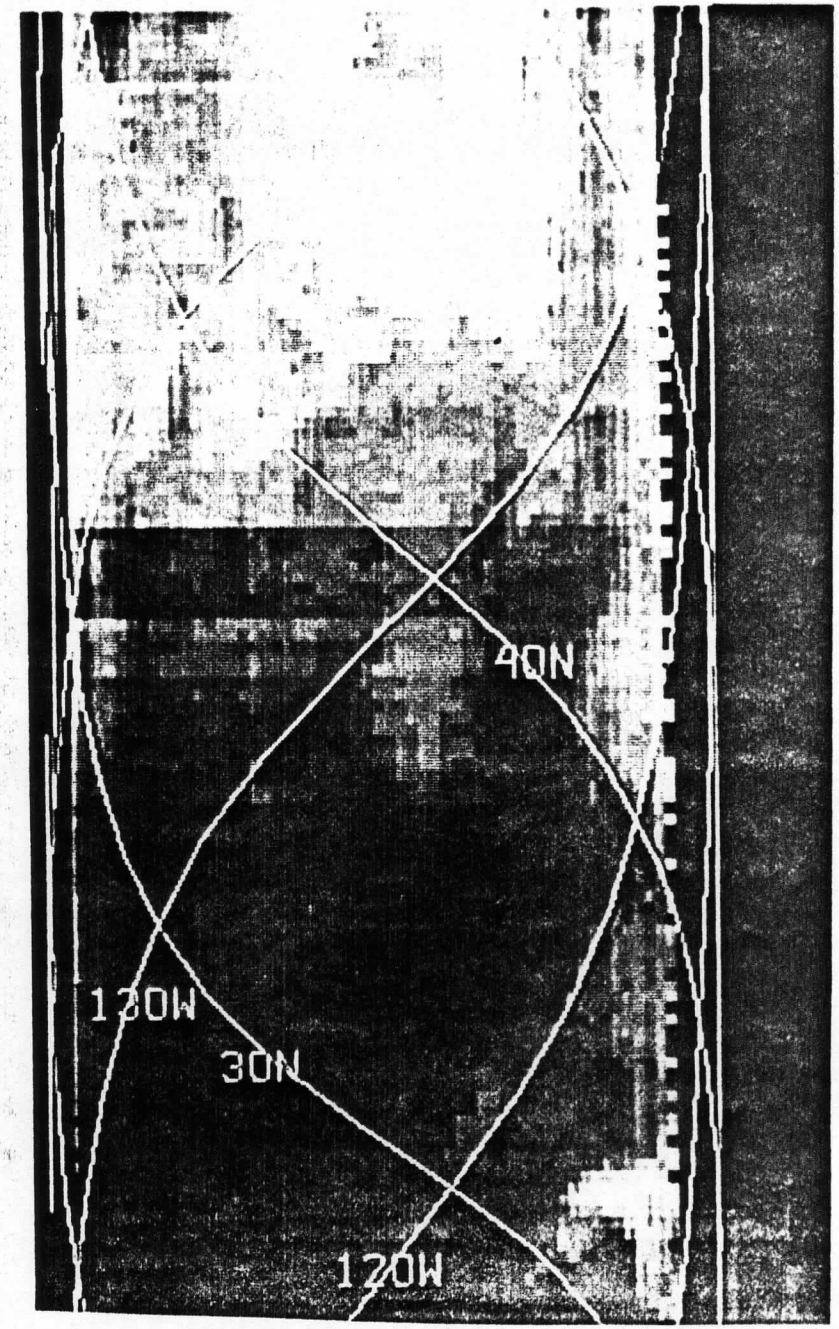


[illegible]. [illegible] AND LW TOA.

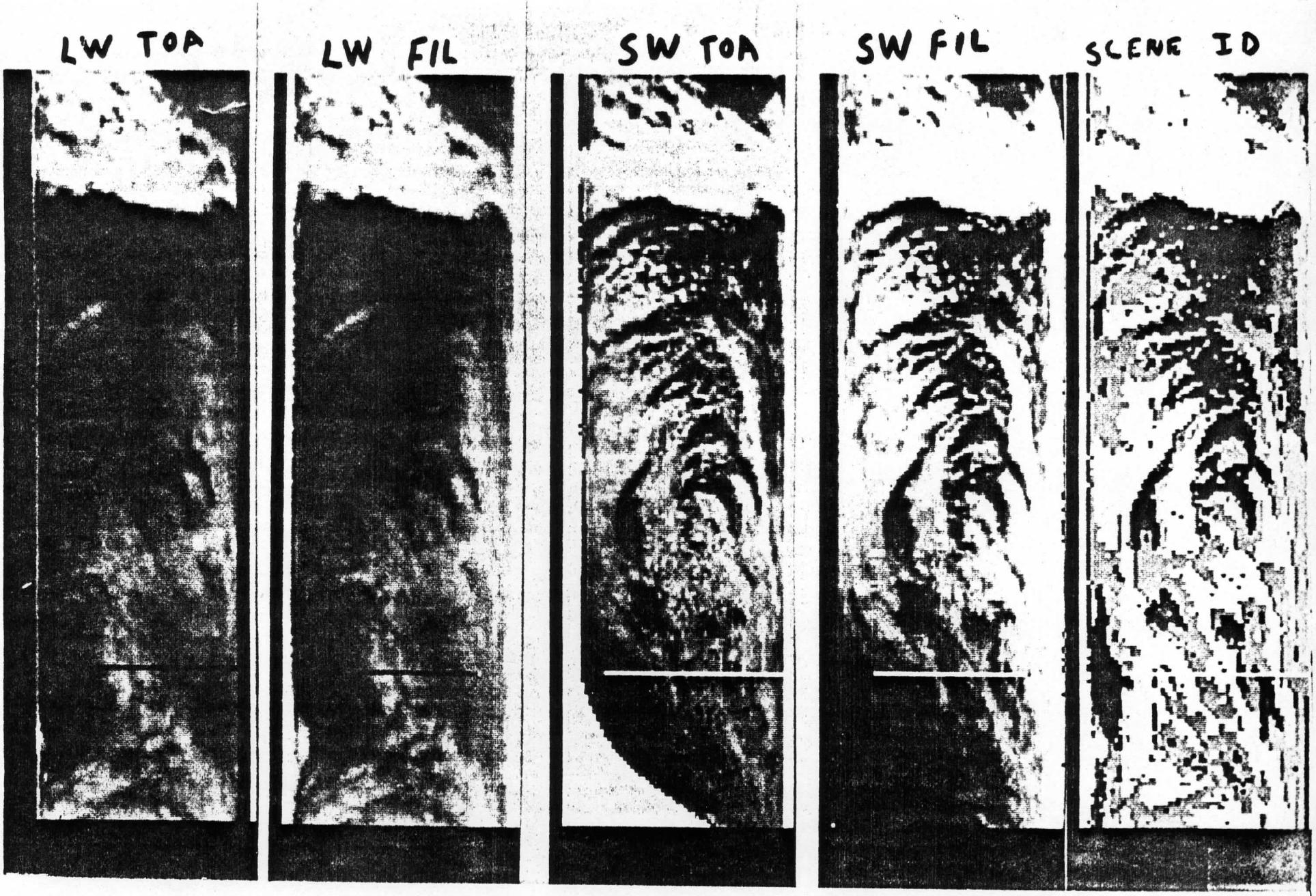


FIGURE 4A. NOV 30 1616GMT LW TOA, LW FILTERED, SW TOA, SW FILTERED AND SCENE ID.

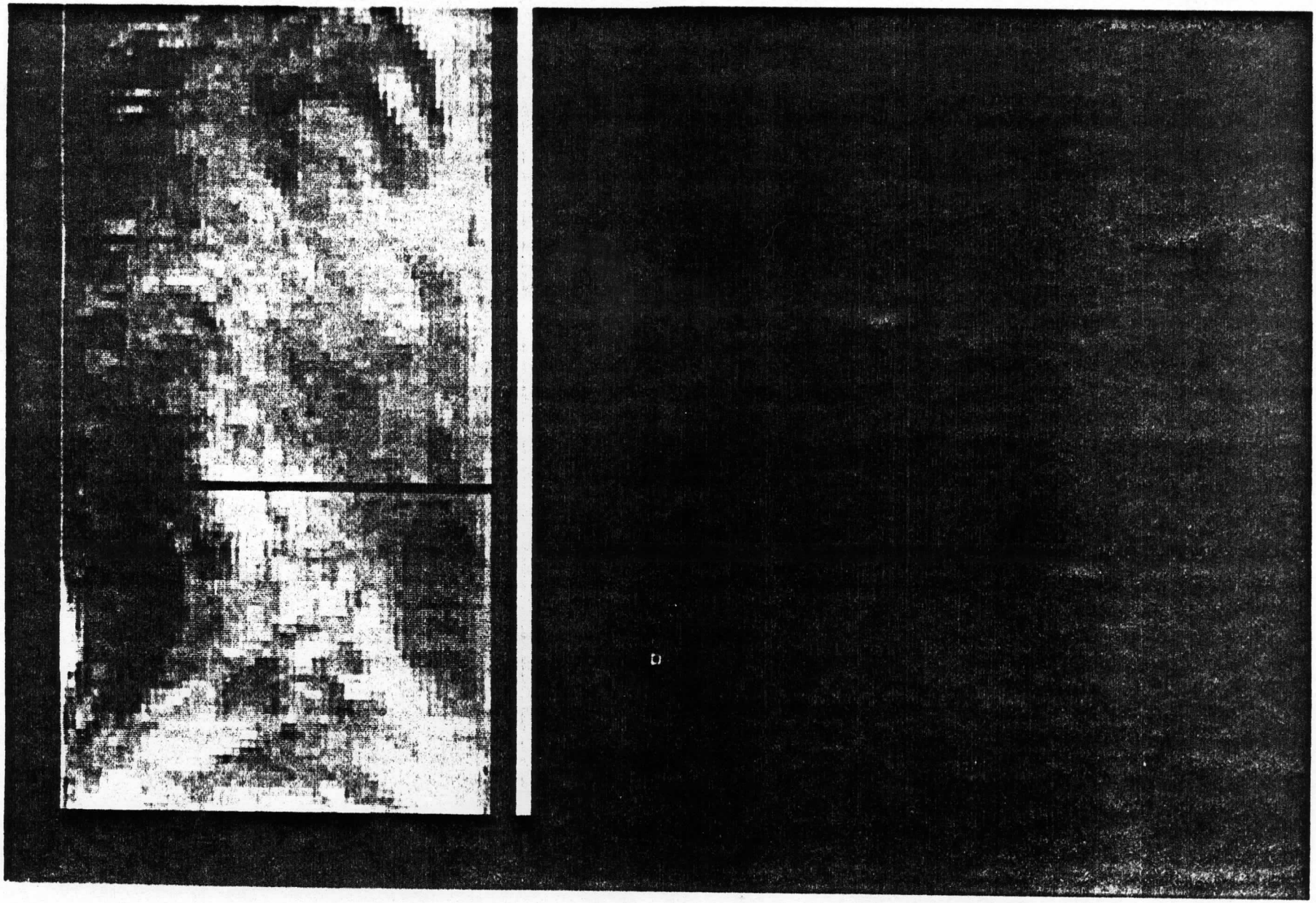

FIGURE 4P. NOV 30 1616GMT SW IOA.

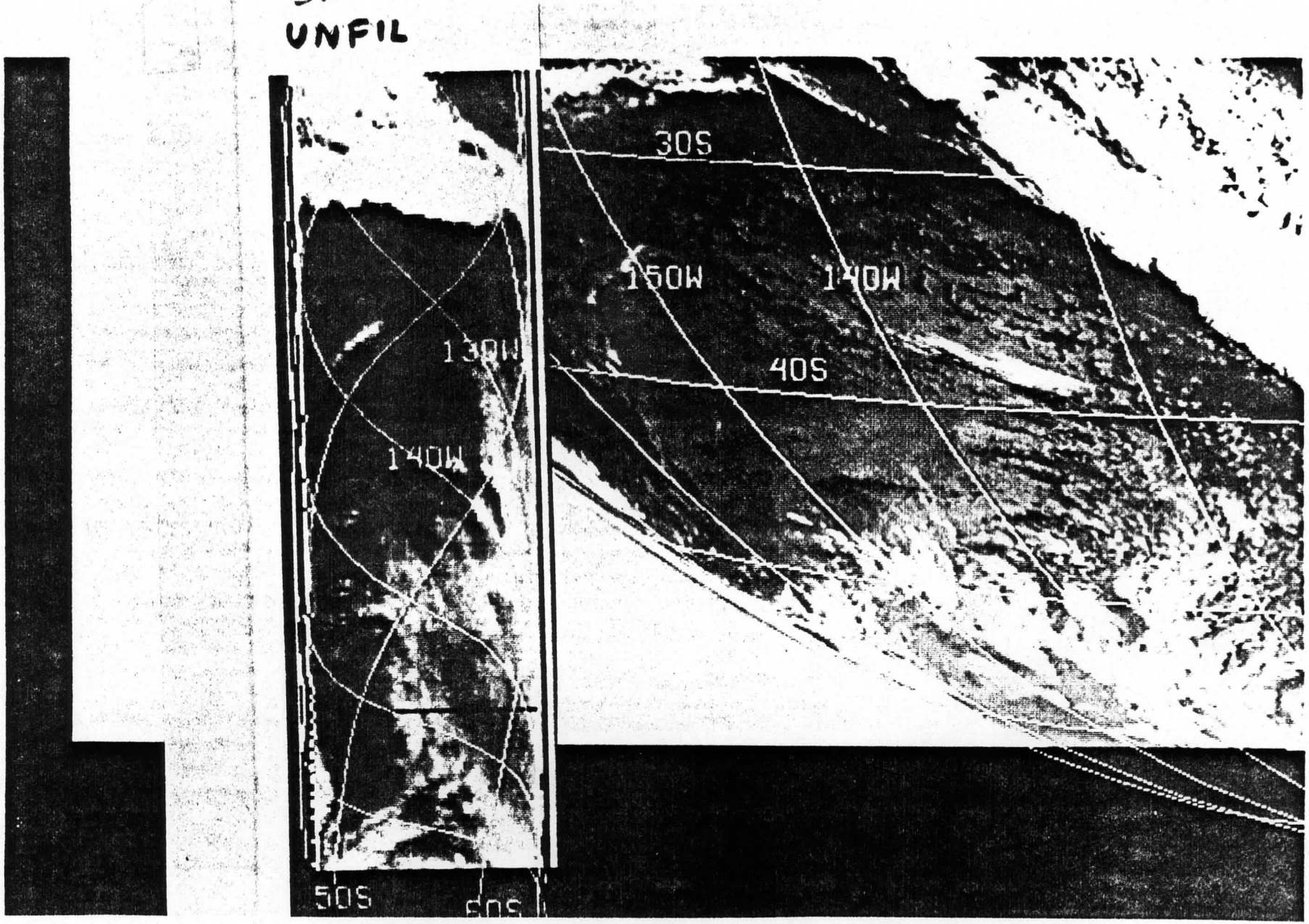


FIGURE 4C. NOV 3 1616GMT GOES-6 IR WITH ERBS 1616GMT LW UNFILTERED INSERT.

# A Preliminary Comparison Between Scanner and Non-Scanner Data

by Leroy Herman and Xiangqian Wu

Data for November 9, 1984 ERBS were selected for comparison between the scanner and non-scanner. The area considered was on the first orbit in the Eastern Pacific Ocean dry zone where there is a minimum of cloudiness. In order to make a comparison, the scanner data was integrated over the viewing area of the non-scanner instruments.

In Figure 1 a satellite orbit is shown, with the satellite's position at times $T_0$ and $T_1$. The ground track and the two horizons seen by the instruments during the orbit are shown. At time $T_1$ the WFOV non-scanner has a footprint shown as an elipse. At the earlier time $T_0$, the satellite scanner was just beginning to observe the WFOV footprint. For a particular satellite instrument, say the short-wave scanner, the bi-directional model is used to convert the reading to an anisotropic value representing the contribution of that point to the reading by the non-scanner for the geometry at the later time $T_1$. All of the other points observed by the short-wave scanner within the footprint are similarly processed so that an integrated value over a period of time from the scanner data is obtained. Similarly, integrated long-wave and total channel data was obtained.

Results of the computations and comparisons are shown in the table. For each non-scanner instrument observations are made every .8 of a second. Data at this high frequency of observation is noisy as seen by its consistently higher standard deviation. In addition, in every case the correlation of the high frequency data with the integrated scanner data is worse than the averaged data correlations. It seems strange that averaged data compares so much better because for this data sample the region is mostly clear of clouds. Thus, the high frequency data is believed to be considerably less reliable than the averaged data.

Non-scanner observations are only made in the short-wave and total bands, while the long-wave values are derived from them. For this data set, the long-wave band has the smallest mean deviation.

02/LDH1/32

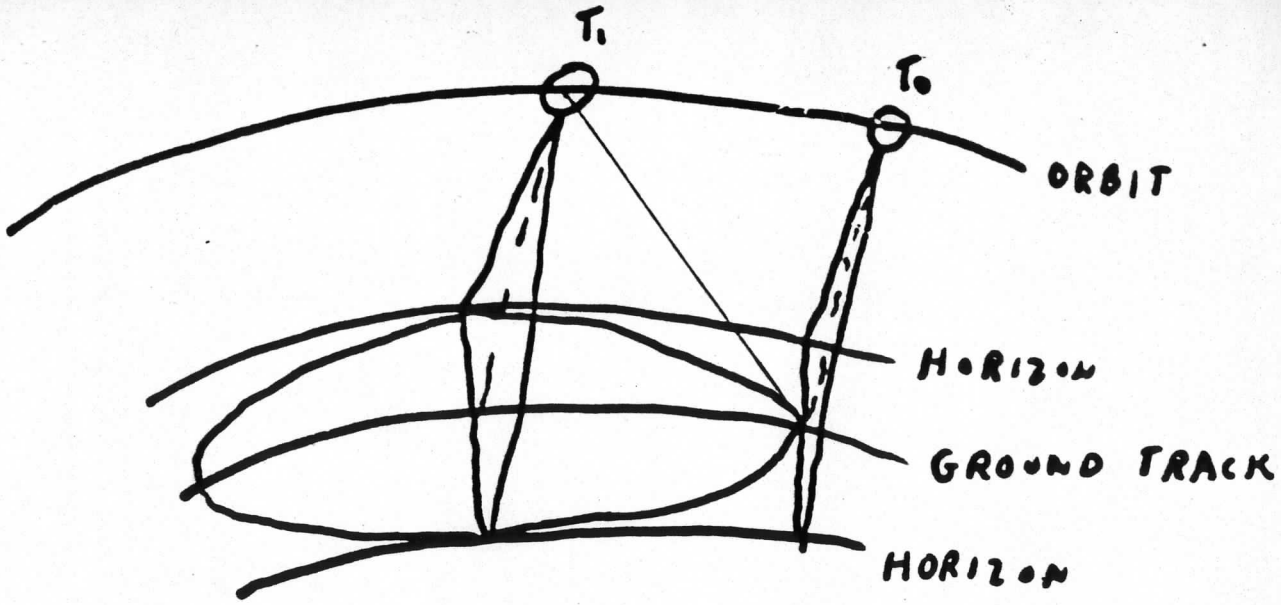


SATELLITE-EARTH GEOMETRY

FIGURE 1. SCANNER AND NON-SCANNER FOOTPRINTS ON EARTH.

Scanner vs. Non-Scanner

| | Non-Scanner | Mean | S.D. | R | Scanner Mean | Scanner S.D. |
|---|---|---|---|---|---|---|
| TOTAL | WFOV | 315.8 | 2.15 | .87 | 308.9 | 2.72 |
| | AVG | 315.8 | 1.92 | .99 | | |
| | MFOV | 152.5 | 1.24 | .90 | 149.2 | 1.13 |
| | AVG | 152.5 | 1.16 | .97 | | |
| SW | WFOV | 65.2 | 1.79 | .97 | 60.4 | 2.64 |
| | AVG | 65.2 | 1.77 | .98 | | |
| | MFOV | 22.7 | 1.78 | .41 | 18.6 | .41 |
| | AVG | 22.7 | .94 | .81 | | |
| LW | WFOV | 250.5 | 1.10 | .41 | 248.5 | .32 |
| | AVG | 250.5 | .51 | .92 | | |
| | MFOV | 129.7 | 1.66 | .27 | 130.6 | .30 |
| | AVG | 129.7 | .71 | .59 | | |

# A QUICK VIEW OF ERB-s SCAN AND NON_SCAN DATA:

By: Fred Nagle

In an effort to gain familiarity with the ERB PAT data, several programs were written at SDAB/NESDIS/NOAA, Madison, to obtain a quick view of the data from both the scanner and medium field of view detectors. Only the long-wave data were processed. Some results follow.

## MEDIUM FIELD OF VIEW:

One entire PAT (Processed Archival Tape) was used for 9 Nov 84. The program was run on an IBM 4381 at the Space Science and Enginnering Center, University of Wisconsin - the so-called McIdas system.

The data obtained from the PAT were plotted onto a Mercator projection of the Earth extending west to east from longitude 180 W to 180 E, and from north to south from latitude 80 N to 80 S. A grid was superimposed over this Mercator projection consisting of 100 points in the east/west direction, and 80 north and south. Such a grid has a resolution of roughly 3.6 degrees east and west. The grid resolution north and south varies with latitude, and is uniform in meridional parts on a Mercator projection, but not on the Earth.

Each PAT record contains 20 medium field of view (MFV) readings, separated by intervals of .8 seconds. To reduce the computational burden on the computer, only two of these 20 readings were used. The MFV detector observes a subset of the Earth's surface subtending an angle of 10 degrees at the center of the Earth. To each grid point falling within the MFV at the moment of a given observation, the program assigned the value of the current longwave reading, weighted and reduced by the cosine of the nadir angle to allow for the flat plate response of the MFV detector. These weighted observations were summed at every grid point over the period of a day, as well as the weights themselves. The weighted observations were then divided by the summed weights at the end of the period to obtain normalized values at all grid points. In extreme polar latitudes, and in some tropical latitudes where successive satellite orbits are widely spaced longitudinally, there were no observations at any time during the period of one day. A linearly-interpolating filling procedure was used to fill in the unobserved tropical nodes, and a constant-value extrapolation was used in polar regions to obtain a value at all 8000 grid nodes.

The results of this procedure are shown in Fig. 1. No conventional data or visible satellite images are available, so comparisons of Fig. 1 with weather phenomena are only conjectural at this point. The region of low readings extending across the tropical Atlantic is presumably the Inter-tropical convergence zone (ITCZ). The

ITCZ, if that is what it is, appears much less strongly in the same latitudes of the Pacific. The highest readings appeared in the tropical Pacific, with values in excess of 125. Aside from the ITCZ, the lowest values appear over central Siberia. The units shown on this chart are simply the values taken directly from the PAT, with no regard to their calibration. The grid shown are those for which at least one reading was available at some time during the day. Note that there are no observations off the southwest coast of Mexico.

SCANNER DATA:

(In the following, reference is made to the celestial and terrestrial coordinate systems. Both use the center of the Earth as origin. In the former, the x-axis lies in the plane of the equator directed toward the Vernal Equinox; the z-axis points toward the North Pole, and the y-axis is chosen to complete a dextral orthonormal system. The terrestrial system has the same z-axis. The x-axis is directed toward the Greenwich meridian, and the y-axis points 90 degrees east of Greenwich to constitute a dextral system. The two coordinate systems are in constant rotation relative to one another at a rate of 360.9856473 degrees per day.)

It goes without saying that in processing a single day of scanner data, one may encounter widely fluctuating results, owing to the fact that a given scene, viewed at several different moments of the day, may undergo a great change in its radiating properties from one observation to the next. Accordingly, it is difficult to ascribe a clear meaning to the results shown in Fig. 2.

In processing the scanner data, some effort was made to estimate the tilt and wobble of the ERB-s satellite in its flight. It was assumed that both the satellite position vector, given in the PAT record, as well as the ground latitude/longitude of each of the 62 scan points in a given scanner sweep, were correct. The program then used the Earth-located position of scan points 31 and 32, which lie nearest the center of a sweep, to estimate any bias in the location of all 62 scan points.

First, a dextral orthonormal coordinate system was defined fixed to the satellite at every instant, with the x-axis along the direction of flight, the y-axis to the right of the flight path, and the z-axis directed downward toward the center of the Earth. This is the so-called 'climbing right turn' convention. Since the satellite's position was given at every moment, the negative unit vector of its terrestrial position was taken as the z-axis. The vector cross product of the satellite's position vectors 5 minutes before and 5 minutes after each scan was computed and was then used as the vector orbital plane (VOP). The cross-product of VOP with the satellite's instantaneous position vector then defines the

x-axis, and the y-axis is then the cross product of the unit-z and unit-x vectors. These calculations are conveniently expressed by the vector equations:

```
VSK = -VUNIT4(VSAT)
dtime = dtime + dsec
VSI = VSK ** VCOORD( dtime, VOP, 'CT  ')
VSJ = VSK ** VSI
```

Note that the program was written in Meteorological Fortran (Metefor) which allows vector and matrix expressions to appear directly in the source code, so that these equations not only describe the transformation from terrestrial coordinates to satellite coordinates, but are also the actual Fortran code used in the program. VCOORD is a vector-valued function which converts a vector from celestial coordinates (in which VOP was initially computed) to terrestrial coordinates at a given instant. The double asterisk (**) is the vector (cross) product operator.

If VMEAN is the mean earth position of scan points 31 and 32, then the vector discrepancy VDISCR given by

```
VDISCR = VMEAN + 6371.*VSK
```

is the difference between the sub-satellite point and the geometrical center of the scan. (VMEAN points from the center of the earth upward to the geometric mean center-of-scan, and VSK points downward from the satellite, so the two vectors have opposite sense.) The two scalar-products

```
compI = VSI*VDISCR
compJ = VSJ*VDISCR
```

are then the along-track and cross-track components of this discrepancy, respectively. The values, summed and averaged over the entire day, were -0.16 km along-track, with standard deviation of 1.35 km, and -21.54 km mean and 4.04 km standard deviation cross-track. The values -0.16 and -21.54 represent a bias or constant tilt in the satellites attitude, and the standard deviations represent the 'wobble' or changes in the attitude. The magnitude of the maximum vector discrepancy observed during the day was 29.24 km, about 2-sigma values from the mean.

Radiometric Data:

The two end points from each 62-point scan line were discarded because they lie very close to the limb of the Earth. The remaining 58 values from each scan were then processed and plotted on a Mercator projection and grid such as described above.

84 11 8

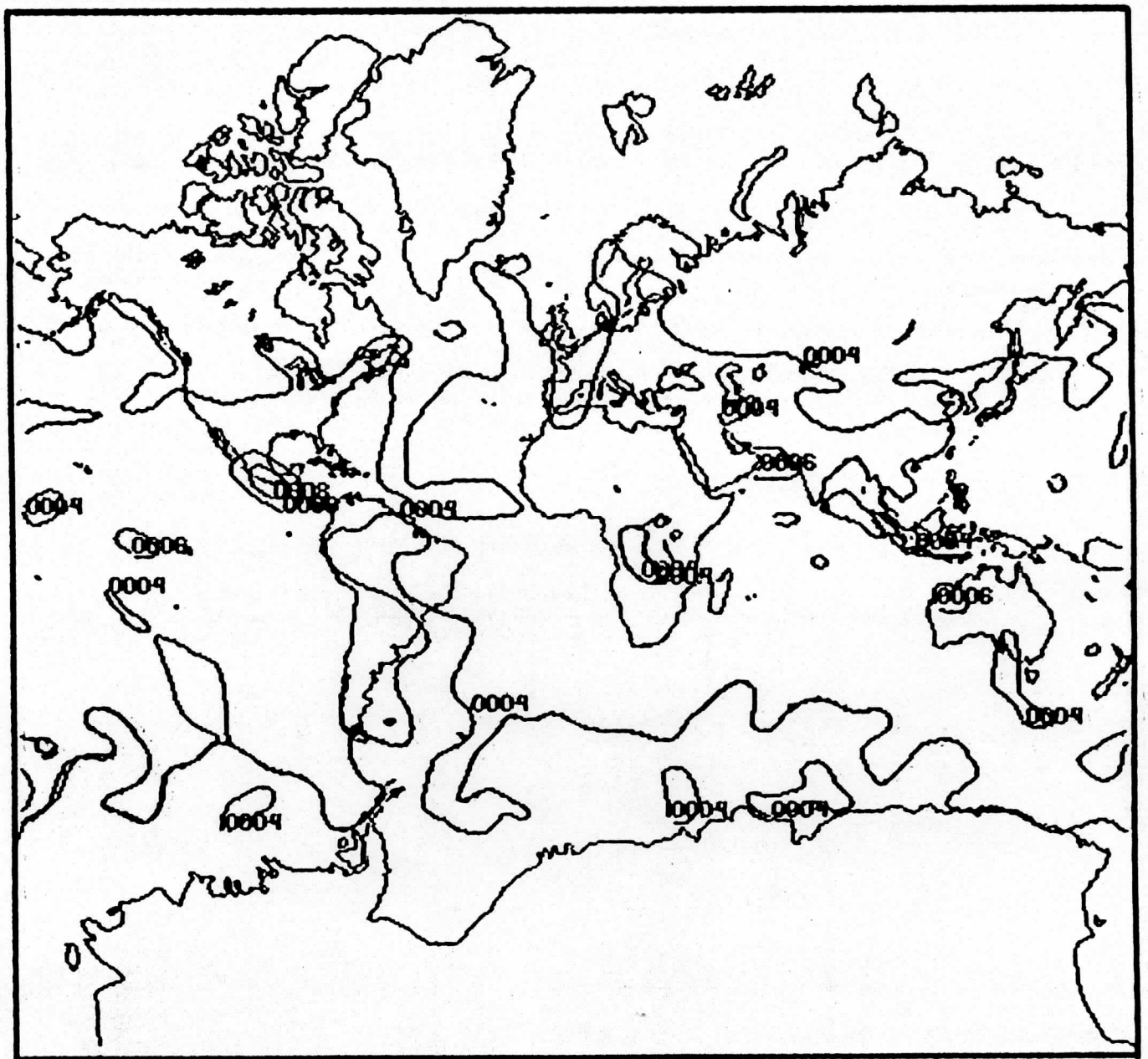

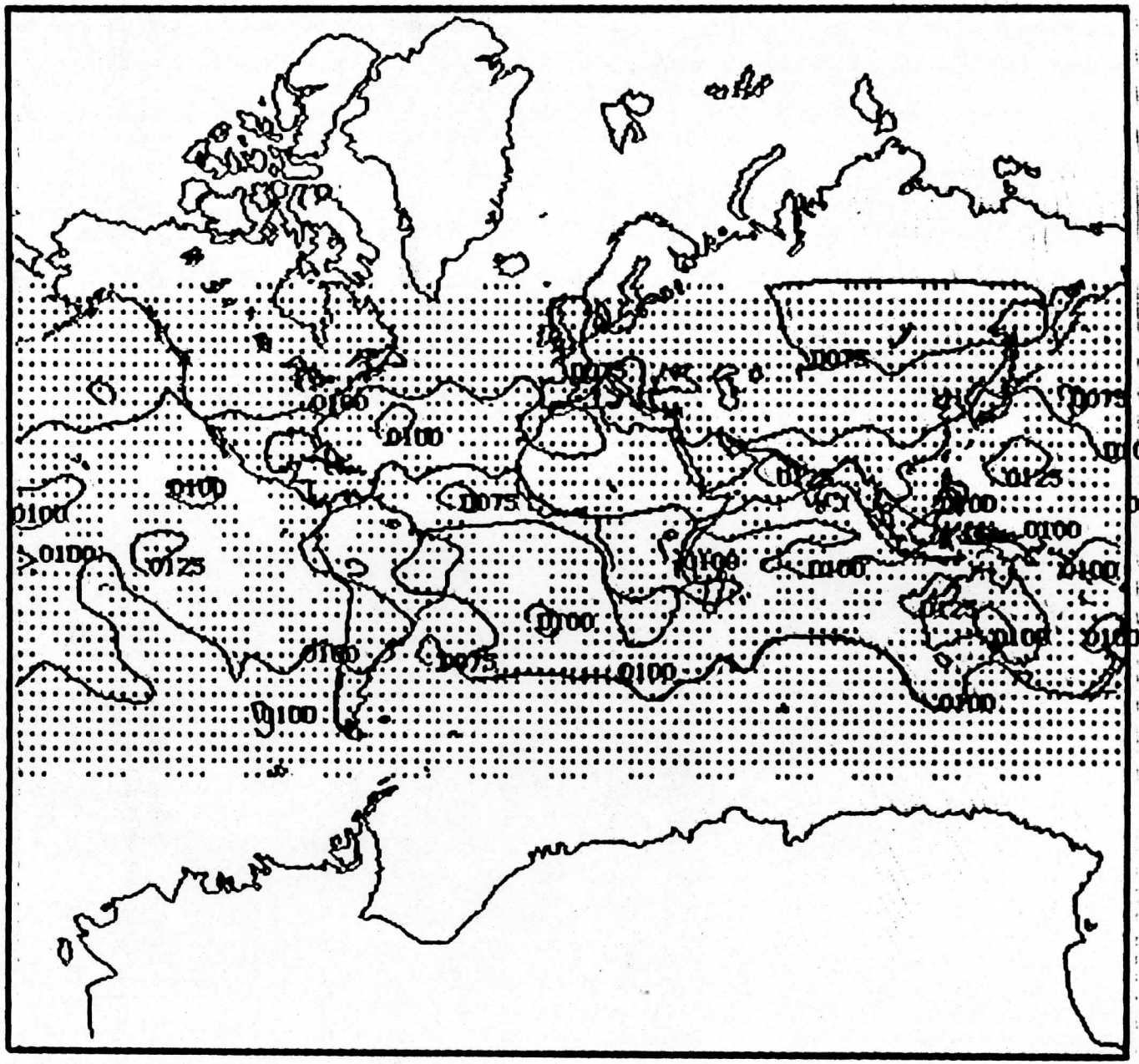


2

4/22/86

Removal of Striping from ERBE Data

Much of the ERBS data that is the Top of the Atmosphere (TOA), long wave variety contains striping or banding. The stripes are eight scan lines wide at least, but may be wider. It is clear that this is an erroneous signal that should be purged from the data. If its source were known, it could be removed. However, the cause is uncertain, though the space clamp is a very likely source. It is unfortunate that the capability to calibrate the data appears to be the source of erroneous data. In addition, a contributing factor to the problem may also be the methods of processing the data on the ground. This is possible because the raw long wave data does not usually have the same striping as the finished product, top of the atmosphere data. Thus, there could be more than one source of the striping.

The correction of the TOA to remove the striping has been attempted with the following considerations. When the striping begins, it appears as an offset to all of the values in a scan line and the next seven lines as well. This creates a brighter or darker band that can either be subtle or obvious depending on the amount of the offset. A measurement of the size of the offset can be made by subtracting the average TOA's for successive lines. The striping begins to become evident in the pictures when it reaches 3 $W/m^2$. However, when there is a natural gradient in the cloudiness due to a cloud edge falling parallel to the scan lines, much larger changes in the scan line averages are possible which are true data variations. On those occasions when a natural cloud gradient occurs when an eight line offset is expected it becomes difficult, if not impossible, to determine the magnitudes of the two effects precisely. In regions where there are uniform conditions being observed, such as clear skies over the ocean, the gradients can be small enough to allow a good estimate of the magnitude of the offset to be made.

EXPERIMENTS

One approach used was to remove all of the variation that occurred at the eight line interval. This caused a deficit of about 33 $W/m^2$ by the time the end of the 200 scan line picture was reached. A second try apportioned the deficit over the picture at the eight line interval--an unsatisfactory procedure.

Another approach tried was to arbitrarily reject every eight line change and reassign the average value of the two lines forming the offset to the mid-point between them. Then the slopes between the midpoints of the offsets were used with the slopes of each eight line range to proportionally compute modifications to each scan line. This method produced changes in the values of each scan line (though many were very small). However, natural changes at cloud edges were modified as well, unfortunately.

Reprinted from Preprint Volume, Sixth Conference on Atmospheric Radiation, May 13-16, 1986, Williamsburg, Va. Published by the American Meteorological Society, Boston, Mass.

J1.15

# INTERCOMPARISON OF PRELIMINARY EARTH RADIATION BUDGET SATELLITE (ERBS) FLUX ESTIMATES AND GEOSTATIONARY SATELLITE MULTI-SPECTRAL "VAS" RADIANCE MEASUREMENTS

Leroy D. Herman[1] and William L. Smith[2]

[1] National Oceanic and Atmospheric Administration
Systems Design and Applications Branch

[2] Cooperative Institute for Meteorological Satellite Studies
Space Science and Engineering Center
Madison, Wisconsin

## 1. INTRODUCTION

The Earth Radiation Budget Satellite (ERBS) provides radiation observations from the earth and its atmosphere. The observations are for two broad spectral bands, a long-wave band of 5-200 microns and a short-wave band of .2-5 microns. These data are recorded on board by both a scanner and two non-scanner instruments. The scanner, whose observations are one set of data used in this study, have a resolution of approximately 36 by 48 kilometers.

The other set of data used for this study is obtained from the VISSR Atmospheric Sounder (VAS) on board GOES-6. Observations from the VAS are obtained in 12 spectral channels with a resolution of either 14 or 8 kilometers. The oversampled 14 km Multi-Spectral Image (MSI) data from VAS is used in this study to obtain temporal coincidence with the ERBS coverage. Theoretical studies (Smith and Woolf, 1982) indicate that a strong relationship exists between the multi-spectral radiance observations obtained in this mode and the outgoing long-wave radiation flux. Channel 7 (12.7μ) is particularly sensitive to low level moisture whereas channel 8 (11.2μ), the infrared window, possesses high sensitivity to surface temperature and cloudiness.

Knowledge of the relationship between the VAS and ERBS instruments will be very useful for climate studies. One application of this information is to the study of the diurnal cycle of cloudiness and radiation. With hourly observations from VAS, more complete information becomes available in the western hemisphere for studying the diurnal cycle and for estimating daily averages from the satellite ERBE system.

This paper develops a preliminary relationship between the outgoing long-wave radiation flux as detected by ERBS and the spectral radiances observed by the VAS MSI channels which are most strongly correlated to the earth-atmosphere outgoing long-wave radiation flux.

## 2. LONG-WAVE INTERCOMPARISON

### 2.1 Data Selection

The first revised, but preliminary ERBS tape released by NASA-Langley which possesses data for the same time that a VAS data set was available is for February 7, 1985. In order to compare and form relationships between the data from the two satellites the observations from each must be nearly simultaneous. Since the area of VAS coverage is fixed, comprising North and South America and the surrounding oceanic region, ERBS passes over this region provide the only opportunity for comparison. A nearly ideal ERBS orbit is available on this date, passing over the VAS subpoint at the equator near 108°W. This orbit covers a region with a diversity of cloud types beginning near 40°N in the eastern U.S. extending into the Gulf of Mexico to the Yucatan peninsula. This pass crosses the jet stream and includes a region where cirrus is widespread (see Figure 1).

Ordinarily, cloud motion is greatest in the jet stream. As a test of the comparison method this region of coverage was chosen since it is the most difficult weather type to be encountered. The technique applied involved computer selection of points for comparison. The goal was to select a region starting at 40°N on the ERBS tape and choose points that gave good coverage, minimized redundancy, and retained good resolution, recognizing that the resolution for all satellites is best near their subpoint track and is worse near the horizon. Since there is considerable ERBS scanner observation redundancy at the satellite subpoint the solution was to require a minimum distance of 30 kilometers between the points selected along a scan line. Each ERBE scan line contains 62 elements; to avoid the low resolution regions near the horizon, the first and last 11 elements along each line were excluded. Of the remaining 40 elements redundancy elimination near the middle of each scan line reduced the average number of data points selected from each scan line to 26. Observations were selected from 100 scan lines giving a total of 2583 picture points. An outline of the ERBS long-wave top of the atmosphere region is shown in Figure 2.

After the data point locations were chosen from the ERBS tape, the closest locations to the preliminary points were found in the VAS/MSI data. The oversampled VAS data have a spatial resolution approximately five times better than the ERBS so an average of 25 VAS observations

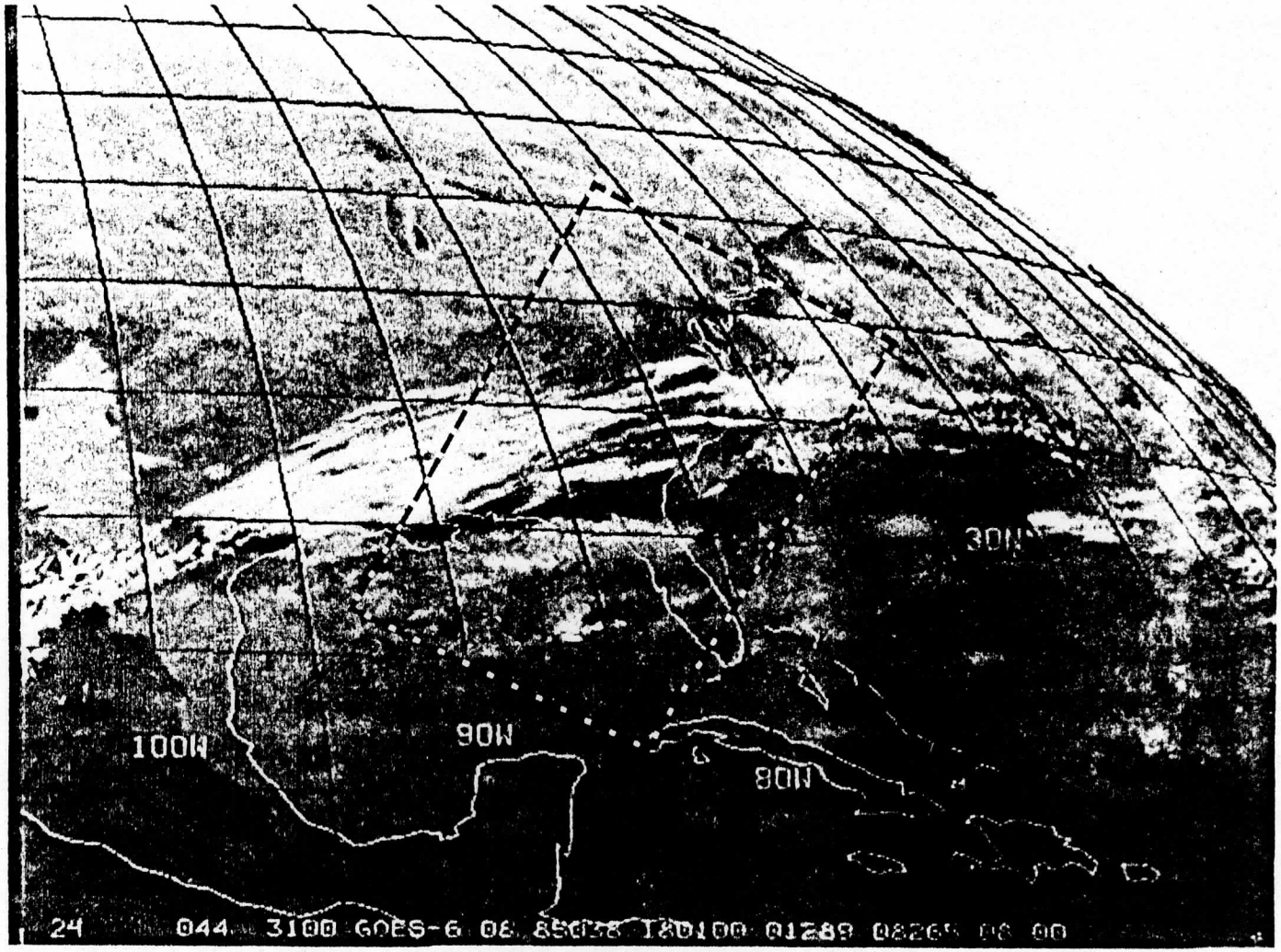


Fig. 1. VAS infrared picture for 1801 GMT February 7, 1985 showing region matched by ERBS orbit.


Fig. 2. ERBS top of the atmosphere flux for near 1800 GMT February 7, 1985 showing region matched with VAS picture.

overlapping the ERBS observation was computed. In order to insure comparisons of uniform scene fields of view, a limit on the range between the maximum and the minimum VAS brightness temperatures of 5°C in the channel 8 data was chosen. After applying this criteria, 697 samples remained.

## 2.2 Regression Relationships

The quality of fit of a simple linear relationship (not shown) between the VAS channel 8 brightness temperatures and ERBS top of the atmosphere long-wave values indicated that a higher order regression relationship was needed. Also, it is better to correlate quantities converted to the same physical units. As a result, equivalent blackbody fluxes were computed from the VAS brightness temperatures using the Stephan Boltzman law: $R_{v8} = \sigma T^4$ where $\sigma$ is the Stephan Boltzman constant, T is the VAS brightness temperature, and $R_{v8}$ is the equivalent VAS blackbody flux. The regression line obtained from this relation and the scatter of the data about this line are shown in Figure 3.

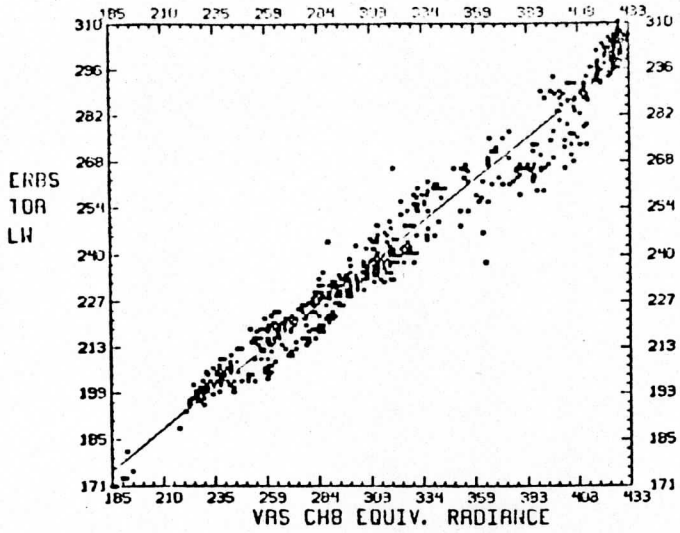


Fig. 3. Scatter diagram and regression line relating the VAS equivalent radiance to the ERBS top of the atmosphere long-wave values.

The statistics of this case are shown in Table 1 and the regression equation obtained was: $R_E = .507\ R_v - 80.7$ where $R_E$ is the predicted ERBS top of the atmosphere long wave value. Note the high correlation coefficient of .9841, in spite of the apparent wide scatter about the line. The large mean deviation between the VAS 11 μm channel blackbody flux and the ERBS top of the atmosphere flux is explained by the absorption by atmospheric constituents observed outside the 11 μm window in the broad band observed by ERBS.

| | |
|---|---|
| Num | = 697 |
| Avg VAS | = 306.5 |
| Avg ERBS | = 235.2 |
| Cor. Coeff. | = .9841 |
| Standard Error of Estimate | = 5.940 |
| Explained Variance | = .9684 |

Table 1. Statistical relationships between VAS channel 8 equivalent radiance and ERBS top of the atmosphere long wave flux for 1801 GMT February 7, 1985.

Several multiple correlations were produced relating the ERBS to the VAS data. These were run separately, correlating the ERBS top of the atmosphere long-wave values and also the ERBS long-wave filtered (raw) data to the VAS data. The source of VAS variables were channels 7 and 8, and the secant function of the VAS satellite zenith angle of observation.

As shown in Table 2, one of the best results obtained was for the multiple correlation of $R_E$, the ERBS top of the atmosphere long-wave with: $R_{v7}$, the equivalent blackbody flux radiance for VAS channel 7; $R_{v8}$, the equivalent blackbody flux for VAS channel 8; sec θ, secant of the satellite zenith angle of the VAS observation.

| | Step 1 | Step 2 | Step 3 |
|---|---|---|---|
| Variable | $\sigma T_{v7}^4$ | sec θ | $\sigma T_8^4$ |
| Cor. Coeff. | .9874 | .9881 | .9882 |
| Standard Error of Estimate | 5.295 | 5.142 | 5.128 |
| Explained Variance | .9749 | .9763 | .9765 |

Table 2. Step-wise multiple regression statisctics for predicting ERBS top of the atmosphere long-wave values from VAS data.

On the first step of the step-wise multiple regression the variable chosen was $R_{v7}$ since it is highly correlated with surface and cloud radiation, and also more sensitive to water vapor emission than is $R_{v8}$. On the second step, the secant of the satellite zenith angle was chosen, and on the third step channel 8 equivalent blackbody flux was included.

The data from the 1801 GMT sample was augmented by additional data from the next ERBS pass at 1930 GMT. The additional data was obtained using the same criteria discussed above. Two areas were chosen for diversity of scene, centered near 10°W 120°W and 40°N 100°W.

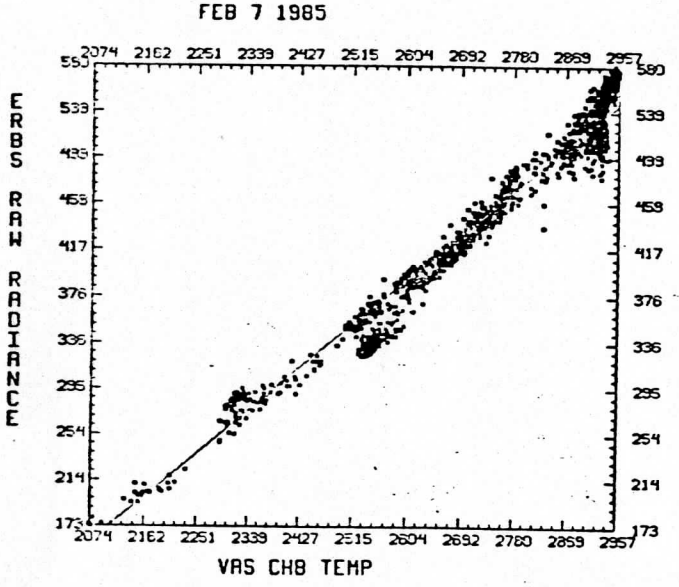


Fig. 4. Scatter diagram and regression line relating the VAS channel 8 temperature to the ERBS raw radiance. Both axis are multiplied by 10.

The scatter of the data is shown in Figure 4. The wide scatter at the warm end where temperatures are greater than 290°K appear to be due to the inability of the channel 8 window to detect the variation of low level moisture commonly found over the ocean surface. Table 3 shows the statistics for the multiple regression on this sample. The final relation found was:

$$R_E = 1.052\sigma T_{v7}^4 - .3995\sigma T_{v8}^4 - 1.195 \sec\theta + 44.36$$

| | Step 1 | Step 2 | Step 3 |
|---|---|---|---|
| Variable | $\sigma T_{v7}^4$ | $\sigma T_{v8}^4$ | sec θ |
| Cor. Coeff. | .9847 | .9858 | .9859 |
| Standard Error of Estimate | 6.735 | 6.478 | 6.468 |
| Explained Variance | .9696 | .9719 | .9720 |

Table 3. Expanded sample step-wise multiple regression statistics for predicting ERBS top of the atmosphere long wave values from VAS data.

## 3. FURTHER WORK

The relationship found here for uniform fields will be checked against an independent data set to validate its usefulness. Even if it appears to stand up to such a test, it must be remembered that the preliminary ERBS data it comes from has not itself been fully validated, especially the TOA modeling. Hence revisions may be necessary, though in all probability any changes would be expected to be small. Application of the relationship to determine the diurnal cycle and the specification of daily average fluxes from the ERBS for various regimes will be presented at the meeting.

## 4. ACKNOWLEDGEMENTS

Thanks to Harold Woolf for assistance with VAS algorithms. Funding for this research has been provided by the NASA, ERBE project through Grant NASA-16507.